A hybrid shell-beam element for straight thin-walled tubular structures

Y. Pascal-Abdellaoui, F. Daude, Claude Stolz, P. Lafon, P. Galon

A hybrid shell-beam element for straight thin-walled tubular structures

Y. Pascal-Abdellaoui[a,b], F. Daude[a,b], C. Stolz[b], P. Lafon[a,b], P. Galon[b,c]

[a] *EDF R&D, ERMES, F-91120 Palaiseau, France*
[b] *IMSIA, UMR EDF-CNRS-CEA-ENSTA 9219, F-91762 Palaiseau, France*
[c] *CEA Saclay, DEN/SEMT, Université Paris-Saclay, F-91191 Gif-sur-Yvette, France*

Abstract

A novel beam model is proposed in order to consider deformations of its cross-section in the context of straight thin-walled tubes. For this purpose, the straight beam kinematics is enriched by addition of orthogonal shell-type displacement field of the tube section. The considered displacement field is composed of three contributions: classical linear beam and linear shell terms in conjunction with the non-linear coupling between local deformation of the section and its global rotation. Both Euler-Bernoulli and Love-Kirchhoff hypotheses for beam and shell kinematics, respectively, are adopted as well as the thin-walled assumption. First-order shear deformation for the radial variable and Fourier expansion in terms of the circumferential variable are also considered for the mid-surface displacement field. Then, the stress tensor is obtained under plane stress conditions. The virtual power principle is finally used to obtain the equations of motion satisfied by the corresponding generalized forces. Afterwards, an explicit updated Lagrangian Finite-Element approach using a lumped mass matrix is proposed for solving the tube governing equations and the stability condition of the time integration is given. Test-cases are then chosen to assess the present tube finite-element. Both static and dynamic problems are considered. First, the proposed model is compared to analytical solutions. Finally, a tube subjected to a distributed patch loading is studied. The influence of the number of Fourier modes, of warping and coupling terms is examined. The proposed model makes it possible to retrieve classical shell solution of the cross-section deformation with significant computational savings.

Keywords: Beam kinematics, shell kinematics, straight thin-walled tubes, explicit time integration, Finite-Element method

1. Introduction

Piping systems are widely used in many industrial energy and transportation applications. Under operational or accident conditions, pipelines can be subjected to a wide variety of static or dynamic loads. The dynamic behavior of such structures has therefore received much attention in recent decades. Furthermore, the presence of fluid inside the pipes also has a significant influence on the pipe motion. The fluid-structure interaction (FSI) effects in piping systems are summarized in following comprehensive textbooks [1, 2] and reviews [3, 4]. Two main approaches have been developed in order to represent the mechanical behavior of pipelines based on shell or beam models. A very large literature exists for describing models issued from different theories. Shell models describe the pipe mid-surface motion in order to depict the cross-sectional evolution. However, the high computational cost associated with these models prohibits their use for realistic complex piping systems. In contrast, beam models describe the pipe center line motion considering rigid cross-sections rendering these models very computationally efficient without taking account of cross-sectional evolutions. What is more, some piping elements such as elbows are known since the pioneer work of von Kàrmàn [5] to present significant cross-section deformations under bending. As a consequence, formulations able to represent the pipe cross-section deformations at an affordable computational cost are of strong interest.

For this purpose, many researchers have previously proposed formulations based on finite elements for both curved and straight pipes [6, 7, 8, 9, 10, 11, 12, 13, 14, 15, 16, 17]. In addition, Weicker *et al.* [14] have reviewed much of the

Email addresses: frederic.daude@edf.fr (F. Daude), claude.stolz@cnrs.fr (C. Stolz)

aforementioned research. For example, in order to consider the pipe radial expansion into their formulation, Ohtsubo & Watanabe [6] use the thin Love-Kirchhoff shell kinematic constraints in conjunction with Fourier series expansions in terms of the tangential variable for longitudinal, tangential and radial displacements of the pipe mid-surface. Furthermore, Bathe & Almeida [7] have proposed a formulation based on the combination between beam and shell kinematics where cross-sectional deformations are expressed in Fourier series. In addition, warping deformations are neglected and the inextensibility in the circumferential direction is assumed by the authors. Additional improvements have been proposed in order to consider interaction effects between straight and curved pipes [18] and pressure stiffening effects [19]. Then, Militello & Huespe [9] consider warping displacements into the formulation initially proposed by Bathe & Almeida in [7]. What is more, Abo-Elkhier [10] consider a more complete displacement-strain relations into this formulation. Finally, as reviewed in [14], there is a great difference among the previously mentioned works. For example, incomplete Fourier expansions are considered as well as some displacements as warping are neglected. For instance, only the second mode of ovalization is considered in [8, 11]. For more generality, complete Fourier series for all three displacements of the mid-surface are adopted in [14, 15] within the framework of the approach proposed by Ohtsubo & Watanabe [6]. The obtained formulation considers warping deformations, variations of tangential and longitudinal displacements in the longitudinal and transverse directions as well as the pipe radial expansion. In addition, Attia *et al.* [16] have compared three different interpolating schemes for the displacement fields in the circumferential direction showing the good behavior of the Fourier series expansion in the context of straight pipes. More recent researches have been published concerning enriched beam elements. For example, a non-linear beam model has been proposed in order to take into account the Poisson effect [20]. Moreover, a high-order beam model has been recently derived to consider deforming cross-sections including both Poisson effect and warping deformations [21]. In addition, enhanced beam kinematics is also considered in [22] to allow distortion of the cross section. In addition, a higher-order beam model able to accurately represent the buckling behaviour of three-dimensional thin-walled structures has been proposed in [23]. Furthermore, a geometrically exact cross-section deformable curved thin-walled beam finite element is proposed in [24]. In the aforementioned research, non-linear or high-order beam models are used for the derivation of the elements. A review of beam models can be found in the textbook [25].

A new non-linear tube model is here proposed for straight thin-walled pipes. The corresponding displacement field is taken as a combination of three contributions:

- an Euler-Bernoulli beam model (for the tube axis motion),
- a Love-Kirchhoff shell kinematics (for the mid-surface evolution) in order to consider both warping and evolution of the cross-section,
- a non-linear coupling between local deformation of the cross-section and the rotation of the tube axis.

Thanks to the consideration of this non-linear coupling, the pipe inertia evolve with cross-section deformation, possible cross-section ovalization is then ensured. Furthermore, the thin-walled cylindrical Flügge shell theory is adopted. In addition, complete Fourier series are used for the shell kinematics respectively to the tangential (or circumferential) variable. As in [12], the coefficients in Fourier expansion corresponding to rigid-body motion are excluded to avoid redundancy with the beam displacements and rotations.

In conjunction with this new model, an explicit solver based on an updated Lagrangian Finite-Element approach is also developed here. Focus is given to the explicit time integration for considering fast-transient events occurring in accidental conditions. Due to the use of explicit schemes, additional questions arise especially concerning the mass matrix as well as the stability condition. As for all elements involving both translational and rotational degrees of freedom (DOFs), a special attention has to be given to the lumped mass matrix. Finally, stability conditions are here simply estimated using natural frequencies of both beams and shells.

The paper is organized as follows. Section 2 is devoted to the derivation of the proposed tube model. The tube kinematics decomposed into both beam and shell terms is presented as well as the non-linear coupling between the tube cross-section deformations and the tube axis rotations. The assumptions adopted for the derivation of the present tube model are also detailed. Afterwards, explicit finite-element resolution of the proposed model is presented in Section 3. In particular, the lumped mass matrix is described and stability conditions are given. The tube model is then assessed on several problems involving a variety of loads in Section 4. Both static and dynamic problems are examined. A series of test-cases where analytical solutions are available is first considered. Finally, the proposed tube

model is assessed on a distributed patch load via the comparison with shell elements. In particular, influence of the number of Fourier modes is analyzed as well as influence of warping and of non-linear coupling.

2. Theoretical model: kinematics, strain-displacement relations and equations of motion

This section is devoted to the derivation of the model proposed here for straight thin-walled tubular geometries. For this purpose, kinematics is decomposed into beam and shell contributions. Conditions of Euler-Bernoulli for the beam contribution and Love-Kirchhoff for the shell description are assumed. In addition, a non-linear coupling between cross-section deformation and rotation of the tube axis is considered. Finally, the tube equations of motion obtained using the virtual power principle are given.

2.1. Enriched beam kinematics of a straight tube

Let us consider a straight tube of length L, mean radius a and thickness e along the axis $\mathbf{E}_x$ as depicted in Fig. (1). The axial, circumferential and radial (with respect to the mean radius) coordinates are denoted by x, θ and z,

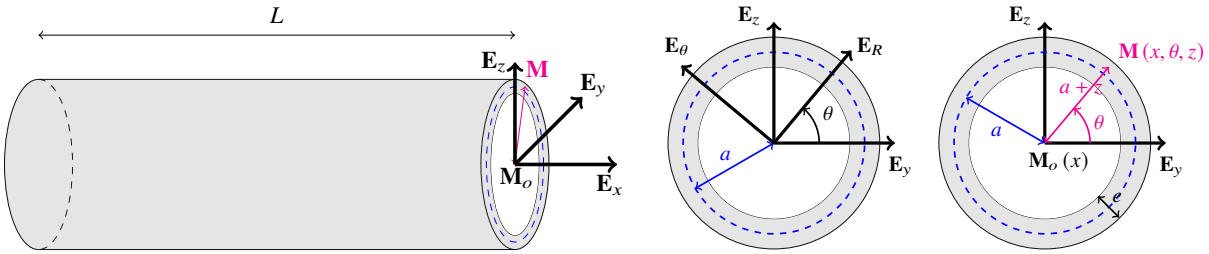

Figure 1: Sketch of a straight pipe: flat view (left), cross-sectional view - cylindrical coordinate system (center), pipe mid-surface, i.e. $z = 0$, and thickness (right).

respectively, while t denotes the time.

The kinematics is here decomposed into beam-type and shell-type contributions. The beam motion is given by displacements of the tube axis, i.e. $U_o(t,x)$, $W_o(t,x)$ and $V_o(t,x)$ expressed in the basis $(\mathbf{E}_x, \mathbf{E}_y, \mathbf{E}_z)$ and by rotations of section, i.e. $\mathbf{R}(t,x)$. Thereafter, the shell-type kinematics is associated with the relative displacements with respect to the rotated section, i.e. $u(t,x,\theta,z)$, $w(t,x,\theta,z)$ and $v(t,x,\theta,z)$ expressed in the basis $(\mathbf{E}_x, \mathbf{E}_R, \mathbf{E}_\theta)$, where $-e/2 \leq z \leq e/2$ (see Figs. (2) and (3)). These displacements represent respectively the warping (associated

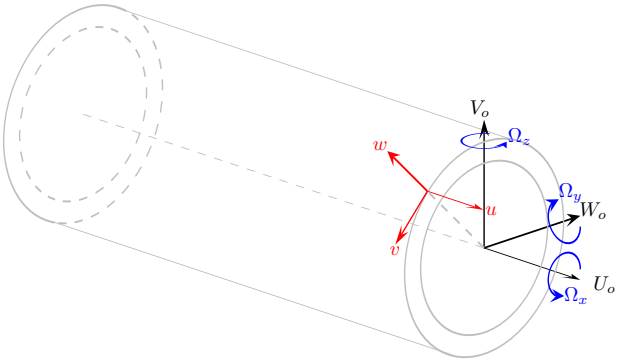

Figure 2: Beam and shell displacements: $U_o, V_o, W_o, \Omega_x, \Omega_y$ and Ω_z for the beam kinematics and u, v and w for the shell kinematics.

with u) and the ovalization (associated with v and w) of the deformed section, (see Figs. (2) and (3)).

The coordinates of the point denoted by $\mathbf{M}(x, \theta, z)$ in the initial state and the coordinates of the point $\mathbf{m}(t, x, \theta, z)$ in the deformed state are respectively given by:

$$\begin{aligned} \mathbf{M} &= \mathbf{M}_o + (a+z)\,\mathbf{E}_R = x\,\mathbf{E}_x + (a+z)\,\mathbf{E}_R \\ \mathbf{m} &= \mathbf{M} + \mathbf{U} = (x+U_o)\,\mathbf{E}_x + V_o\,\mathbf{E}_z + W_o\,\mathbf{E}_y + \mathbf{R}(t,x).\Big((a+z+w)\,\mathbf{E}_R + u\,\mathbf{E}_x + v\,\mathbf{E}_\theta\Big) \end{aligned} \tag{1}$$

The rotation of the section is considered to be small, therefore:

$$\mathbf{R}(t,x) = \mathbf{I} + \boldsymbol{\Omega}(t,x), \quad \boldsymbol{\Omega}.\mathbf{V} = \big(\Omega_x(t,x)\,\mathbf{E}_x + \Omega_y(t,x)\,\mathbf{E}_y + \Omega_z(t,x)\,\mathbf{E}_z\big) \wedge \mathbf{V} \tag{2}$$

where $\mathbf{V}$ is any 3-D vector and $\mathbf{I}$ the identity matrix.

Even if a full 3-D motion has been developed as described in [26], only an in-plane motion in $(\mathbf{E}_x, \mathbf{E}_z)$ is considered in the following in order to simplify the presentation of the new model, i.e. $W_o = 0$ and $\Omega_x = \Omega_z = 0$ (see Fig. (3)). Assuming small perturbations, linear strain in terms of displacement is considered. However, in order to take into account the ovalization of the section in a straight tube, a non-linear coupling between the beam-type rotation and the shell-type displacements is also introduced. Only the coupling between the cross-section ovalization driven by w and v and the rotation of the tube axis, i.e. Ω_y, is taking into account, the coupling involving the warping cross-section being here neglected. As it is explained in the following, the consideration of this coupling ensures that the inertia of the section can evolve. In addition, the present motion considers the dynamic behavior as the proposed tube model is a first step for the simulation of fast-transient events involving fluid-structure interaction in piping systems with deformable cross-sections.

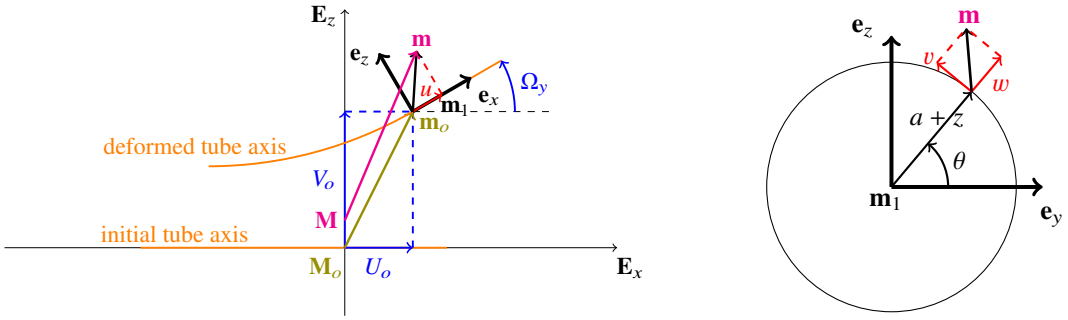

Figure 3: In-plane beam motion (left) and shell displacement in the tube cross-section (right).

The current position, $\mathbf{m}(t, x, \theta, z)$, is written in the cylindrical basis $(\mathbf{E}_x, \mathbf{E}_R, \mathbf{E}_\theta)$ as:

$$\mathbf{m} = \big(x + U_o + u + [(a+z+w)\sin\theta + v\cos\theta]\,\Omega_y\big)\,\mathbf{E}_x + (a+z+V_o\sin\theta+w)\,\mathbf{E}_R + (V_o\cos\theta + v)\,\mathbf{E}_\theta \tag{3}$$

The non-linear coupling is described in the axial component by the term $h\Omega_y$ with $h = w\sin\theta + v\cos\theta$. The derivatives of the position vector $\mathbf{m}$ with respect to the coordinates x, θ and z are detailed in Appendix A as well as the strain-

displacement relations which are given in Eq. (A.1) and summarized in the following:

$$\begin{cases} \varepsilon_{xx} = \dfrac{\partial U_o}{\partial x} + (a+z)\sin\theta\dfrac{\partial \Omega_y}{\partial x} + \dfrac{\partial u}{\partial x} + \left(\Omega_y + \dfrac{\partial V_o}{\partial x}\right)\dfrac{\partial h}{\partial x} + h\dfrac{\partial \Omega_y}{\partial x} \\ \varepsilon_{\theta\theta} = \dfrac{1}{a+z}\left(\dfrac{\partial v}{\partial \theta} + w\right) \\ \varepsilon_{zz} = \dfrac{\partial w}{\partial z} \\ 2\,\varepsilon_{x\theta} = \left(\Omega_y + \dfrac{\partial V_o}{\partial x}\right)\cos\theta + \dfrac{1}{a+z}\dfrac{\partial u}{\partial \theta} + \dfrac{\partial v}{\partial x} + \dfrac{1}{a+z}\left(\Omega_y + \dfrac{\partial V_o}{\partial x}\right)\dfrac{\partial h}{\partial \theta} \\ 2\,\varepsilon_{xz} = \left(\Omega_y + \dfrac{\partial V_o}{\partial x}\right)\sin\theta + \dfrac{\partial u}{\partial z} + \dfrac{\partial w}{\partial x} + \left(\Omega_y + \dfrac{\partial V_o}{\partial x}\right)\dfrac{\partial h}{\partial z} \\ 2\,\varepsilon_{z\theta} = \dfrac{1}{a+z}\left(\dfrac{\partial w}{\partial \theta} - v\right) + \dfrac{\partial v}{\partial z} \end{cases} \tag{4}$$

The strain tensor given in Eq. (4) is decomposed into three contributions: linear beam-type kinematic terms $\boldsymbol{\varepsilon}^b$, linear shell-type kinematic terms $\boldsymbol{\varepsilon}^s$ and non-linear *coupling* terms $\boldsymbol{\varepsilon}^{nl}$:

$$\begin{array}{lll} \varepsilon^b_{xx} = \dfrac{\partial U_o}{\partial x} + (a+z)\sin\theta\dfrac{\partial \Omega_y}{\partial x}, & \varepsilon^s_{xx} = \dfrac{\partial u}{\partial x}, & \varepsilon^{nl}_{xx} = \left(\Omega_y + \dfrac{\partial V_o}{\partial x}\right)\dfrac{\partial h}{\partial x} + h\dfrac{\partial \Omega_y}{\partial x}, \\ \varepsilon^b_{\theta\theta} = 0, & \varepsilon^s_{\theta\theta} = \dfrac{1}{a+z}\left(\dfrac{\partial v}{\partial \theta} + w\right), & \varepsilon^{nl}_{\theta\theta} = 0, \\ \varepsilon^b_{zz} = 0, & \varepsilon^s_{zz} = \dfrac{\partial w}{\partial z}, & \varepsilon^{nl}_{zz} = 0, \\ 2\,\varepsilon^b_{x\theta} = \left(\Omega_y + \dfrac{\partial V_o}{\partial x}\right)\cos\theta, & 2\,\varepsilon^s_{x\theta} = \dfrac{1}{a+z}\dfrac{\partial u}{\partial \theta} + \dfrac{\partial v}{\partial x}, & 2\,\varepsilon^{nl}_{x\theta} = \dfrac{1}{a+z}\left(\Omega_y + \dfrac{\partial V_o}{\partial x}\right)\dfrac{\partial h}{\partial \theta}, \\ 2\,\varepsilon^b_{xz} = \left(\Omega_y + \dfrac{\partial V_o}{\partial x}\right)\sin\theta, & 2\,\varepsilon^b_{xz} = \dfrac{\partial u}{\partial z} + \dfrac{\partial w}{\partial x}, & 2\,\varepsilon^{nl}_{xz} = \left(\Omega_y + \dfrac{\partial V_o}{\partial x}\right)\dfrac{\partial h}{\partial z}, \\ 2\,\varepsilon^b_{z\theta} = 0, & 2\,\varepsilon^s_{z\theta} = \dfrac{1}{a+z}\left(\dfrac{\partial w}{\partial \theta} - v\right) + \dfrac{\partial v}{\partial z}, & 2\,\varepsilon^{nl}_{z\theta} = 0. \end{array} \tag{5}$$

Considering the beam strain, the absence of shear deformation corresponding to the Euler-Bernoulli hypothesis imposes that:

$$\varepsilon^b_{xz} = 0 \quad \text{or equivalently} \quad \Omega_y + \frac{\partial V_o}{\partial x} = 0 \tag{6}$$

Under this hypothesis, the beam kinematics enforces planar sections normal to the neutral axis to remain planar after deformation. As a consequence, the deformation terms associated to the beam are only present in the ε^b_{xx} component. Finally, this corresponds to a beam whose straight section is an undeformed circular ring. Note that one of the main consequences of the previous hypothesis is that the non-linear coupling term is only present in the ε_{xx} component, i.e. $\varepsilon^{nl}_{xx} = h\partial_x\Omega_y$ while $\varepsilon^{nl}_{\theta\theta} = \varepsilon^{nl}_{zz} = \varepsilon^{nl}_{x\theta} = \varepsilon^{nl}_{xz} = \varepsilon^{nl}_{z\theta} = 0$.

Concerning the shell-type kinematics, the mid-surface of the tube corresponding to $z = 0$ (see Fig. (4)) is taken to be the reference surface and the local rotations of this surface are here considered and assumed to be small. Taking the classical Love-Kirchhoff hypothesis corresponding to the absence of shear deformation for the shell kinematics, i.e. the shell-type terms in the ε^s_{xz} and $\varepsilon^s_{z\theta}$ components being null, leads to the two following additional relations:

$$\frac{\partial u}{\partial z} + \frac{\partial w}{\partial x} = 0 \quad \text{and} \quad \frac{1}{a+z}\left(\frac{\partial w}{\partial \theta} - v\right) + \frac{\partial v}{\partial z} = 0 \tag{7}$$

The shell kinematics follows here the first-order shear deformation shell theory [27, 28] leading to the following displacement field:

$$w = w_o, \quad v = v_o + z v_1, \quad u = u_o - z u_1 \tag{8}$$

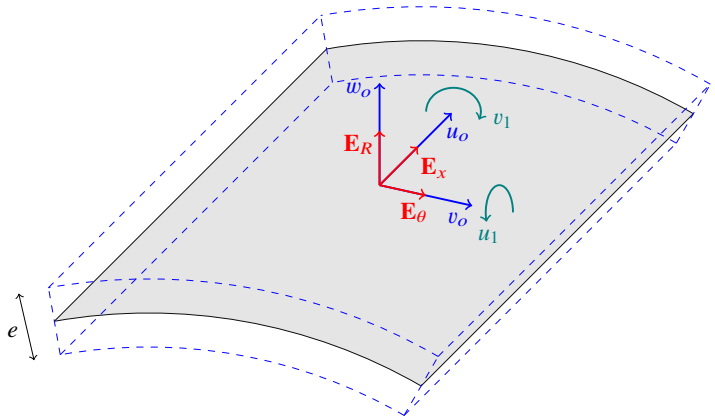

Figure 4: Shell geometry: tube mid-surface at $z = 0$ in gray, its associated cylindrical coordinates system $(\mathbf{E}_x, \mathbf{E}_R, \mathbf{E}_\theta)$ and the shell DOFs: u_o, v_o, w_o, u_1 and v_1.

with u_1 and v_1 the rotation angles of the mid-surface of transverse normal $\mathbf{E}_R$ in the $(\mathbf{E}_x, \mathbf{E}_R)$ and $(\mathbf{E}_R, \mathbf{E}_\theta)$ planes, respectively, (see Fig. (4)). As a consequence, Eq. (7) rewrites as:

$$u_1 = \frac{\partial w_o}{\partial x} \quad \text{and} \quad v_1 = -\frac{1}{a}\left(\frac{\partial w_o}{\partial \theta} - v_o\right) \tag{9}$$

Under this hypothesis, the shell kinematics enforces straight fibres initially perpendicular to the middle surface to remain straight and perpendicular to the deformed mid-surface.

In addition, the global strain tensor is decomposed into first-order terms related to the radial variable z and the thin-shell hypothesis is also considered. As a consequence, terms in $\dfrac{1}{a+z}$ are approximated as follows:

$$\frac{1}{a+z} = \frac{1}{a} - \frac{z}{a^2} + o\left(\frac{z}{a^2}\right) \tag{10}$$

neglecting the second-order and higher order terms. Consequently, the strain tensor can be decomposed as the sum of a membrane term denoted by $\boldsymbol{\varepsilon}^m$ and a linear term in z corresponding to curvatures denoted by $\mathbf{k}$ as $\boldsymbol{\varepsilon} = \boldsymbol{\varepsilon}^m + z\,\mathbf{k}$ which can be expressed in terms of both axis displacements, i.e. U_o and V_o, and mid-surface displacements, i.e. u_o, v_o and w_o:

$$\begin{aligned}
\varepsilon_{xx} &= \frac{\partial U_o}{\partial x} - a\sin\theta\,\frac{\partial^2 V_o}{\partial x^2} + \frac{\partial u_o}{\partial x} - \frac{\partial^2 V_o}{\partial x^2}\left(w_o\sin\theta + v_o\cos\theta\right) + z\,k_{xx} \\
\varepsilon_{\theta\theta} &= \frac{1}{a}\left(\frac{\partial v_o}{\partial \theta} + w_o\right) + z\,k_{\theta\theta} \\
2\,\varepsilon_{x\theta} &= \frac{1}{a}\frac{\partial u_o}{\partial \theta} + \frac{\partial v_o}{\partial x} + 2\,z\,k_{x\theta}
\end{aligned} \tag{11}$$

and the following curvature terms:

$$\begin{aligned}
k_{xx} &= -\sin\theta\,\frac{\partial^2 V_o}{\partial x^2} - \frac{\partial^2 w_o}{\partial x^2} + \frac{\cos\theta}{a}\frac{\partial^2 V_o}{\partial x^2}\left(\frac{\partial w_o}{\partial \theta} - v_o\right) \\
k_{\theta\theta} &= -\frac{1}{a^2}\left(\frac{\partial^2 w_o}{\partial \theta^2} + w_o\right) \\
2\,k_{x\theta} &= -\frac{1}{a}\left(2\,\frac{\partial^2 w_o}{\partial x \partial \theta} + \frac{1}{a}\frac{\partial u_o}{\partial \theta} - \frac{\partial v_o}{\partial x}\right)
\end{aligned} \tag{12}$$

Notice that the shell-type membrane and curvature terms correspond exactly to those obtained with the Flügge shell theory [29]. A brief review of thin cylindrical shell theories can be found in [14] where it is shown that the different contributions on thin-shell theory all agree concerning the expressions of the membrane strain. However, different expressions for curvature have been obtained relying upon the assumptions used in the derivation. For example, the shell-type curvature terms adopted in Ohtsubo and Watanabe [6], Millard and Roche [8], Berton [11] or in Weicker *et al.* [14] are different from the present ones and correspond to those developed by Timoshenko [30]. However, it has to be noticed that with the additional assumption of the pipe radial inextensibility, the mentioned thin cylindrical shell theories lead to the same strain-displacement relations. In the present work, the pipe is not assumed to be inextensible in order to capture its radial expansion/contraction. Finally, in all these previous works, the coupling terms between the section deformation and the axis rotation have not been taken into account. The coupling contributes only in the uni-axial components ε^m_{xx} and k_{xx}.

2.2. Fourier series expansion

The shell displacement field is now expanded in Fourier series in terms of the tangential variable θ. In contrast to previous works [31, 8, 13, 32, 7, 9, 10] where incomplete displacement Fourier series are considered, the longitudinal, tangential and radial mid-surface displacements, i.e. u_o, v_o and w_o, are here all expanded in Fourier series:

$$\begin{cases} u_o(t,x,\theta) &= u_o^c(t,x) + u_1^c(t,x)\cos\theta + u_1^s(t,x)\sin\theta \; + \sum_{i=2}^{N_f} \left(u_i^c(t,x)\cos(i\theta) + u_i^s(t,x)\sin(i\theta)\right) \\ v_o(t,x,\theta) &= v_o^c(t,x) \; + v_1^c(t,x)\cos\theta + v_1^s(t,x)\sin\theta \; + \sum_{i=2}^{N_f} \left(v_i^c(t,x)\cos(i\theta) + v_i^s(t,x)\sin(i\theta)\right) \\ w_o(t,x,\theta) &= w_o^c(t,x) + w_1^c(t,x)\cos\theta + w_1^s(t,x)\sin\theta + \sum_{i=2}^{N_f} \left(w_i^c(t,x)\cos(i\theta) + w_i^s(t,x)\sin(i\theta)\right) \end{cases} \tag{13}$$

N_f represents the number of Fourier modes considered in the expansion. $u_i^c(t,x)$, $u_i^s(t,x)$, $v_i^c(t,x)$, $v_i^s(t,x)$, $w_i^c(t,x)$ and $w_i^s(t,x)$ are the coefficients of the Fourier series becoming the new unknowns and depending only on the longitudinal variable x (and on the time t). The index c represents the coefficients in cosine while the index s the coefficients in sine in the Fourier expansion.

The coefficients in the expansion producing a rigid-body motion are set equal to zero in order to avoid redundancy with the beam-type degrees of freedom. As a consequence, u_o^c corresponding to a rigid-body longitudinal displacement is taken to be zero. Similarly, u_1^c, u_1^s and v_o^c are also null as these terms correspond to a rigid-body rotation about the $\mathbf{E}_z$, the $\mathbf{E}_y$ and the $\mathbf{E}_x$ axis, respectively. In addition, the coefficient multiplying $\cos\theta$ in the expansion of v_o has been set to the negative of the coefficient multiplying $\sin\theta$ in the expansion of w_o, i.e. $v_1^c(t,x) = -w_1^s(t,x)$. This produces a vanishing rigid-body displacement of the cross-section in the $\mathbf{E}_z$ direction [12] via the integration over the tangential variable θ. In the same way, the coefficient multiplying $\sin\theta$ in the expansion of v_o has been set to the coefficient multiplying $\cos\theta$ in the expansion of w_o, i.e. $v_1^s(t,x) = w_1^c(t,x)$ in order to produce a vanishing rigid-body displacement of the cross-section in the $\mathbf{E}_y$ direction.

In addition, for Fourier modes of higher order, i.e. greater than or equal to two, an inextensibility assumption in the circumferential direction of the section is also taken in consideration meaning that the section perimeter remains constant [33, 34]. In other words, the circumferential membrane deformation is null, i.e. $(\varepsilon^m)_{\theta\theta} = 0$, for $i \geq 2$. As $(\varepsilon^m)_{\theta\theta} \equiv \frac{1}{a}(\partial_\theta v_o + w_o)$, this allows to obtain a relation between v_i^c, w_i^s, w_i^c and v_i^s for $i \geq 2$:

$$\frac{1}{a}\sum_{i=2}^{N_f}\left(\frac{\partial}{\partial\theta}\left(v_i^c\cos(i\theta) + v_i^s\sin(i\theta)\right) + w_i^c\cos(i\theta) + w_i^s\sin(i\theta)\right) = 0 \tag{14}$$

Thus, the shell-type displacements of the tube mid-surface can be expressed as:

$$\left\{\begin{array}{lcll} u_o & = & & \displaystyle\sum_{i=2}^{N_f}\left(u_i^c\cos(i\theta)+u_i^s\sin(i\theta)\right) \\ v_o & = & -w_1^s\cos\theta+w_1^c\sin\theta+ & \displaystyle\sum_{i=2}^{N_f}\left(\frac{1}{i}w_i^s\cos(i\theta)-\frac{1}{i}w_i^c\sin(i\theta)\right) \\ w_o & = & w_o^c \quad +w_1^c\cos\theta+w_1^s\sin\theta+ & \displaystyle\sum_{i=2}^{N_f}\left(w_i^c\cos(i\theta)+w_i^s\sin(i\theta)\right) \end{array}\right. \tag{15}$$

w_o^c represents the radial extensibility of the cross-section. w_1^c and w_1^s are associated with vanishing lateral rigid-body displacements. w_i^c and w_i^s for $i \geq 2$ represent cross-section distortions. In addition, u_i^c and u_i^s for $i \geq 2$ represent the warping cross-section deformations.

Finally, the tube displacement field is given by:

$$\mathbf{U} = \left(U_o + u + \left[(a+z+w)\sin\theta + v\cos\theta\right]\Omega_y\right)\,\mathbf{E}_x + (V_o\sin\theta + w)\,\mathbf{E}_R + (V_o\cos\theta + v)\,\mathbf{E}_\theta \tag{16}$$

respecting for the beam-type displacement terms the Euler-Bernoulli hypothesis

$$\Omega_y = -\frac{\partial V_o}{\partial x}$$

and with the shell-type displacement field:

$$w = w_o, \quad v = v_o + zv_1, \quad u = u_o - zu_1 \tag{17}$$

where u_o, v_o and w_o are expressed in Eq. (15) and with

$$u_1 = \frac{\partial w_o}{\partial x} \quad \text{and} \quad v_1 = -\frac{1}{a}\left(2w_1^s\cos\theta - 2w_1^c\sin\theta + \sum_{i=2}^{N_f}\frac{i^2-1}{i}\left(w_i^s\cos(i\theta) - w_i^c\sin(i\theta)\right)\right) \tag{18}$$

respecting the Love-Kirchhoff hypothesis.

2.3. Virtual power principle

The equations of motion can be obtained through the application of the virtual power principle which expresses the equilibrium between the forces of inertia, external and internal forces:

$$\mathcal{P}_a = \mathcal{P}_e + \mathcal{P}_i \tag{19}$$

with $\mathcal{P}_a$, $\mathcal{P}_e$ and $\mathcal{P}_i$ the power of inertia, external and internal forces, respectively. The power of inertia forces is defined in the current (deformed) configuration as:

$$\mathcal{P}_a = \int_\Omega \rho\frac{\partial^2\mathbf{U}}{\partial t^2}\cdot\delta\,\mathbf{U}\,\mathrm{d}V \tag{20}$$

in which the integration is performed over the current volume Ω occupied by the solid body and where ρ is the solid density, $\dfrac{\partial^2\mathbf{U}}{\partial t^2}$ the acceleration vector, $\delta\,\mathbf{U}$ the virtual displacement field.

The power of external forces (without considering volume forces) is defined as:

$$\mathcal{P}_e = \int_{\partial\Omega}\mathbf{T}.\delta\,\mathbf{U}\,\mathrm{d}S \tag{21}$$

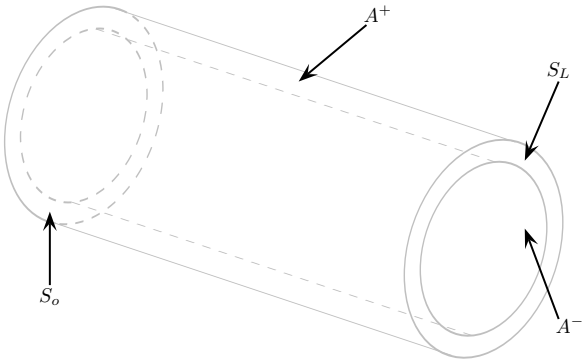

Figure 5: Tube surfaces decomposed by the two cross-sections S_o and S_L and by A^- the inner and A^+ the outer lateral sections.

$\mathbf{T}$ is the vector of applied forces on the boundaries. The edge of the tube is decomposed into the two end surfaces denoted by S_o and S_L where the elementary surface $\mathrm{d}S$ is set to be equal to $a\ \mathrm{d}\theta\mathrm{d}z$ instead of $(a+z)\ \mathrm{d}\theta\mathrm{d}z$ due to the thin-walled assumption, and the inner and outer skins of the tube denoted by A^- and A^+ where $A^\pm = 2\pi L(a \pm e/2)$ as depicted in Fig. (5).

Finally, the power of internal forces is given by:

$$\mathcal{P}_i = -\int_\Omega \boldsymbol{\sigma} : \delta\,\boldsymbol{\varepsilon}\ \mathrm{d}V \tag{22}$$

where $\boldsymbol{\sigma}$ is the Cauchy stress tensor and $\delta\,\boldsymbol{\varepsilon}$ the virtual stress tensor. Using the circular geometry of the considered pipe leads to the following expression for the power of internal forces:

$$\mathcal{P}_i = -\int_0^L \left(\int_0^{2\pi} \int_{-e/2}^{e/2} \boldsymbol{\sigma} : \delta\,\boldsymbol{\varepsilon}\ a\ \mathrm{d}\theta\mathrm{d}z \right) \mathrm{d}x \tag{23}$$

Due to the thin-shell assumption, i.e. $z << a$, the integration is performed through the elementary volume $a\ \mathrm{d}\theta\mathrm{d}z\mathrm{d}x$ instead of $(a+z)\ \mathrm{d}\theta\mathrm{d}z\mathrm{d}x$.

The strain-stress relationship is here obtained using a local linear elastic behavior:

$$\boldsymbol{\sigma} = \frac{E}{1-\nu^2}\left((1-\nu)\ \boldsymbol{\varepsilon} + \nu\ \mathrm{trac}(\boldsymbol{\varepsilon})\ \mathbf{I} \right) \tag{24}$$

Using plane stress conditions in the $(\mathbf{E}_\theta, \mathbf{E}_x)$ plane, i.e. $\sigma_{zz} = \sigma_{xz} = \sigma_{\theta z} = 0$, this leads to:

$$\begin{pmatrix} \sigma_{xx} \\ \sigma_{\theta\theta} \\ \sigma_{x\theta} \end{pmatrix} = \frac{E}{1-\nu^2} \begin{pmatrix} 1 & \nu & 0 \\ \nu & 1 & 0 \\ 0 & 0 & 1-\nu \end{pmatrix} \begin{pmatrix} \varepsilon_{xx} \\ \varepsilon_{\theta\theta} \\ \varepsilon_{x\theta} \end{pmatrix} \tag{25}$$

with ν the Poisson's ratio and E the Young's modulus of the pipe wall material.

The power of inertia forces as well as the power of internal forces are expressed in Appendix B (see Eqs. (B.5) and (B.8) respectively) when considering all the Fourier modes and the non-linear coupling terms. In addition, the governing equation of the tube are expressed in Eq. (B.14) and the corresponding generalized forces in Eqs. (B.9,B.10,B.11,B.12,B.13).

In the following, details are given when considering only the mode 0 in the Fourier series and then only the Fourier mode 2. As previously mentioned, Fourier mode 0 corresponds to the radial expansion/contraction of the tube cross-section whereas Fourier mode 2 corresponds to its ovalization. Comments are also given when higher Fourier modes are considered.

2.4. Governing equations and generalized forces for Fourier mode 0 for linear-type motion

When only the first Fourier mode ($N_f = 0$) is considered, the shell kinematics is only carried by w_o (i.e. $u_o = v_o = 0$) and u_1 (i.e. $v_1 = 0$) (cf. Eqs. (15) and (18)). In addition, the non-linear coupling term is not taken into account at this stage. As a consequence, the shell-type displacement field is given by:

$$w_o(t,x,\theta) = w_o^c(t,x), \quad u_1 = \frac{\partial w_o^c}{\partial x} \tag{26}$$

leading to the tube displacement field:

$$\mathbf{U} = \left(U_o - z\frac{\partial w_o^c}{\partial x} - (a+z)\sin\theta\,\frac{\partial V_o}{\partial x}\right)\mathbf{E}_x + \left(V_o\sin\theta + w_o^c\right)\mathbf{E}_R + \left(V_o\cos\theta\right)\mathbf{E}_\theta \tag{27}$$

As a consequence, the non-zero components of the strain tensor are given by:

$$\varepsilon_{xx} = \frac{\partial U_o}{\partial x} - a\sin\theta\frac{\partial^2 V_o}{\partial x^2} + z\left(-\sin\theta\frac{\partial^2 V_o}{\partial x^2} - \frac{\partial^2 w_o^c}{\partial x^2}\right) \quad \text{and} \quad \varepsilon_{\theta\theta} = \left(\frac{1}{a} - \frac{z}{a^2}\right)w_o^c \tag{28}$$

The power of internal forces can thus be expressed as:

$$\mathcal{P}_i = -\int_\Omega \boldsymbol{\sigma} : \delta\boldsymbol{\varepsilon}\,\mathrm{d}V = -\int_0^L \left(N\frac{\partial\delta U_o}{\partial x} - M_y\frac{\partial^2\delta V_o}{\partial x^2} - (m_w)_o^c\,\frac{\partial^2\delta w_o^c}{\partial x^2} + (t_w)_o^c\,\delta w_o^c\right)\mathrm{d}x \tag{29}$$

where the generalized forces are defined as:

$$\begin{aligned} N &= \int_S \sigma_{xx}\,\mathrm{d}S \quad ; \quad M_y = \int_S \sigma_{xx}\,(a+z)\sin\theta\,\mathrm{d}S \\ (t_w)_o^c &= \int_S \sigma_{\theta\theta}\left(\frac{1}{a} - \frac{z}{a^2}\right)\mathrm{d}S \quad ; \quad (m_w)_o^c = \int_S \sigma_{xx}\,z\,\mathrm{d}S \end{aligned} \tag{30}$$

with $\mathrm{d}S = a\mathrm{d}\theta\mathrm{d}z$. The term z/a^2 in $(t_w)_o^c$ is neglected in the following due to the thin-walled assumption.
In addition, the power of inertia forces can be expressed as:

$$\begin{aligned} \mathcal{P}_a &= \int_\Omega \rho\frac{\partial^2\mathbf{U}}{\partial t^2}\cdot\delta\mathbf{U}\,\mathrm{d}V \\ &= \int_0^L \rho\left(S\frac{\partial^2 U_o}{\partial t^2}\delta U_o + S\left(\frac{\partial^2 V_o}{\partial t^2} - \frac{I_y^b}{S}\frac{\partial^4 V_o}{\partial t^2\partial x^2}\right)\delta V_o + S\left(\frac{\partial^2 w_o^c}{\partial t^2} - \frac{e^2}{12}\frac{\partial^4 w_o^c}{\partial t^2\partial x^2}\right)\delta w_o^c\right)\mathrm{d}x \end{aligned} \tag{31}$$

with the pipe cross-section $S = 2\pi ae$ and the moment of inertia $I_y^b = \pi ae\left(a^2 + \frac{e^2}{12}\right) \approx \pi a^3 e$.
Without considering external forces, i.e. $\mathcal{P}_e = 0$, the equations of motion write:

$$\begin{cases} \rho S\dfrac{\partial^2 U_o}{\partial t^2} & - & \dfrac{\partial N}{\partial x} & = & 0 \\ \rho S\dfrac{\partial^2 V_o}{\partial t^2} - \rho I_y^b\dfrac{\partial^4 V_o}{\partial t^2\partial x^2} & - & \dfrac{\partial^2 M_y}{\partial x^2} & = & 0 \\ \rho S\left(\dfrac{\partial^2 w_o^c}{\partial t^2} - \dfrac{e^2}{12}\dfrac{\partial^4 w_o^c}{\partial t^2\partial x^2}\right) & - & \dfrac{\partial^2 (m_w)_o^c}{\partial x^2} + (t_w)_o^c & = & 0 \end{cases} \tag{32}$$

Note that for a plate element with uniform material properties, the ratio between the moment of inertia and the area of the cross-section corresponds to $e^2/12$ which thus takes the same role as I_y/S for the shell-type DOFs.
The static counterpart of Eq. (32) corresponds to:

$$\frac{\partial N}{\partial x} = 0; \quad \frac{\partial^2 M_y}{\partial x^2} = 0; \quad -\frac{\partial^2 (m_w)_o^c}{\partial x^2} + (t_w)_o^c = 0 \tag{33}$$

For the considered behavior given in Eq. (25), the generalized forces are given by:

$$\begin{aligned} N &= \frac{ES}{1-\nu^2}\left(\frac{\partial U_o}{\partial x} + \nu\frac{w_o^c}{a}\right) \quad ; \quad M_y = -\frac{EI_y^b}{1-\nu^2}\frac{\partial^2 V_o}{\partial x^2} \quad ; \\ (t_w)_o^c &= \frac{ES}{1-\nu^2}\frac{1}{a}\left(\nu\frac{\partial U_o}{\partial x} + \frac{w_o^c}{a}\right) \quad ; \quad (m_w)_o^c = -\frac{ES}{1-\nu^2}\frac{e^2}{12}\frac{\partial^2 w_o^c}{\partial x^2} \end{aligned} \tag{34}$$

where N corresponds to the beam-type axial force with an additional term involving the pipe radial contraction/expansion corresponding to the Poisson effect, M_y to the beam in-plane bending moment whereas $(t_w)_o^c$ corresponds to the radial force divided by the mean radius and $(m_w)_o^c$ to the bending moment of the mid-surface in the $(\mathbf{E}_x, \mathbf{E}_R)$ plane. Eqs. (32) and (34) correspond to Eqs. (B.15) and (B.16) described in Appendix B.

Note that, without considering the Poisson effect, the two first equations in Eq. (32) correspond to the classical straight Euler-Bernoulli beam governing equations which, for example, are given in [35]. In addition, it has to be noticed that Eq. (32) correspond to the axisymmetric thin-shell cylinder equations of motion as expressed in [36] where the terms $e^2/12a$ is neglected due to the thin-walled assumption and thus the integration over $a\ \mathrm{d}\theta\mathrm{d}z$ instead of $(a+z)\ \mathrm{d}\theta\mathrm{d}z$. Finally, neglecting the $\partial^2_{x^2}\,(m_w)_o^c$ term in Eq. (32) makes it possible to retrieve the equations of motion proposed by Walker & Phillips [37] for an axisymmetric small-deformed elastic plane-stressed tube as also reported in the review [3].

2.5. Governing equations and generalized forces for Fourier mode 2

Only the second Fourier mode is here considered corresponding to the cross-section ovalization. As in [8, 11], only the shell membrane deformations are considered (i.e. for shell-type DOFs $\mathbf{k} = \mathbf{0}$ except $k_{\theta\theta} \neq 0$)). The assumption of the section inextensibility is taken into account (see Eq. (14)) as well as the non-linear coupling terms. As a consequence, for an in-plane motion, the considered shell kinematics of the mid-surface writes:

$$u_o(t,x,\theta) = 0, \quad w_o(t,x,\theta) = w_2^c(t,x)\cos(2\theta), \quad v_o(t,x,\theta) = -\frac{1}{2}w_2^c(t,x)\sin(2\theta) \tag{35}$$

The strain tensor is thus given by:

$$\begin{cases} \varepsilon_{xx} = \dfrac{\partial U_o}{\partial x} - \left[(a+z)\sin\theta + h_o\right]\dfrac{\partial^2 V_o}{\partial x^2} \\ \varepsilon_{\theta\theta} = 3\dfrac{z}{a^2}\cos(2\theta)\, w_2^c \\ 2\,\varepsilon_{x\theta} = -\dfrac{1}{2}\sin(2\theta)\dfrac{\partial w_2^c}{\partial x} \end{cases} \quad \text{with} \quad h_o = \left(\cos(2\theta)\sin\theta - \frac{1}{2}\sin(2\theta)\cos\theta\right) w_2^c \tag{36}$$

After some algebraic manipulations, the power of internal forces leads to the following expression:

$$\mathcal{P}_i = -\int_0^L \left(N\frac{\partial \delta U_o}{\partial x} - M_y\frac{\partial^2 \delta V_o}{\partial x^2} + (t_w)_2^c\,\delta w_2^c + (n_w)_2^c\,\frac{\partial \delta w_2^c}{\partial x}\right)\mathrm{d}x \tag{37}$$

where the generalized forces are defined as:

$$\begin{aligned} N &= \int_S \sigma_{xx}\ \mathrm{d}S \\ M_y &= \int_S \sigma_{xx}\left[(a+z)\sin\theta + h_o\right]\ \mathrm{d}S \\ (t_w)_2^c &= \int_S \left(\frac{1}{2}\sigma_{xx}\left(\sin(2\theta)\cos\theta - 2\cos(2\theta)\sin\theta\right)\frac{\partial^2 V_o}{\partial x^2} + 3\frac{z}{a^2}\sigma_{\theta\theta}\cos(2\theta)\right)\mathrm{d}S \\ (n_w)_2^c &= -\int_S \frac{1}{2}\sigma_{x\theta}\sin(2\theta)\ \mathrm{d}S \end{aligned} \tag{38}$$

Without considering external forces, i.e. $\mathcal{P}_e = 0$, the equations of motion write:

$$\left\{\begin{array}{lcll} \rho S\dfrac{\partial^2 U_o}{\partial t^2} & - & \dfrac{\partial N}{\partial x} & = 0 \\ \rho S\dfrac{\partial^2 V_o}{\partial t^2} - \rho I_y \dfrac{\partial^4 V_o}{\partial t^2 \partial x^2} & - & \dfrac{\partial^2 M_y}{\partial x^2} & = 0 \\ \rho S\dfrac{1}{2}\left(\dfrac{5}{4}\dfrac{\partial^2 w_2^c}{\partial t^2} - \dfrac{e^2}{12}\dfrac{\partial^4 w_2^c}{\partial t^2 \partial x^2}\right) & - & \dfrac{\partial (n_w)_2^c}{\partial x} + (t_w)_2^c & = 0 \end{array}\right. \tag{39}$$

with the moment of inertia given by:

$$I_y = \pi a^3 e\left(1 + \frac{e^2}{12a^2} - \frac{3}{2}\frac{w_2^c}{a} + \frac{5}{8}\left(\frac{w_2^c}{a}\right)^2\right) \approx \pi a^3 e\left(1 - \frac{3}{2}\frac{w_2^c}{a} + \frac{5}{8}\left(\frac{w_2^c}{a}\right)^2\right)$$

where $I_y^b \approx \pi a^3 e$.
In a similar way, the equilibrium equations in static are obtained as:

$$\frac{\partial N}{\partial x} = 0 \quad ; \quad \frac{\partial^2 M_y}{\partial x^2} = 0 \quad ; \quad \frac{\partial (n_w)_2^c}{\partial x} - (t_w)_2^c = 0 \tag{40}$$

With the behavior law given in Eq. (25), the generalized forces are expressed as:

$$\begin{aligned} N &= +\frac{ES}{1-\nu^2}\frac{\partial U_o}{\partial x} \quad ; \quad \xi = \frac{w_2^c}{a} \\ M_y &= -\frac{EI_y^b}{1-\nu^2}\left(1 - \frac{3}{2}\xi + \frac{5}{8}\xi^2\right)\frac{\partial^2 V_o}{\partial x^2} \\ (t_w)_2^c &= +\frac{ES}{1-\nu^2}\frac{1}{2}\left(\left(-\frac{3}{4} + \frac{5}{8}\xi\right)a\left(\frac{\partial^2 V_o}{\partial x^2}\right)^2 + 3\frac{e^2}{4a^2}\frac{1}{a}\xi\right) \\ (n_w)_2^c &= +\frac{ES}{1+\nu}\frac{1}{16}a\frac{\partial \xi}{\partial x} \end{aligned} \tag{41}$$

As previously, N corresponds the beam-type axial force and M_y to the beam in-plane bending moment. For the shell DOFs, $(t_w)_2^c$ corresponds to a force divided by the mean radius and $(n_w)_2^c$ to a shear-type force. Eqs. (39) and (41) correspond to Eqs. (B.17) and (B.18) described in Appendix B.

Due to the non-linear coupling between the tube cross-section deformation (here linked to w_2^c) and the rotation of the tube axis, i.e. $-\partial_x V_o$, the in-plane bending moment M_y depends on terms in w_2^c and, in a similar way, terms in $\partial_x V_o$ are involved in the expression of $(t_w)_2^c$. Let consider the curvature κ defined as:

$$\kappa = \frac{a^2}{e}\left(-\frac{\partial^2 V_o}{\partial x^2}\right)$$

In the case of Euler-Bernoulli beams and in the case of Fourier mode 0 described previously, it appears that the bending moment M_y is linear with respect to the curvature κ as the inertia remains constant. In contrast, in the present model involving both the Fourier mode 2 and the non-linear coupling, due to the terms in ξ in the expression of the bending moment, the inertia of the section can change with its deformation leading to a non-linear relation between M_y and κ. Comparison between the different moment-curvature and ovalization-curvature relationships encountered in the literature is performed in [34]. The ovalization-curvature are obtained taking $(t_w)_2^c$ equal to zero. For example, considering only the first-order terms in the expressions of M_y and $(t_w)_2^c$, i.e.

$$M_y = -\frac{EI_y^b}{1-\nu^2}\left(1 - \frac{3}{2}\xi\right)\frac{\partial^2 V_o}{\partial x^2} \quad \text{and} \quad (t_w)_2^c = \frac{ES}{1-\nu^2}\frac{3}{8}\left(-a\left(\frac{\partial^2 V_o}{\partial x^2}\right)^2 + \frac{e^2}{a^3}\xi\right)$$

leads to the following moment-curvature and ovalization-curvature relationships:

$$M_y = K\left(1 - \frac{3}{2}\xi\right)\kappa \quad \text{and} \quad \xi = \kappa^2$$

with K a constant. This exactly corresponds to the relationships initially derived by Brazier [33]. Then, considering the second-order terms in Eq. 41 leads to the following moment-curvature and ovalization-curvature relationships:

$$M_y = K\left(1 - \frac{3}{2}\xi + \frac{5}{8}\xi^2\right)\kappa \quad \text{and} \quad \xi = \frac{\kappa^2}{1 + \frac{5}{6}\kappa^2}$$

which corresponds to the relationships referred to as modified Brazier initially straight tubes in [34].

2.6. Higher Fourier modes

The derivation of both governing equations and generalized forces has been presented previously when only considering Fourier mode 0 or Fourier mode 2. Taking into account higher Fourier modes together makes this derivation more complex, especially due to the coupling between different modes. The corresponding tube governing equations are derived in Appendix B and are expressed in Eq. (B.14). The generalized forces are given in Eqs. (B.9), (B.10), (B.11), (B.12) and (B.13). In addition, mathematical tools dedicated to formal computation such as Sympy (`https://www.sympy.org`) and wxMaxima (`https://wxmaxima-developers.github.io/wxmaxima/`) have been used for verification.

2.7. Further discussion on the kinematics of the present element and comparison with previous beam elements

As shown in the previous sections, the present tube element is here derived in the context of thin-walled tubular geometries. Even if a full 3-D motion has been considered in the derivation of this element, only an in-plane motion is presented for simplicity. As described previously, the kinematics is obtained through the enrichment of straight beam kinematics by the addition of orthogonal shell-type displacement field of the tube cross-section. The corresponding displacement field is here composed of three contributions: linear beam and shell terms in conjunction with a non-linear coupling between cross-section deformation and rotation of the tube axis. First, concerning the beam-type DOFs of the proposed tube model, as shown in the derivation of the generalized forces (cf. Appendix B.2), the classical Euler-Bernoulli beam is recovered plus the consideration of the Poisson effect which is derived from the link between beam and shell. Then, concerning the shell-type motion, the present tube element incorporates all the elements reviewed in Weicker [14] including the elements previously proposed in [6, 7, 8, 9, 10, 11, 13] as complete Fourier series for warping, ovalization and radial deformations of the mid-surface are considered. In addition, as shown in Appendix B.4, the present tube kinematics incorporates the circular shell kinematics as the corresponding circular cylindrical shells equations of motion can be retrieved from the present formulation. What is more, via the consideration of the non-linear coupling, the inertia of the section can change with its deformation as described in Brazier [33]. As a consequence, the present tube element seems to present the simplest kinematics able to consider both deformations of its cross-section and changes of inertia as only one non-linear coupling term is considered for this purpose. However, this single non-linear term is not sufficient to describe all possible local and global buckling as it is performed in [34]. In addition, the previous elements have been derived for static analysis whereas the present one is considered for explicit dynamic analysis.

In the following section, the numerical method used to solve the derived tube model is detailed.

3. Numerical approximations: an explicit updated Lagrangian Finite-Element approach

The governing equations are here discretized using an explicit updated Lagrangian Finite-Element approach which is described in the following. For simplicity, the numerical methods are detailed in the case where only the 0-mode is considered in the Fourier expansion as described in Sec. 2.4 and the extension to higher Fourier modes is briefly discussed. In addition, even if the numerical method as well as the tube element have been derived for a 3-D motion, only an in-plane motion is presented in the following for simplicity. The time integration is performed using the explicit central difference operator whose stability condition is given considering both beam and shell contributions.

3.1. Nodal unknowns and shape functions

By means of the Finite-Element method, the spatial domain of the beam is discretized into a number of sub-domains named here tube element. Each element has two nodes and the vector of nodal generalized displacements is defined as:

$$\mathbf{d}_e = \left(\mathbf{d}_e^1,\, \mathbf{d}_e^2\right)^T \quad \text{where} \quad \mathbf{d}_e^i = \left(U_o^i,\; V_o^i,\; \Omega_y^i,\; \left(w_o^c\right)^i,\; u_1^i\right)^T \tag{42}$$

when only Fourier mode 0 is here considered. The subscript e associates a given quantity with a typical tube element whereas the superscript $i = 1, 2$ associates a given quantity with the corresponding node of the considered tube element. The length of the element is denoted by ℓ_e. Due to the assumption of small deformations, the length of the tube element is assumed to be the same as the initial undeformed element, i.e. $\ell_e^n = \ell_e^o$ where the superscript n denotes the time level. Shape functions are used to approximate the displacement field inside the tube element of any arbitrary point located at the beam axis for the beam-type DOFs and at the mid-surface of the tube for the shell-type DOFs. In addition, the displacement field is assumed to satisfy the conditions imposed by the tube kinematics, in particular the Euler-Bernoulli and the Love-Kirchhoff hypotheses:

$$\Omega_y + \frac{\partial V_o}{\partial x} = 0 \quad \text{and} \quad u_1 = \frac{\partial w_o^c}{\partial x} \tag{43}$$

To this end, for the beam-type DOFs, linear and cubic interpolating polynomials are chosen to approximate, respectively, the axial and transverse neutral fiber displacements within each tube element whereas cubic shape functions are used for the mid-surface displacements for the shell-type DOFs. As a consequence the displacement field within the tube element is approximated using $\mathbf{N}_e$ the matrix of shape functions as follows:

$$\overline{\mathbf{d}}_e = \mathbf{N}_e\, \mathbf{d}_e \quad \text{with} \quad \mathbf{N}_e = \left(\mathbf{N}_e^1\; \mathbf{N}_e^2\right) \quad \text{and} \quad \mathbf{N}_e^i = \begin{pmatrix} N_{U_o^i} & 0 & 0 & 0 & 0 \\ 0 & N_{V_o^i} & N_{\Omega_y^i} & 0 & 0 \\ 0 & -\frac{\mathrm{d}N_{V_o^i}}{\mathrm{d}x} & -\frac{\mathrm{d}N_{\Omega_y^i}}{\mathrm{d}x} & 0 & 0 \\ 0 & 0 & 0 & N_{(w_o^c)^i} & N_{u_1^i} \\ 0 & 0 & 0 & \frac{\mathrm{d}N_{(w_o^c)^i}}{\mathrm{d}x} & \frac{\mathrm{d}N_{u_1^i}}{\mathrm{d}x} \end{pmatrix} \tag{44}$$

with the following shape functions:

$$\begin{cases} N_{U_o^1} &= 1-\lambda \\ N_{V_o^1} = N_{(w_o^c)^1} &= (\lambda-1)^2(2\lambda+1) \\ N_{\Omega_y^1} = -N_{u_1^1} &= -\ell_e\lambda(\lambda-1)^2 \end{cases} \quad \text{and} \quad \begin{cases} N_{U_o^2} &= \lambda \\ N_{V_o^2} = N_{(w_o^c)^2} &= \lambda^2(3-2\lambda) \\ N_{\Omega_y^2} = -N_{u_1^2} &= -\ell_e\lambda^2(\lambda-1) \end{cases}$$

with $\lambda = x/\ell_e$ where ℓ_e corresponds to the length of the tube element.

We can also note that the tube displacement field given in Eq. (27) can be expressed as:

$$\mathbf{U} = \mathbf{T}\,\overline{\mathbf{d}}_e \quad \text{with} \quad \mathbf{T} = \begin{pmatrix} 1 & 0 & (a+z)\sin\theta & 0 & -z \\ 0 & \sin\theta & 0 & 1 & 0 \\ 0 & \cos\theta & 0 & 0 & 0 \end{pmatrix} \tag{45}$$

as the non-linear coupling term is here neglected.

For the discretized pipe, the virtual power principle (see Eqs. (20) and (29)) writes:

$$\sum_e \left(\int_{V_e} \rho \frac{\partial^2 \mathbf{U}}{\partial t^2} \cdot \delta\,\mathbf{U}\,\mathrm{d}V\right) = -\sum_e \left[\int_0^{\ell_e} \left(N\frac{\partial \delta U_o}{\partial x} + M_y\left(-\frac{\partial^2 \delta V_o}{\partial x^2}\right) + (t_w)_o^c\,\delta w_o^c - (m_w)_o^c\,\frac{\partial^2 \delta w_o^c}{\partial x^2}\right)\mathrm{d}x\right] \tag{46}$$

with V_e the volume of the tube element and considering the sum over the tube elements. This can be rewritten in the following form:

$$\sum_e \left[\int_{V_e} \left(\rho\,(\delta\,\mathbf{U})^T\,\frac{\partial^2 \mathbf{U}}{\partial t^2}\right)\mathrm{d}V\right] = -\sum_e \left[\int_0^{\ell_e} \left((\delta\,\mathbf{E})^T\;\mathbf{F}\right)\mathrm{d}x\right] \tag{47}$$

with the generalized force vector $\mathbf{F}$ and the generalized strain vector $\mathbf{E}$ defined as:

$$\mathbf{F} = \left(N,\ M_y,\ (t_w)_o^c,\ (m_w)_o^c\right)^T \quad \text{and} \quad \mathbf{E} = \left(\frac{\partial U_o}{\partial x},\ -\frac{\partial^2 V_o}{\partial x^2},\ w_o^c,\ -\frac{\partial^2 w_o^c}{\partial x^2}\right)^T$$

which are related using the constitutive matrix denoted here by $\mathbf{D}$ as follows:

$$\mathbf{F} = \mathbf{D}\,\mathbf{E} \quad \text{with} \quad \mathbf{D} = \frac{ES}{1-\nu^2}\begin{pmatrix} 1 & 0 & \frac{\nu}{a} & 0 \\ 0 & \frac{I_y}{S} & 0 & 0 \\ \frac{\nu}{a} & 0 & \frac{1}{a^2} & 0 \\ 0 & 0 & 0 & \frac{e^2}{12} \end{pmatrix}$$

With the assumed displacement field within the tube element, the vector $\mathbf{E}$ can be expressed using the nodal displacement vector, i.e. $\mathbf{E} = \mathbf{B}_e\,\mathbf{d}_e$, with the strain-displacement matrix $\mathbf{B}_e$ given by:

$$\mathbf{B}_e = \left(\mathbf{B}_e^1\ \mathbf{B}_e^2\right) \quad \text{with} \quad \mathbf{B}_e^i = \begin{pmatrix} \frac{\mathrm{d}N_{U_o^i}}{\mathrm{d}x} & 0 & 0 & 0 & 0 \\ 0 & \frac{\mathrm{d}^2 N_{V_o^i}}{\mathrm{d}x^2} & \frac{\mathrm{d}^2 N_{\Omega_y^i}}{\mathrm{d}x^2} & 0 & 0 \\ 0 & 0 & 0 & N_{(w_o^c)^i} & N_{u_1^i} \\ 0 & 0 & 0 & \frac{\mathrm{d}^2 N_{(w_o^c)^i}}{\mathrm{d}x^2} & \frac{\mathrm{d}^2 N_{u_1^i}}{\mathrm{d}x^2} \end{pmatrix}$$

With the previous notations, the virtual power principle can be expressed as:

$$\sum_e \left[(\delta\,\mathbf{d}_e)^T\ \mathbf{M}_e\,\ddot{\mathbf{d}}_e\right] = -\sum_e \left[(\delta\,\mathbf{d}_e)^T\ \mathbf{f}_{e,\text{int}}\right] \tag{48}$$

with the consistent mass matrix $\mathbf{M}_e$ and the nodal internal forces vector $\mathbf{f}_{e,\text{int}}$ defined by:

$$\mathbf{M}_e = \int_{V_e} \rho \mathbf{N}_e^T \mathbf{T}^T \mathbf{T} \mathbf{N}_e\ \mathrm{d}V \quad \text{and} \quad \mathbf{f}_{e,\text{int}} = \int_0^{\ell_e} \mathbf{B}_e^T\,\mathbf{F}\ \mathrm{d}x$$

The internal forces are approximated using a Gauss quadrature approach:

$$\mathbf{f}_{e,\text{int}} = \int_0^{\ell_e} \mathbf{B}_e^T\,\mathbf{F}\ \mathrm{d}x \approx \sum_{j=1}^{N_G} \omega_j \mathbf{B}_e^T\left(\lambda_j\right)\,\mathbf{F}\left(\lambda_j\right) \tag{49}$$

with N_G the number of Gauss points used for the present tube element, ω_j and λ_j the weight and location of each Gauss point, respectively. The number of Gauss points as well as the corresponding weights and locations depends on the order of the polynomials used in $\mathbf{B}_e^T\,\mathbf{F}$. Due to the presence of the cubic interpolating functions $N_{(w_o^c)^i}$ for $i = 1, 2$, a polynomial of power six is involved as $\mathbf{F} = \mathbf{D}\mathbf{B}_e\,\mathbf{d}_e$. A four-point Gauss rule is thus necessary to integrate this six-order polynomial function in an exact manner, i.e. $N_G = 4$, with the following weights and locations:

$$\begin{aligned} \lambda_1 &= 0.0694318442, \quad \omega_1 = 0.1739274226\ \ell_e \\ \lambda_2 &= 0.3300094782, \quad \omega_2 = 0.3260725774\ \ell_e \\ \lambda_3 &= 0.6699905218, \quad \omega_3 = 0.3260725774\ \ell_e \\ \lambda_4 &= 0.9305615580, \quad \omega_4 = 0.1739274226\ \ell_e \end{aligned}$$

In the case of the standard Euler-Bernoulli beam element, only two Gauss points are required as described in [35, 38, 39].

3.2. Consistent and lumped mass matrices

Based on the assumed displacement field within the tube element, the consistent mass matrix has the following explicit form:

$$\mathbf{M}_e = \begin{pmatrix} \mathbf{M}_e^{11} & \mathbf{M}_e^{12} \\ \mathbf{M}_e^{21} & \mathbf{M}_e^{22} \end{pmatrix} \quad \text{with} \quad \mathbf{M}_e^{ij} = \int_{V_e} \rho \left(\mathbf{N}_e^i\right)^T \mathbf{T}^T \mathbf{T} \mathbf{N}_e^j\ \mathrm{d}V$$

as $\mathbf{M}_e^{ji} = \left(\mathbf{M}_e^{ij}\right)^T$, the consistent mass matrix is symmetric and its components are given by:

$$\mathbf{M}_e^{11} = \rho S \ell_e \begin{pmatrix} \frac{1}{3} & 0 & 0 & 0 & 0 \\ 0 & \frac{13}{35} + \frac{6}{5}\frac{I_y}{S\ell_e} & -\frac{11\ell_e}{210} - \frac{1}{10}\frac{I_y}{S\ell_e} & 0 & 0 \\ 0 & -\frac{11\ell_e}{210} - \frac{1}{10}\frac{I_y}{S\ell_e} & \frac{\ell_e^2}{105} + \frac{2}{15}\frac{I_y}{S} & 0 & 0 \\ 0 & 0 & 0 & \frac{13}{35} + \frac{6}{5}\frac{e^2}{12\ell_e^2} & -\frac{11\ell_e}{210} - \frac{1}{10}\frac{e^2}{12\ell_e} \\ 0 & 0 & 0 & -\frac{11\ell_e}{210} - \frac{1}{10}\frac{e^2}{12\ell_e} & \frac{\ell_e^2}{105} + \frac{2}{15}\frac{e^2}{12} \end{pmatrix}$$

$$\mathbf{M}_e^{22} = \rho S \ell_e \begin{pmatrix} \frac{1}{3} & 0 & 0 & 0 & 0 \\ 0 & \frac{13}{35} + \frac{6}{5}\frac{I_y}{S\ell_e} & \frac{11\ell_e}{210} + \frac{1}{10}\frac{I_y}{S\ell_e} & 0 & 0 \\ 0 & \frac{11\ell_e}{210} + \frac{1}{10}\frac{I_y}{S\ell_e} & \frac{\ell_e^2}{105} + \frac{2}{15}\frac{I_y}{S} & 0 & 0 \\ 0 & 0 & 0 & \frac{13}{35} + \frac{6}{5}\frac{e^2}{12\ell_e^2} & \frac{11\ell_e}{210} + \frac{1}{10}\frac{e^2}{12\ell} \\ 0 & 0 & 0 & \frac{11\ell_e}{210} + \frac{1}{10}\frac{e^2}{12\ell_e} & \frac{\ell_e^2}{105} + \frac{2}{15}\frac{e^2}{12} \end{pmatrix}$$

$$\mathbf{M}_e^{12} = \rho S \ell_e \begin{pmatrix} \frac{1}{6} & 0 & 0 & 0 & 0 \\ 0 & \frac{9}{70} - \frac{6}{5}\frac{I_y}{S\ell_e} & \frac{13\ell_e}{420} - \frac{1}{10}\frac{I}{S\ell_e} & 0 & 0 \\ 0 & -\frac{13\ell_e}{420} + \frac{1}{10}\frac{I_y}{S\ell_e} & -\frac{\ell_e^2}{140} - \frac{1}{30}\frac{I_y}{S} & 0 & 0 \\ 0 & 0 & 0 & \frac{9}{70} - \frac{6}{5}\frac{e^2}{12\ell_e^2} & \frac{13\ell_e}{420} - \frac{1}{10}\frac{e^2}{12\ell_e} \\ 0 & 0 & 0 & -\frac{13\ell_e}{210} + \frac{1}{10}\frac{e^2}{12\ell_e} & -\frac{\ell_e^2}{140} - \frac{1}{30}\frac{e^2}{12} \end{pmatrix} \quad \text{and} \quad \mathbf{M}_e^{21} = \left(\mathbf{M}_e^{12}\right)^T$$

Note that the first 3×3 block-matrix of each component of the mass matrix of the present tube element corresponds exactly to the component of the consistent mass matrix of the Euler-Bernoulli beam element as described in [35, 38]. As an explicit time integration is retained in the following, the use of lumped or diagonal mass matrix in place of the consistent mass matrix is classically used to enhance the computational efficiency of the explicit scheme. For the Euler-Bernoulli beam element described in [35] with both translational and rotational DOFs, the lumping of the mass matrix is performed as follows. Concerning the translational terms, a "row-sum" approach is used. This also corresponds to the element mass preservation by dividing the total mass among the diagonal entries of the mass matrix and setting all other entries to zero. This leads to the diagonal term: $\rho S \ell_e/2$. In contrast, for the rotational terms, the lumping is performed by ignoring the off-diagonal terms of the consistent mass matrix and scaling the term involving inertia in the diagonal term as performed in [38, 35]. The same procedure is here used for both beam and shell translational and rotational DOFs leading to the following lumped mass matrix:

$$\tilde{\mathbf{M}}_e = \begin{pmatrix} \tilde{\mathbf{M}}_e^{11} & \mathbf{0} \\ \mathbf{0} & \tilde{\mathbf{M}}_e^{22} \end{pmatrix} \quad \text{with} \quad \tilde{\mathbf{M}}_e^{11} = \tilde{\mathbf{M}}_e^{22} = \rho S \ell_e \begin{pmatrix} \frac{1}{2} & 0 & 0 & 0 & 0 \\ 0 & \frac{1}{2} & 0 & 0 & 0 \\ 0 & 0 & \frac{\ell_e^2}{105} + \frac{I_y}{S} & 0 & 0 \\ 0 & 0 & 0 & \frac{1}{2} & 0 \\ 0 & 0 & 0 & 0 & \frac{\ell_e^2}{105} + \frac{e^2}{12} \end{pmatrix} \tag{50}$$

where the same scaling is used for the terms I_y/S and $e^2/12$ in the rotational beam and shell DOFs, respectively.

The local coordinate system for each tube element has been used for expressing the nodal displacement vector $\mathbf{d}_e$. In order to express the unknowns in the global coordinate system, the transformation matrix is used $\mathbf{P}_e$. Note that the present lumped mass matrix is independent of the coordinate system, i.e. $\mathbf{P}_e \tilde{\mathbf{M}}_e \mathbf{P}_e^T = \tilde{\mathbf{M}}_e$. The assembly is then obtained through the sum over the elements after the connectivity transformation:

$$\mathbf{P}_e \, \mathbf{d}_e = \mathbf{C}_e \, \mathbf{d} \tag{51}$$

with $\mathbf{d}$ the global displacement expressed in generalized coordinates and $\mathbf{C}_e$ the connectivity matrix associated with the finite element in question. As the two displacement vectors $\mathbf{P}_e \, \mathbf{d}_e$ and $\mathbf{d}$ are expressed in the same coordinate

system, the $\mathbf{C}_e$ matrices are simply Boolean matrices. Finally, this leads to the following relation:

$$\mathbf{d}^T \mathbf{M}\, \ddot{\mathbf{d}} = -\,\mathbf{d}^T\, \mathbf{f}_{\text{int}} \quad \text{or equivalently} \quad \tilde{\mathbf{M}}\, \ddot{\mathbf{d}} = -\,\mathbf{f}_{\text{int}} \tag{52}$$

with $\tilde{\mathbf{M}} = \sum_e \left(\mathbf{C}_e^T \tilde{\mathbf{M}}_e \mathbf{C}_e \right)$ the global lumped mass matrix and $\mathbf{f}_{\text{int}} = \sum_e \left(\mathbf{C}_e^T \mathbf{P}_e\, \mathbf{f}_{e,\text{int}} \right)$ the global internal force vector.

3.3. Explicit central difference scheme

The explicit time integration of Eq. (52) is here performed using the central difference operator leading to:

$$\begin{cases} \dot{\mathbf{d}}^{n+1/2} &= \dot{\mathbf{d}}^n + \Delta t^n\, \ddot{\mathbf{d}}^n/2 \\ \mathbf{d}^{n+1} &= \mathbf{d}^n + \Delta t^n\, \dot{\mathbf{d}}^{n+1/2} \\ \ddot{\mathbf{d}}^{n+1} &= \left(\tilde{\mathbf{M}}^{n+1} \right)^{-1} \left(\mathbf{f}_{\text{ext}}^{n+1} - \mathbf{f}_{\text{int}}^{n+1} \right) \\ \dot{\mathbf{d}}^{n+1} &= \dot{\mathbf{d}}^{n+1/2} + \Delta t^n\, \ddot{\mathbf{d}}^{n+1}/2 \end{cases} \tag{53}$$

with $\mathbf{d}$, $\dot{\mathbf{d}}$ and $\ddot{\mathbf{d}}$ the nodal displacements, velocities and accelerations, $\mathbf{f}_{\text{int}}$ and $\mathbf{f}_{\text{ext}}$ the nodal internal and external forces, respectively, the superscript n denoting the time level. As the inertia of the section can evolve, the lumped mass matrix is updated at each time step.

The explicit central difference scheme is one of the most popular explicit time integration operator due to its simplicity and its second-order accuracy in time. In addition, in the case of constant time step, this scheme is known to be non-dissipative [40].

3.4. Extension to higher Fourier modes

The previous derivation has been detailed for $N_f = 0$ in the Fourier expansion described previously and for an in-plane motion. Considering the Fourier mode 1 leads to the integration of the two following additional DOFs w_1^s and $\frac{\partial w_1^s}{\partial x}$ for an in-plane motion in the generalized displacement vector $\mathbf{d}_e^i$. Cubic interpolating shape functions are thus used for w_1^s. Then, considering the k-th Fourier mode for $k \geq 2$ induces to take into account three additional DOFs for an in-plane motion, i.e. u_k^m, w_k^m and $\frac{\partial w_k^m}{\partial x}$ with $m = s$ if k is impair and $m = c$ if k is pair. As a consequence, linear shape functions are used for u_k^m whereas cubic shape function for w_k^m. For the same reason as previously, a 4-point Gauss quadrature approach is still used for the computation of the internal forces (cf. Eq. (49)) even if higher Fourier modes are considered. In addition, the lumped mass matrix of the tube element is modified in Eq. (50) as follows:

$$\tilde{\mathbf{M}}_e^{11} = \tilde{\mathbf{M}}_e^{22} = \rho S \ell_e \begin{pmatrix} \frac{1}{2} & 0 & 0 & 0 & 0 & 0 & 0 & \dots & 0 & 0 & 0 & \dots \\ 0 & \frac{1}{2} & 0 & 0 & 0 & 0 & 0 & \dots & 0 & 0 & 0 & \dots \\ 0 & 0 & \frac{\ell_e^2}{105} + \frac{I_y}{S} & 0 & 0 & 0 & 0 & \dots & 0 & 0 & 0 & \dots \\ 0 & 0 & 0 & \frac{1}{2} & 0 & 0 & 0 & \dots & 0 & 0 & 0 & \dots \\ 0 & 0 & 0 & 0 & \frac{\ell_e^2}{105} + \frac{e^2}{12} & 0 & 0 & \dots & 0 & 0 & 0 & \dots \\ 0 & 0 & 0 & 0 & 0 & \frac{1}{2} & 0 & \dots & 0 & 0 & 0 & \dots \\ 0 & 0 & 0 & 0 & 0 & 0 & \frac{\ell_e^2}{105} + \frac{e^2}{12} & \dots & 0 & 0 & 0 & \dots \\ \vdots & \vdots & \vdots & \vdots & \vdots & \vdots & \vdots & \ddots & \vdots & \vdots & \vdots & \vdots \\ 0 & 0 & 0 & 0 & 0 & 0 & 0 & \dots & \frac{1}{2} & 0 & 0 & \dots \\ 0 & 0 & 0 & 0 & 0 & 0 & 0 & \dots & 0 & \frac{1}{2} & 0 & \dots \\ 0 & 0 & 0 & 0 & 0 & 0 & 0 & \dots & 0 & 0 & \frac{\ell_e^2}{105} + \frac{e^2}{12} & \dots \\ \vdots & \vdots & \vdots & \vdots & \vdots & \vdots & \vdots & \vdots & \vdots & \vdots & \vdots & \ddots \end{pmatrix} \tag{54}$$

where the first 3×3 block diagonal matrix corresponds to the standard Euler-Bernoulli lumped mass matrix [35, 39], the following 2×2 block diagonal matrix corresponds to the Fourier mode 0, the next 2×2 block diagonal to the Fourier mode 1 and the next 3×3 to the Fourier mode i. The diagonal term for the transitional DOFs for both beam and shell is $\rho S \ell_e/2$, whereas the term of the rotational DOFs for beam and shell are $\rho S \ell_e \left(\ell_e^2/105 + I_y/S \right)$ and $\rho S \ell_e \left(\ell_e^2/105 + e^2/12 \right)$ respectively.

3.5. Stability condition and time step evaluation

For the explicit time integration of an undamped system with the central difference operator, the time step Δt^n used in Eq. (53) has to respect the following stability condition [41, 42]:

$$\Delta t^n = C\Delta t^n_{\text{crit}} \quad \text{with} \quad \Delta t^n_{\text{crit}} = \frac{2}{\omega^n_{\max}} \tag{55}$$

where $0 < C \leq 1$ is the Courant number, Δt^n_{crit} the critical time step and $\omega^n_{\max}$ the maximum eigenvalue of the system which is classically bounded by the largest element eigenvalue:

$$\omega^n_{\max} \leq \max_e \left(\omega^n_{e,\max}\right) \tag{56}$$

with $\omega^n_{e,\max}$ the maximum eigenvalue of the e-th element, unrestrained.

Therefore, to express the stability condition, the expression of the maximum frequency of the proposed tube element is required. Instead of solving the eigenvalue problem which can be complex in the case of the present element especially when considering higher Fourier modes, this is here performed using the natural frequencies of beams and cylindrical shells which are given in [43]. Even if only an in-plane motion is presented in the previous sections for simplicity, we recall that a full 3-D motion is derived. As a consequence, all the corresponding contributions have been also considered for numerical stability. Finally, the maximum element eigenvalue corresponds to the maximum of the eigenvalues associated to all of the contributions of the present tube element:

$$\omega^n_{e,\max} = \max\left(\omega^n_{e,\text{b}}, \omega^n_{e,\text{s}}\right) \tag{57}$$

where for the beam-type contribution, i.e. beam axial and beam flexural, as described in [35, 39]:

$$\omega^n_{e,\text{b}} = \max\left(\frac{2}{\ell_e}\sqrt{\frac{E}{\rho}}, \frac{2}{\ell_e^2}\sqrt{\frac{EI_y}{\rho S}\pi^4}\right) \tag{58}$$

and the natural frequencies of cylindrical shells as expressed in [43] in terms of a dimensionless frequency parameter λ are given by:

$$\omega^n_{e,\text{s}} = \frac{2\lambda}{a}\sqrt{\frac{E}{\rho\left(1-\nu^2\right)}} \tag{59}$$

with the following expressions of the dimensionless frequency parameter λ:

$$\lambda = \begin{cases} \lambda^{\text{r}} = 1 & \text{for the radial tube mode} \\ \lambda^{\text{a}} = \dfrac{a}{\ell_e}\sqrt{\left(1-\nu^2\right)\pi^2} & \text{for the axial tube mode} \\ \lambda^{\text{t}} = \dfrac{a}{\ell_e}\sqrt{\left(\dfrac{1-\nu^2}{1+\nu}\right)\dfrac{\pi^2}{2}} & \text{for the torsional tube mode} \\ \lambda^{\text{f}} = \dfrac{a^2}{\ell_e^2}\sqrt{\left(1-\nu^2\right)\dfrac{\pi^4}{2}} & \text{for the flexural tube mode} \\ \lambda^{\text{o}}_{ij} = \dfrac{\sqrt{\left(1-\nu^2\right)\left(\frac{j\pi a}{\ell_e}\right)^4 + \frac{e^2}{12a^2}\left(i^2+\left(\frac{j\pi a}{\ell_e}\right)^2\right)^4}}{i^2+\left(\frac{j\pi a}{\ell_e}\right)^2} & \text{for the ovalization tube mode} \end{cases} \tag{60}$$

with $i = 6$ and $j = 1$ as i and j correspond to the number of circumferential and axial modes, respectively.

As a consequence, the maximum element eigenvalue is defined as:

$$\omega^n_{e,\max} = \max\left(\frac{2}{\ell_e}\sqrt{\frac{E}{\rho}},\ \frac{2}{\ell_e^2}\sqrt{\frac{EI_y}{\rho S}\pi^4},\ \frac{2\lambda_{\max}}{a}\sqrt{\frac{E}{\rho\left(1-\nu^2\right)}}\right) \tag{61}$$

where $\lambda_{\max} = \max\left(\lambda^{\mathrm{r}}, \lambda^{\mathrm{a}}, \lambda^{\mathrm{t}}, \lambda^{\mathrm{f}}, \lambda^{\mathrm{o}}_{ij}\right)$ given in Eq. (60) making it possible to express the stability condition used for the time step evaluation at each time iteration using Eq. (55).

4. Numerical results

The new tube finite-element proposed here and detailed in the previous sections is then assessed via comparisons with analytical or numerical reference solutions. For this purpose, several test-cases on a single straight pipe under various loading conditions are considered dealing with extension, breathing due to internal pressure, pure bending and punctual force on the tube cross-section. The pipe configuration used for all the considered tests is described in Table 1 and respects both the thin-shell and the Euler-Bernoulli hypotheses. In the following, in order to assess the

L (m)	a (m)	e (m)	E (GPa)	ν	ρ (kg/m^3)
10	1	0.1	200	0.3	7800

Table 1: Geometric and material properties of the pipe configuration used for the present tests.

grid-independence of the numerical solution, two computations are performed: the first one with a single tube element and the second one with ten tube elements. The verification of the present beam model is assessed on both static and dynamic problems. All the computations considered here are performed using a Courant number $C = 0.5$ in Eq. (55). For all considered test-cases, it appears that the critical time step is linked to the pipe cross-section ovalization (cf. Eq. (61)) leading to the following expression:

$$\Delta t = C\frac{a}{\lambda^{\mathrm{o}}_{ij}}\sqrt{\frac{\rho\left(1-\nu^2\right)}{E}} \tag{62}$$

with $\lambda^{\mathrm{o}}_{ij}$ the dimensionless ovalization frequency parameter expressed in Eq. (60). Finally, the following values of the time step are obtained: $\Delta t = 9.039 \times 10^{-5}$ s for one element and $\Delta t = 9.862 \times 10^{-6}$ s for ten elements. For the considered static problems, as an explicit time integration is used for solving the tube equations of motion, the imposed loading is not imposed suddenly but with a smooth increase in time in order to avoid spurious numerical oscillations. The associated rise time which is denoted here by τ is set to be significantly greater than the maximum time scale of each contribution of the tube element, i.e. beam axial, beam flexural, tube radial, tube torsional, tube flexural and tube ovalization, expressed in Sec. 3.5. In other words, τ is taken to be:

$$\tau = N\mathcal{T} \quad \text{with} \quad \mathcal{T} = \max\left(\ell_e\sqrt{\frac{\rho}{E}},\ \ell_e^2\sqrt{\frac{\rho S}{EI_y\pi^4}},\ \frac{a}{\lambda_{\min}}\sqrt{\frac{\rho\left(1-\nu^2\right)}{E}}\right) \tag{63}$$

where $\lambda_{\min} = \min\left(\lambda^{\mathrm{r}}, \lambda^{\mathrm{a}}, \lambda^{\mathrm{t}}, \lambda^{\mathrm{f}}, \lambda^{\mathrm{o}}_{ij}\right)$ given in Eq. (60) and $N >> 1$.

4.1. Test 1: Pipe contraction due to a uniform and static extension via the Poisson effect

The first test-case considered here consists in a simple extension. For this purpose, a symmetric displacement is imposed at the two boundaries of the tube, i.e. $\pm u_D/2$ at each side. Due to the Poisson effect which is taken into account in the present tube model, the pipe elongation is accompanied by a pipe cross-section reduction.

First, the analytical solution of the present test-case is derived from the proposed model considering only a uniform radial displacement which corresponds to the 0 mode in Fourier series as described in Sec. 2.4. In the present case of a

uniform extension, only the beam-type axial displacement U_o and the shell-type radial displacement w_o^c are non-zero. Considering a uniform radial displacement, the non-zero components of the strain tensor given in Eq. (11) and the non-zero generalized forces defined in Eq. (34) are expressed as:

$$\left\{\begin{array}{lcl} \varepsilon_{xx} & = & \dfrac{\partial U_o}{\partial x} \\ \varepsilon_{\theta\theta} & = & \left(\dfrac{1}{a} - \dfrac{z}{a^2}\right) w_o^c \end{array}\right. \quad \text{and} \quad \left\{\begin{array}{lcl} N & = & \dfrac{ES}{1-\nu^2}\left(\dfrac{\partial U_o}{\partial x} + \nu\dfrac{w_o^c}{a}\right) \\ (t_w)_o^c & = & \dfrac{ES}{1-\nu^2}\dfrac{1}{a}\left(\nu\dfrac{\partial U_o}{\partial x} + \dfrac{w_o^c}{a}\right) \end{array}\right. \tag{64}$$

Finally, the static equilibrium equations expressed in Eq. (33) write:

$$\frac{\partial N}{\partial x} = 0, \quad (t_w)_o^c = 0 \tag{65}$$

leading to the two following relations verified by the axial and the radial displacements:

$$w_o^c = -\nu a \frac{\partial U_o}{\partial x} \quad \text{and} \quad \frac{\partial^2 U_o}{\partial x^2} = 0 \tag{66}$$

Finally, using the value of the axial displacements at the two pipe boundaries, i.e. $U_o(0) = -\dfrac{u_D}{2}$ and $U_o(L) = \dfrac{u_D}{2}$, leads to:

$$U_o = \frac{u_D}{2L}(2x - L) \quad \text{and} \quad w_o^c = -\nu a \frac{u_D}{L} \tag{67}$$

In the present test-case, the elongation is taken as: $u_D/L = 0.01$ satisfying the small deformation assumption and leading to the following constant value: $w_o^c/a = -3 \times 10^{-3}$. Then, the numerical solutions are compared to the analytical solution previously described in order to assess the numerical method used for approximating the governing equations of the tube model.

The time evolution of the imposed displacement at the boundaries depicted in Fig. (6) starts with a smooth increase in order to avoid spurious numerical oscillations. The associated rise time is set to be equal to $\tau = 100\mathcal{T}$ in Eq. (63).

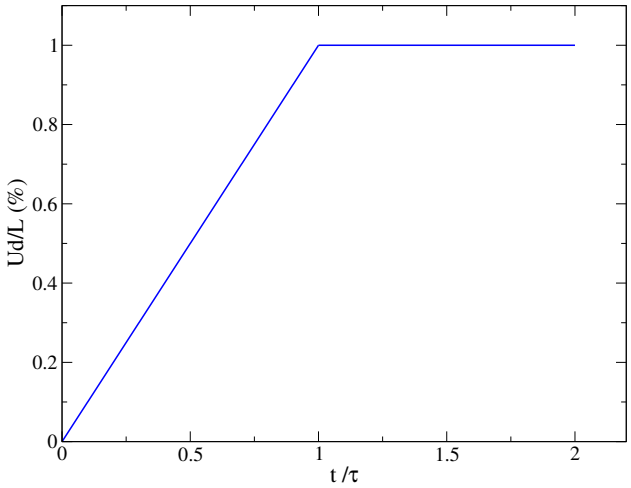

Figure 6: Test 1: Time evolution of the axial imposed normalized displacement.

The numerical solutions of the radial displacement obtained with one single element and ten elements are compared with the analytical solution in Fig. (7). It is shown that the steady-state solution is in good agreement with the analytical one as expected.

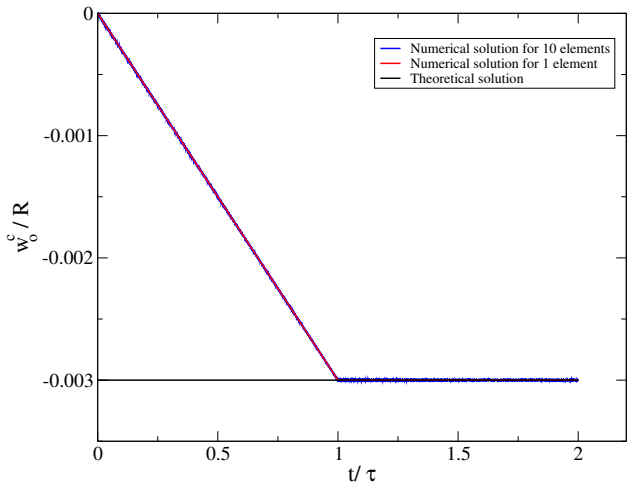

Figure 7: Test 1: Comparison between numerical and analytical solutions of the radial displacements for the elongation test.

4.2. Test 2: Radial pipe expansion due to an internal pressure

The second test-case consists in a tube under an internal pressure. A uniform pressure denoted by P_{int} is applied inside the pipe and creates a uniform expansion of the tube cross-section.

As in the previous case, the analytical solution of the present test is derived from the enriched beam model developed in this paper and considering only the mode 0 in the Fourier expansion. Once again, under an internal pressure loading, only the beam-type axial displacement U_o and the shell-type radial displacement w_o^c are non-zero. In addition, let us consider that w_o^c is uniform and that U_o is null. As a consequence, the only non-zero component of the strain tensor $\varepsilon_{\theta\theta}$ expressed in Eq. (11) and the generalized force associated with the radial pipe cross-section expansion $(t_w)_o^c$ given in Eq. (34) can be expressed as:

$$\varepsilon_{\theta\theta} = \left(\frac{1}{a} - \frac{z}{a^2}\right) w_o^c \quad \text{and} \quad (t_w)_o^c = \frac{ES}{1-\nu^2}\frac{1}{a^2} w_o^c \tag{68}$$

The power of the internal pressure applied to the inner tube surface writes as:

$$\mathcal{P}_e = \int_{A^-} P_{\text{int}} \delta w_o^c \mathrm{d}A^- = \int_0^L \int_0^{2\pi} P_{\text{int}} \delta w_o^c \left(a - \frac{e}{2}\right) \mathrm{d}\theta \mathrm{d}x = \int_0^L 2\pi P_{\text{int}} \left(a - \frac{e}{2}\right) \delta w_o^c \mathrm{d}x \tag{69}$$

Knowing the external loading, the equilibrium equation derived from Eq. (33) becomes:

$$(t_w)_o^c = 2\pi P_{\text{int}} \left(a - \frac{e}{2}\right) \tag{70}$$

As a consequence, the radial displacement due to the internal pressure can be expressed as:

$$w_o^c = \frac{P_{\text{int}}\left(1-\nu^2\right)}{E} \frac{a}{e} \left(a - \frac{e}{2}\right) \tag{71}$$

The numerical solutions are now compared with this analytical solution. In the present test-case, a uniform internal pressure P_{int} of 100 bar is imposed following a time evolution similar to the one depicted in Fig. (6) with a smooth linear increase in order to avoid spurious numerical oscillations where $\tau = 100\,\mathcal{T}$ as defined in Eq. (63). In addition, a condition of zero axial displacement, i.e. $U_o = 0$, is imposed at the two boundary nodes. For a pressure of 100 bar, the analytical solution expressed in Eq. 71 leads to the following value: $w_o^c = 4.3225 \times 10^{-4}$ m.

The comparison between the numerical solutions and the analytical radial displacement is shown in Fig. (8). The numerical results for one element is registered at the right boundary node and at the middle node for the computation with ten elements. As in the previous test-case, a good agreement between the numerical solutions and the analytical one is achieved.

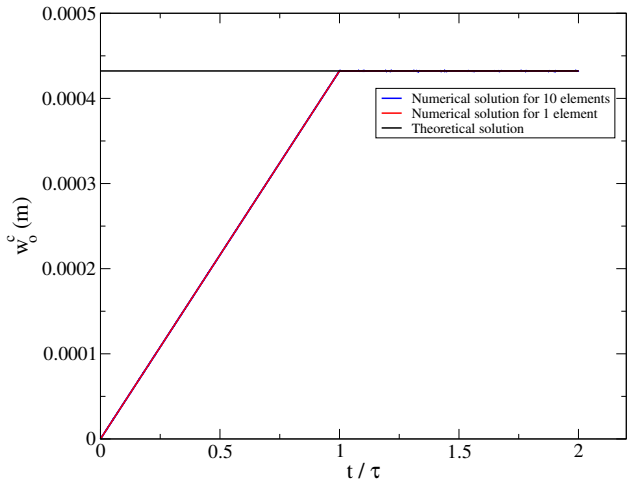

Figure 8: Test 2: Comparison between numerical and analytical solutions of the radial displacements for the breathing test - the analytical solution corresponds to the value: $w_o^c = 4.3225 \times 10^{-4}$ m.

4.3. Test 3: Dynamic radial tube motion

The present test-case is similar to the previous one except that a dynamic internal pressure loading is now considered. Following the same assumptions as previously, the equation of motion given in Eq. (32) writes as:

$$\rho S \frac{\partial^2 w_o^c}{\partial t^2} + (t_w)_o^c = 2\pi P_{\text{int}} \left(a - \frac{e}{2}\right) \quad \text{with} \quad (t_w)_o^c = \frac{ES}{1-\nu^2} \frac{1}{a^2} w_o^c \tag{72}$$

with the initial condition: $w_o^c(t = 0) = 0$ m. The analytical solution of this equation writes as:

$$w_o^c(t) = w_o^{c,\text{sta}} \Big(1 - \cos(\omega t)\Big) \quad \text{with} \quad w_o^{c,\text{sta}} = \frac{P_{\text{int}}\left(1-\nu^2\right)}{E} \frac{a}{e} \left(a - \frac{e}{2}\right) \quad \text{and} \quad \omega = \frac{1}{a} \sqrt{\frac{E}{\rho\left(1-\nu^2\right)}} \tag{73}$$

$w_o^{c,\text{sta}}$ corresponds to the static solution, i.e. the analytical solution of the previous test, and ω corresponds to the radial pulsation of a cylindrical shell as expressed in [43].

The computation of the present test-case is performed by imposing the internal pressure of 100 bar at the first time step. The corresponding numerical solutions obtained with both one element and ten elements shown in Fig. (9) correspond to a periodic function. The period obtained from the numerical solution is compared to its analytical counterpart: $T_{\text{the}} \approx 1.1836761 \times 10^{-3}$ s versus $T_{\text{num}} \approx 1.183688 \times 10^{-3}$ s, showing the good agreement between the two results.

In the two previous cases, only mode 0 in the Fourier expansion is considered which corresponds to the radial expansion/contraction of the tube cross-section. In the next test-case, only Fourier mode 2 is considering in order to represent the cross-section ovalization.

4.4. Test 4: Ovalization due to a pipe in-plane bending

The present test-case consists in a pure in-plane bending test where a symmetric rotation is imposed at the two boundaries of the tube, i.e. $\pm\Omega$ at each side. Due to the bending, it is expected that the tube tends to ovalize.

The analytical solution of the present test is derived from the present beam model considering only mode 2 in the Fourier series as it is detailed in Sec. 2.5. Considering in addition that w_2^c is uniform and that $w_2^c/a \ll 1$, the non-zero

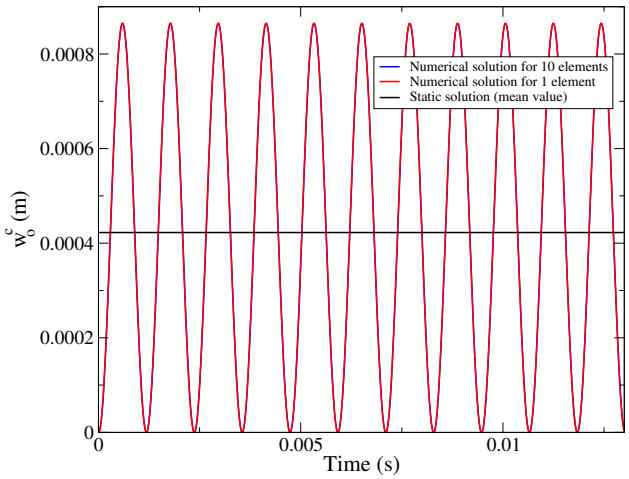

Figure 9: Test 3: Time evolution of the radial displacement in the case of an internal pressure loading.

forces defined in Eq. (41) can be expressed as:

$$\left\{ \begin{array}{lcl} M_y & = & -\dfrac{E}{1-\nu^2}\pi a^3 e \left(1 - \dfrac{3}{2}\dfrac{w_2^c}{a}\right)\dfrac{\partial^2 V_o}{\partial x^2} \\ (t_w)_2^c & = & +\dfrac{E}{1-\nu^2}\dfrac{3\pi a e}{4}\left(-a\left(\dfrac{\partial^2 V_o}{\partial x^2}\right)^2 + \dfrac{e^2}{a^2}\dfrac{w_2^c}{a^2}\right) \end{array} \right. \tag{74}$$

and the equilibrium equations given in Eq. (40) write:

$$\frac{\partial^2 M_y}{\partial x^2} = 0, \quad (t_w)_2^c = 0 \tag{75}$$

with the following boundary conditions:

$$\left\{ \begin{array}{l} V_o(0) = 0 \\ V_o(L) = 0 \end{array} \right. \quad \text{and} \quad \left\{ \begin{array}{l} -\Omega_y(0) = \dfrac{\partial V_o}{\partial x}(0) = -\Omega \\ -\Omega_y(L) = \dfrac{\partial V_o}{\partial x}(L) = \Omega \end{array} \right. \tag{76}$$

As a consequence, the beam-type vertical displacement V_o and the shell-displacement w_2^c are given by:

$$V_o = \Omega\frac{x}{L}(x - L) \quad \text{and} \quad w_2^c = 4\Omega^2 a\frac{a^4}{e^2 L^2} \tag{77}$$

In the present test-case, the rotation at the two pipe ends is taken as $\Omega = 0.1$ radian.

The numerical solutions are now compared to the analytical reference previously described. The time evolution of the imposed rotation at the two tube boundaries is once again similar as the one shown in Fig. (6). As previously, a smooth increase of the imposed rotation is considered in order to avoid spurious oscillations. In the present case, the rise time τ is taken as $\tau = 3000\,\mathcal{T}$ as defined in Eq. (63). In addition, the beam-type vertical displacement is set to be zero at the two pipe ends, i.e. $V_o(0) = 0$ and $V_o(L) = 0$.

The time evolution of the shell displacement corresponding to the second Fourier mode associated with the pipe cross-section ovalization is depicted in Fig. (10). The numerical results are taken at the outlet end of the tube for both one and ten elements. Once again, the analytical solution corresponds to the numerical steady-state solution. Note that, during the period $0 \leq t \leq \tau$ where the imposed rotation Ω evolves linearly in time, the radial displacement w_2^c follows a quadratic behavior. This is explained as w_2^c evolves with the square of Ω as shown in Eq. (77).

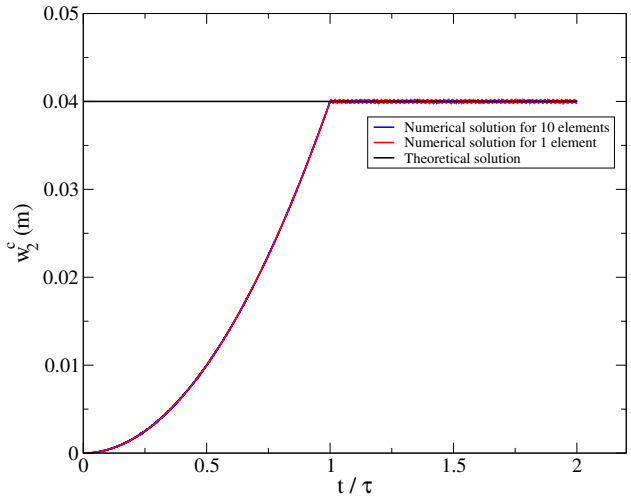

Figure 10: Test 4: Comparison between numerical and analytical solutions of the shell-type radial displacement corresponding to the second Fourier mode.

4.5. Test 5: Cross-section deformation of a clamped tube subject to a distributed patch load

This test-case consists in a tube clamped at its two ends and subjected to a downward distributed patch load of amplitude $F_z = 10^{10}$ N acting at the mid-region of its mid-surface within an area given by $0.4L \leq x \leq 0.6L$, $\pi/2 - \theta_p \leq \theta \leq \pi/2 + \theta_p$ at $z = 0$ with $\theta_p = \pi/100$ as depicted in Fig. (11). A reference numerical solution is first

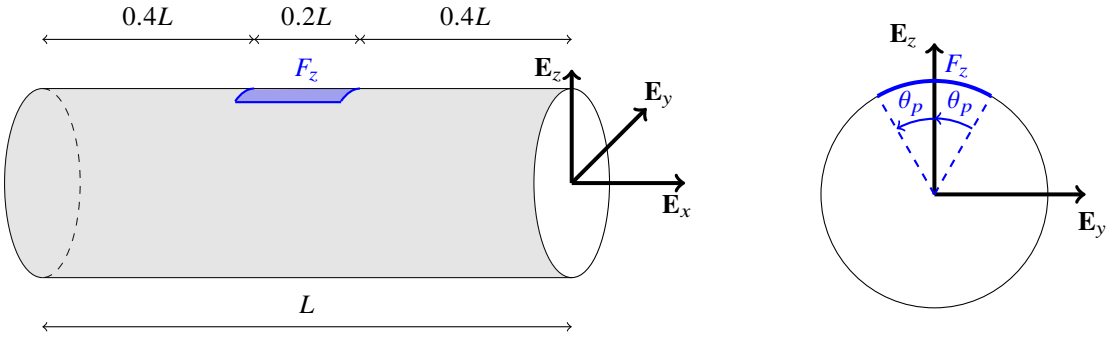

Figure 11: Test 5: Clamped tube subjected to a distributed patch load - patch loading area and direction of the vertical force.

obtained with shell elements in order to identify the tube cross-section deformation due to the present loading. For this purpose, this reference numerical solution is obtained using Code_Aster (`https://www.code-aster.org`) with the 9-node linear and bi-quadratic quadrilateral shell elements named Coque_3D [44]. The corresponding computation is performed with 9 082 elements, 32 068 nodes and 171 345 DOFs. Afterwards, the ability of the present tube model to retrieve the tube deformation is assessed. To this end, the distributed loading is applied with a smooth increase and $\tau = 100\mathcal{T}$ in Eq. (63) similarly as in Fig. (6). Due to the longitudinal variation of the distributed patch loading, 10 elements are used in the present computations, i.e. $\ell_e = L/10$. The external force is here applied to the present tube model through the virtual power principle where the power of this external force can be expressed as:

$$\mathcal{P}_e = -F_z \int_{0.4L}^{0.6L} \int_{\pi/2-\theta_p}^{\pi/2+\theta_p} \Big(\delta V_o + \sin\theta \; \delta w_o + \cos\theta \; \delta v_o \Big) \mathrm{d}\theta \mathrm{d}x$$

In practice, the external force is applied on the two tube elements located at the mid-length of the pipe, i.e. $0.4L \leq x \leq 0.5L$ for the first element and $0.5L \leq x \leq 0.6L$ for the second one. The different tests performed for the analysis of the present tube model on this test-case are described in the following.

4.5.1. *Influence of the number of Fourier modes*

First, the influence of the number of modes considered in the Fourier expansion in terms of the circumferential variable expressed in Eq. (15) is examined. For this purpose, the numerical solutions of the tube model using $N_f = 2$, $N_f = 4$ and $N_f = 6$ are compared to the reference shell-type solution. Fig. (12) shows the tube cross-section deformation at $x = 0.5L$ obtained with the different computations as well as the initial undeformed circular cross-

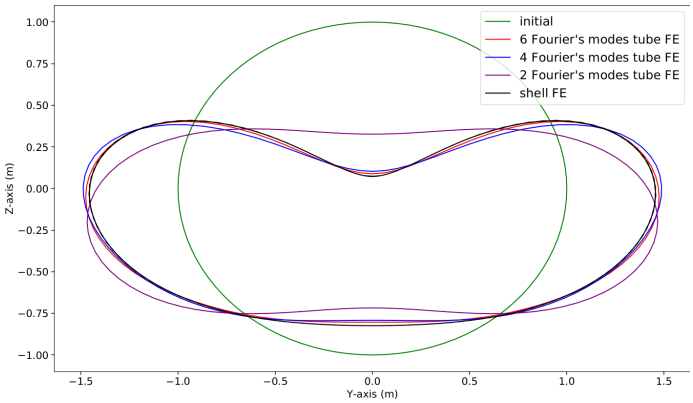

Figure 12: Test 5: Influence of the number of Fourier modes on the tube cross-section deformation at $x = 0.5L$.

section. The tube cross-section obtained with $N_f = 2$ has an elliptical shape with a slight asymmetry which is due to the inextensibility hypothesis as discussed in [34]. In contrast, the tube cross-section obtained with $N_f = 4$ and $N_f = 6$ is in good agreement with the reference shell solution with an improved concordance with $N_f = 6$. Note that this result is in accordance with the following references [6, 15, 45] where $N_f = 6$ is also retained by the authors. In the following, $N_f = 6$ is thus considered.

4.5.2. *Influence of the warping terms*

The influence of the consideration of the warping terms in the tube displacement field is now studied. The tube cross-sections at $x = 0.5L$ obtained with and without the warping terms are compared in Fig. (13). It is clearly shown

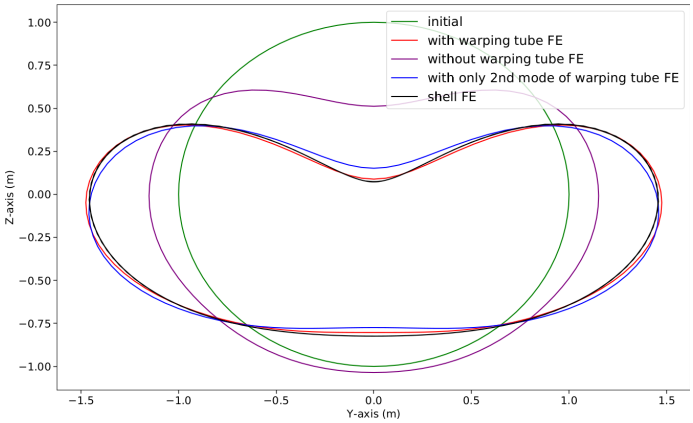

Figure 13: Test 5: Influence of the warping terms on the tube cross-section deformation at $x = 0.5L$.

that considering the warping terms is necessary to retrieve the reference deformation. This shows the interaction between warping and ovalization terms through the distortion $\varepsilon_{x\theta}$. Note that this coupling is also observed in the generalized forces as terms in $u_i^{c/s}$ are involved in the forces $(t_w)_i^{c/s}$ (see Eq. (B.13)). In addition, it has to be noticed

that the second Fourier mode for the warping terms u_o seems to be sufficient to be in agreement with the shell solution. However, in the following the warping terms are considered in conjunction with $N_f = 6$ for u_o, v_o and w_o.

4.5.3. *Influence of the non-linear coupling terms*

The influence of the consideration of the non-linear coupling terms in the tube kinematics is now analyzed. Fig. (14) shows the cross-section deformations at $x = 0.5L$ obtained with or without the non-linear terms. This demonstrates the requirement of considering the non-linear coupling to retrieve the reference shell deformation. To complete the analysis, the same comparison is now performed at different locations along the pipe, i.e. $x = 0.6L$, $x = 0.7L$, $x = 0.8L$ and $x = 0.9L$. In addition, the warping of the tube cross-section is also examined. Fig. (15) shows the corresponding results. At $x = 0.6L$, the highly deformed cross-section presents also a significant warping as well as a notable rotation which is not observed at $x = 0.5L$ due to the symmetry of the present problem. Once again, considering the non-linear coupling makes it possible to improve the agreement between the tube and the shell solutions. The more the sections are far from the pipe center the less is the corresponding deformation (ovalization and warping). In the same way, the influence of the non-linear coupling is reduced as the section moves away. In all the observed locations, the solutions considering the non-linear coupling is in good agreement with the reference solution.

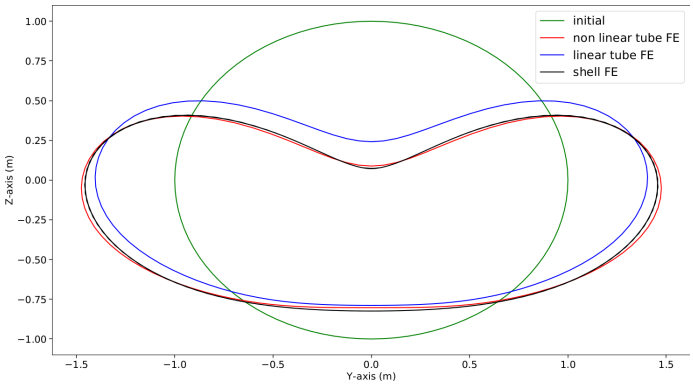

Figure 14: Test 6: Influence of the non-linear coupling terms on the tube cross-section deformation at $x = 0.5L$.

The previous analysis is performed on the tube cross-section deformation including both ovalization and warping. Focus is now given to the local generalized stress field for both linear and non-linear tube models. This is performed through the comparison with the numerical solutions obtained with shell finite-elements.

4.5.4. *Analysis of the longitudinal stress component and comparison with shell elements*

Comparison with shell-type solution is now performed on the longitudinal stress component σ_{xx} given by:

$$\sigma_{xx} = \sigma^m_{xx} + z\sigma^k_{xx} \quad \text{with} \quad \sigma^m_{xx} = \frac{E}{1-\nu^2}\left(\varepsilon^m_{xx} - \nu\,\varepsilon^m_{\theta\theta}\right) \quad \text{and} \quad \sigma^k_{xx} = \frac{E}{1-\nu^2}\left(k_{xx} - \nu k_{\theta\theta}\right)$$

The profile of this contribution along the circumferential direction at $x = 0.5L$ is depicted in Fig. (16) for the shell-type modeling, the non-linear and the linear tube model in conjunction with six Fourier modes at $z = 0$, i.e. at the mid-surface, for the membrane term and at $z = e/2$ which corresponds to the outer surface. Concerning the membrane term σ^m_{xx}, it has to be noticed that the three models lead to a similar oscillatory response with a first peak associated with a compressive stress at $\theta = \pi/2$ which corresponds to the location of the external load center and a second *compressive stress* peak at $\theta = 3\pi/2$. In addition, two peaks associated with a tensile stress are also obtained but their locations differ from one model to the other. With the shell model, these two peaks are located at $\theta = \pi$ and $\theta = 2\pi$. However, with the present tube model (for both linear and non-linear formulations), the analysis of the strain tensor components shows that these *tensile stress* peaks are located at the locations of the two local extrema of the ε^m_{xx} component. Due to the inextensibility assumption for Fourier modes of order greater than or equal to two considered

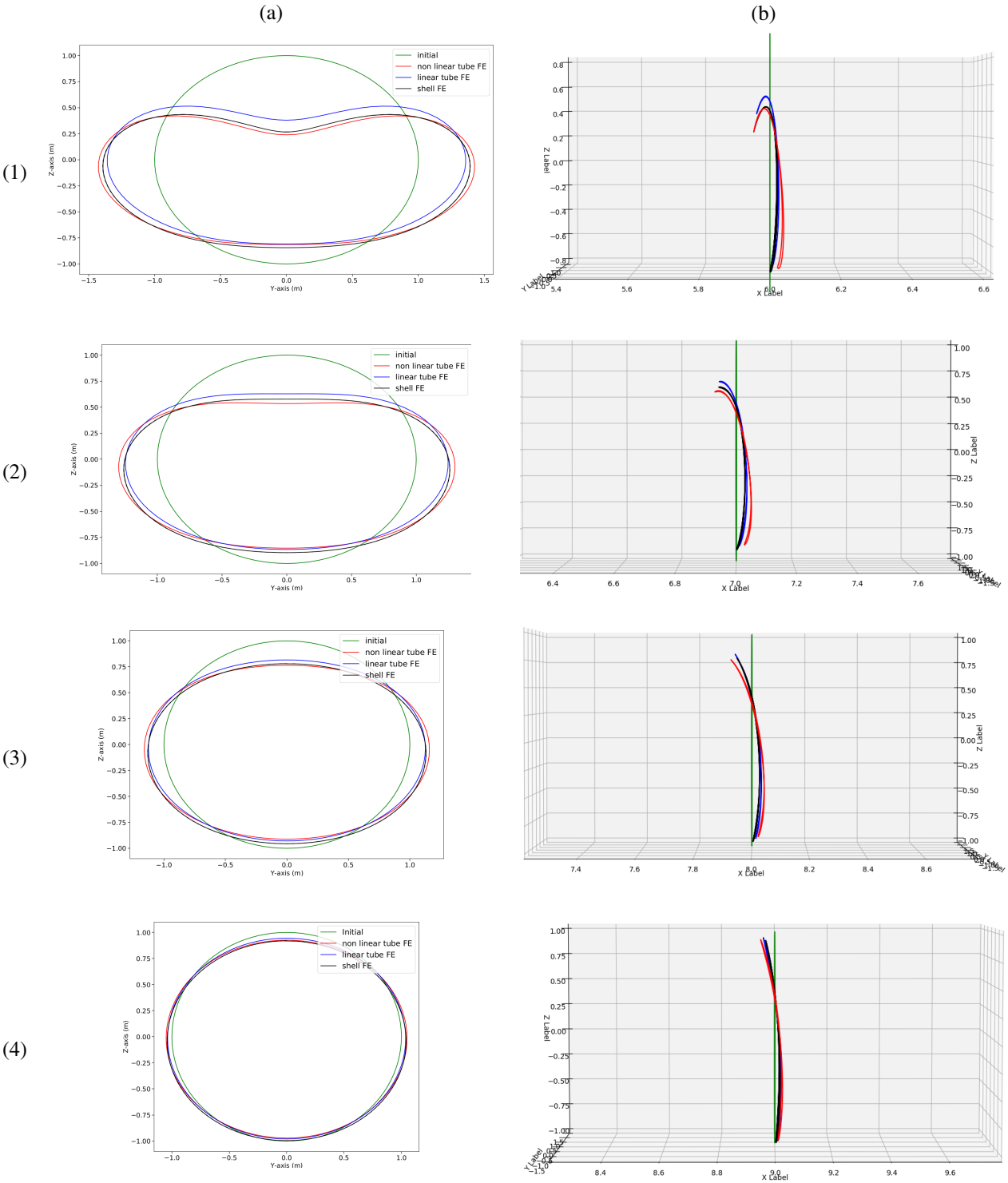

Figure 15: Test 5: Influence of the non-linear coupling on the tube cross-section (a) ovalization and (b) warping at different locations along the pipe: (1) at $x = 0.6L$, (2) at $x = 0.7L$, (3) at $x = 0.8L$ and (4) at $x = 0.9L$.

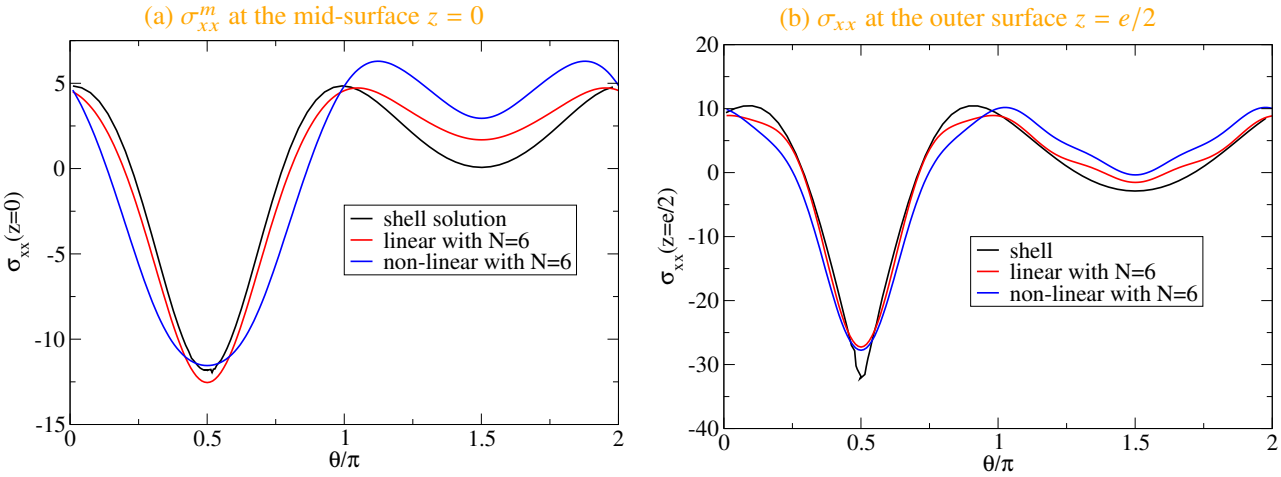

Figure 16: Test 5: Longitudinal stress component σ_{xx} at $x = 0.5L$ (a) for $z = 0$ and (b) for $z = e/2$, comparison between shell elements, non-linear and linear tube model with 6 Fourier modes, the stress values are divided by 10^9 Pa.

in the present formulation, only the first Fourier mode is involved in $\varepsilon^m_{\theta\theta}$ which, finally, has no influence on these two *tensile stress* peaks. Nevertheless, a quite good agreement is obtained with the three models. This agreement seems to be furthermore improved for the σ_{xx} component at the outer surface. Once again, two *compressive stress* peaks and two *tensile stress* peaks are observed in the shell solution which are retrieved with the present tube model with both linear and non-linear formulations.

The previous analysis demonstrates the accuracy of the present tube model in comparison with a shell solution. The two types of numerical solution are now compared in terms of computational efficiency.

4.5.5. Further discussion on the computational efficiency of the present tube model

In order to estimate the computational savings providing by the use of the present tube model with respect to the use of shell elements, focus is here firstly given to the number of DOFs involved in the two types of model considered here. Classically when using quadrangle shell elements, it corresponds to 4-node elements with 6 DOFs per node (3 translations and 3 rotations). Let us denote by $\mathcal{N}$ the number of shell elements used to discretize the pipe circumference. A lower estimation of $\mathcal{N}$ is 16 where only 4 nodes are used for the discretization of a quarter of the pipe circumference which corresponds to a quite coarse description of the pipe perimeter. Using only one shell in the pipe longitudinal direction leads to 192 DOFs. In contrast, when using one single tube element, only 2 nodes are considered with 42 DOFs per nodes (or 22 DOFs for an in-plane motion), i.e. 84 DOFs (or 44 DOFs for an in-plane motion). As a consequence, with similar length and stability condition, the use of the present tube model makes it possible to reduce the computational effort by a factor of 2.28 (or 4.56 for an in-plane motion). Obviously, the computational savings are increased when the pipe circumference is more accurately discretized. For example, in the present test-case, $\mathcal{N} = 64$ nodes are used for the pipe perimeter leading to a ratio of 9.14 (or 17.45 for an in-plane motion) between the DOFs with shell elements and the DOFs with one single tube element showing the significant reduction of the number of DOFs. Then, another aspect which has to be considered for the evaluation of computational efficiency of the present tube model in comparison with standard shell elements is the time for constructing generalized forces. For this purpose, the size and sparseness of the stiffness matrices when using the tube element and the standard 4-node shell finite element are here studied and detailed in Appendix C. It is shown that the stiffness matrix of the present tube element has 1948 non-zero components using the non-linear formulation and 476 non-zero components when it is derived following the linear formulation for one single element. In comparison, the shell stiffness matrix has 208 non-zero components for one single element showing a ratio of 9.36 for the non-linear tube and a ratio of 2.29 for the linear tube. As it is discussed previously $\mathcal{N} = 16$ shell elements represent a coarse description of the pipe perimeter. However, it leads to a greater time for constructing the stiffness matrix when using shell elements in comparison

with only one single tube element for the same section. Finally, focus is now given to the comparison between the critical time step obtained with the present tube model and the one obtained with shell elements as it directly drives the computational cost for dynamic analysis. In the present case, as discussed previously, the critical time step is given by the cross-section ovalization (cf. Eq. (62)) leading to the following value: $\Delta t_{\text{tube}} \approx 9.862 \times 10^{-6}$ s for $\ell_e = L/10$ (corresponding to 10 elements in the pipe length). For shell elements, the critical time step should be rigorously given by the most restrictive mode among traction, bending and torsion which is in general due to the rotational DOFs. In explicit dynamics, the rotary mass can be scaled to permit larger time steps without a loss of stability [46, 41]. As a consequence, the critical time step is given by the traction mode with the following expression:

$$\Delta t_{\text{shell}} = C\ell_e \sqrt{\frac{\rho\left(1-\nu^2\right)}{E}} \tag{78}$$

leading to the value: $\Delta t_{\text{tube}} \approx 9.25 \times 10^{-6}$ s for $\ell_e = 2\pi a/64$ (corresponding to 64 elements in the pipe perimeter) with a Courant number $C = 0.5$. This leads to a similar value for the critical time step between the proposed tube element and shell elements. This analysis clearly demonstrates the interest of the present tube model in terms of computational efficiency. In addition, it has to be noticed that for FSI problems, the present tube model has to be coupled with a 1-D fluid model for the internal fluid. In that case, only one 1-D fluid cell is required in conjunction with the present tube model as described in [39]. In contrast, it is necessary to mesh the 3-D internal fluid domain inside the tube when it is discretized with shell elements. Once again it strongly increases the computational effort associated with the use of shell elements in contrast to the one of the present tube model. What is more, it also makes it possible to avoid the numerical problems due to the rezoning procedure with large pipe cross-section deformations where robustness problems can appear due to the apparition of high distortions of meshes in the fluid domain. This is an additional major interest of using the present tube model.

5. Conclusion and perspectives

A novel straight thin-walled tube element has been here proposed in order to take deformations of its cross-section and inertia evolution into account. The present kinematics is decomposed into Euler-Bernoulli beam, Love-Kirchhoff shell contributions and a non-linear coupling between cross-section deformation and neutral axis rotation. Concerning the shell kinematics, the Flügge thin cylindrical shell theory is used. Finally, Fourier expansion in terms of the circumferential variable is applied for the mid-surface DOFs in which coefficients producing a rigid-body motion are excluded to avoid redundancy with beam DOFs. In addition, for Fourier modes of order greater than or equal to two, an inextensiblity of the section is assumed. Following this derivation, the proposed tube element DOFs depend only on the longitudinal variable while also considering radial expansion, warping as well as ovalization of its cross-section. In addition, the consideration of the non-linear coupling terms ensures that the inertia of the tube section can evolve with its deformation. A comparison between the proposed formulation and the previously published ones is discussed showing that the present formulation consider complete Fourier expansion for all the shell DOFs which thus can be seen as a generalization of the previous approaches. In addition, the present formulation seems to be the simplest one able to consider the cross-section deformations as well as the changes of inertia as only one non-linear coupling term is taken into account for this purpose. Note that this non-linear term is not sufficient to describe all possible local and global buckling. Then, the tube equations of motion are obtained and expressed through the virtual power principle. Afterwards, an explicit updated Lagrangian Finite-Element solver is proposed for the present tube model. In particular, the lumped mass matrix is described as well as the stability condition of the explicit scheme taking into account both beam and shell contributions. Then, the proposed tube model is assessed on several test-cases. A first series of simple cases where analytical solutions of the tube model can be obtained is considered in order to evaluate the numerical method. Finally, a more complex test-case involving a distributed patch loading is studied. The numerical solution of the present tube model is here compared with a reference solution obtained with shell elements. The influence of the Fourier modes number as well as the warping terms and the non-linear coupling is examined. The shell-type cross-section deformation is retrieved with the present tube model. Finally, a discussion concerning the computational efficiency of the proposed element is also provided in order to illustrate the corresponding savings in comparison with the use of shell elements.

The present tube element has been proposed and derived in the context of straight thin-walled tubular geometries. However, realistic piping systems involve elbows and bends. For this reason, the present model has first to be extended to curved thin-walled tubes via the introduction of the elbow's radius of curvature and the associated local frame of reference where the tube displacement field has to be expressed. In addition, only a linear elastic behavior is considered in the present study. Plasticity has thus to be taken into account in the future in order to perform inelastic analysis of piping systems where additional questions arise. In particular, a yield criterion taking into account all of the generalized forces of the tube element has to be defined. In addition, focus has also to be given to the local detection of the tube region where plasticity occurs. Finally, for considering FSI problems, the present tube model has also to be coupled with a 1-D fluid model in a similar way as it is proposed in [39] where a standard Euler-Bernoulli beam element is used. In this kind of coupling, the cross-section deformation has a direct impact on the wave speed of the internal fluid pressure waves whereas the internal fluid pressure variation has an influence on the tube section evolution. These different issues are under consideration for current research in order to use the present tube element for the simulation of fast-transient events occurring in industrial piping systems such as pipe whipping for example.

Acknowledgements

The first author received a financial support through the EDF-CIFRE contract 2019/0907. This work has been achieved within the framework of the "Dynamique Rapide" project of the EDF/CEA/Framatome tripartite Institute. Computational facilities were provided by EDF. Numerical simulations have been performed with the *Europlexus* software.

[1] M. P. Païdoussis, Fluid-Structure Interactions, Slender structures and axial flow, Volume 2, Elsevier Academic Press, 2003.
[2] M. P. Païdoussis, Fluid-Structure Interactions, Slender structures and axial flow, Volume 1, 2nd edition, Elsevier Academic Press, 2014.
[3] A. S. Tijsseling, Fluid-structure interaction in liquid-filled pipe systems: A review, J. Fluids Struct. 10 (1996) 395–420.
[4] S. Li, B. W. Karney, G. Liu, FSI research in pipeline systems A review of the literature, J. Fluids Struct. 57 (2015) 277–297.
[5] T. von Kármán, Uber die Formänderung dünnwandiger Rohre, insbseondere federnder Ausgleichsrohre, Z. Ver. deut. Ing. 55 (1911) 1889–1895, (in German).
[6] H. Ohtsubo, O. Watanabe, Stress analysis of pipe bends by ring elements, ASME J. Pressure Vessel Technol. 100 (1) (1978) 122–122.
[7] K.-J. Bathe, C. A. Almeida, A simple and effective pipe elbow element, linear analysis, ASME J. Appl. Mech. 47 (1980) 93–100.
[8] A. Millard, R. Roche, Elementary solutions for the propagation of ovalization along straight pipes and elbows, Int. J. Pres. Ves. & Piping 16 (1) (1984) 101–129.
[9] C. Militello, A. E. Huespe, A displacement-based pipe elbow element, Comput. Struct. 29 (2) (1988) 339–343.
[10] M. Abo-Elkhier, Analysis of pipe bends using pipe elbow element, Comput. Struct. 37 (1) (1990) 9–15.
[11] M.-N. Berton, A simplified method for elastic calculation for pipes based on the beam theory and allowing for section ovalization, Int. J. Pres. Ves. & Piping 51 (1) (1992) 53–83.
[12] S. A. Karamanos, J. L. Tassoulas, Tubular members I: stability analysis and preliminary results, ASCE J. Eng. Mech. 122 (1) (1996) 64–71.
[13] E. M. M. Fonseca, F. J. M. Q. de Melo, C. A. M. Oliveira, Determination of flexibility factors in curved pipes with end restraints using a semi-analytical formulation, Int. J. Pres. Ves. & Piping 79 (12) (2002) 829–840.
[14] K. Weicker, R. Salahifar, M. Mohareb, Shell analysis of thin walled pipes. Part I - Field equations and solution, Int. J. Pres. Ves. & Piping 87 (2010) 402–413.
[15] K. Weicker, R. Salahifar, M. Mohareb, Shell analysis of thin walled pipes. Part II - Finite element formulation, Int. J. Pres. Ves. & Piping 87 (2010) 414–423.
[16] S. Attia, M. Mohareb, M. Martens, N. Y. Ghodsi, Y. Li, S. Adeeb, Shell finite element formulation for geometrically nonlinear analysis of straight thin-walled pipes, Int. J. Nonlinear Mech. 137 (2021) 103829.
[17] S. Attia, M. Mohareb, M. Martens, N. Y. Ghodsi, Y. Li, S. Adeeb, Shell finite element formulation for geometrically nonlinear analysis of curved thin-walled pipes, Thin-Walled Struct. 173 (2022) 108971.
[18] K.-J. Bathe, C. A. Almeida, A simple and effective pipe elbow element, interaction effects, ASME J. Appl. Mech. 49 (1982) 165–171.
[19] K.-J. Bathe, C. A. Almeida, A simple and effective pipe elbow element, pressure stiffening effects, ASME J. Appl. Mech. 49 (1982) 914–915.
[20] E. Ruocco, J. N. Reddy, A new nonlinear 5-parameter beam model accounting for the Poisson effect, Int. J. Nonlinear Mech. 142 (2022) 103996.
[21] M. Chadha, M. D. Todd, The mathematical theory of a higher-order geometrically-exact beam with a deforming cross-section, Int. J. Solids Struct. 202 (2020) 854–880.
[22] I. Sokolov, S. Krylov, I. Harari, Extension of non-linear beam models with deformable cross sections, Comput. Mech. 56 (2015) 999–1021.
[23] R. F. Vieira, F. B. E. Virtuoso, E. B. R. Pereira, Buckling of thin-walled structures through a higher order beam model, Comput. Struct. 180 (2017) 104–116.
[24] L. Duan, J. Zhao, A geometrically exact cross-section deformable thin-walled beam finite element based on generalized beam theory, Comput. Struct. 218 (2019) 32–59.
[25] J. N. Reddy, Theories and analyses of beams and axisymmetric circular plates, CRC Press, 2022.
[26] Y. Pascal Abdellaoui, Modèles mécaniques de poutre enrichis pour la simulation de tubes minces sous pression, Ph.D. thesis, Université Paris-Saclay (2022).

[27] M. Amabili, Nonlinear Vibrations and Stability of Shells and Plates, Cambridge University Press, New York, USA, 2008.
[28] A. W. Leissa, Vibration of shells, Tech. Rep. NASA SP-288, NASA (1973).
[29] W. Flügge, Stresses in Shells, Springer Berlin Heidelberg, Germany, 1973.
[30] S. Timoshenko, Theory Of Plates And Shells, McGraw Hill, New-York, USA, 1959.
[31] J. D. Wood, The flexure of a uniformly pressurized, circular, cylindrical shell, ASME J. Appl. Mech. 25 (4) (1958) 453–458.
[32] L. Madureira, F. Q. Melo, Stress analysis of curved pipes with a hybrid formulation, Int. J. Pres. Ves. & Piping 81 (3) (2004) 243–249.
[33] L. G. Brazier, On the flexure of thin cylindrical shells and other "thin" sections, Proc. Royal Society London, Series 116 (773) (1927) 104–114.
[34] S. A. Karamanos, Bending instabilities of elastic tubes, Int. J. Solids Struct. 39 (2002) 2059–2085.
[35] F. Daude, P. Galon, A. Shams, Numerical investigations of a two-way coupled fluid-structure interaction approach for fast transients in fluid-filled flexible piping systems, In preparation.
[36] H. Cao, M. Mohareb, I. Nistor, Finite element for the dynamic analysis of pipes subjected to water hammer, J. Fluids Struct. 93 (2020) 102845.
[37] J. S. Walker, J. W. Phillips, Pulse propagation in fluid-filled tubes, ASME J. Appl. Mech. 44 (1977) 31–35.
[38] P. Galon, M. Lepareux, Documentation théorique : Modélisation des tuyauteries dans *Europlexus*, Tech. Rep. DEN/DM2S/SEMT/DYN/RT/01-021/A, CEA (2001).
[39] F. Daude, P. Galon, A Finite-Volume approach for compressible single- and two-phase flows in flexible pipelines with fluid-structure interaction, J. Comput. Phys. 362 (C) (2018) 375–408.
[40] S. W. Key, Transient response by time integrations: review of implicit and explicit operators, in: J. Donea (Ed.), Advanced Structural Dynamics, Applied Science Publishers, UK, 1980, pp. 71–95.
[41] T. J. R. Hughes, The Finite Element Method - Linear Static and Dynamic Finite Element Analysis, Dover Publications, Inc., 2000.
[42] T. Belytschko, W. K. Liu, B. Moran, K. I. Elkhodary, Nonlinear Finite Elements for Continua and Structures, 2d edition, Wiley, 2014.
[43] R. D. Blevins, Formulas For Dynamics, Acoustics And Vibration, Wiley, 2016.
[44] T. De Soza, Modélisation Coque_3D, documentation Code_Aster (2015).
[45] H. D. Hibbit, E. K. Leung, An approach to detailed inelastic analysis of thin walled pipelines, in: T. J. R. Hughes, A. Pifko, A. Jay (Eds.), Nonlinear Finite Element Analysis of Plates and Shells, ASME, AMD 48, 1981, pp. 83–118.
[46] T. J. R. Hughes, M. Cohen, M. Haroun, Reduced and selective integration techniques in the Finite Element analysis of plates, Nuclear Eng. Design 46 (1978) 203–222.
[47] J.-S. Chang, W.-J. Chiou, Natural frequencies and critical velocities of fixed-fixed laminated circular cylindrical shells conveying fluids, Comput. Struct. 57 (5) (1995) 929–939.
[48] M. Ji, K. Inaba, F. Triawan, Vibration characteristics of cylindrical shells filled with fluid based on first-order shell theory, J. Fluids Struct. 85 (2019) 275–291.

Appendix A. Derivatives with respect to coordinates x, θ and z

As given in Eq. (1), the coordinates of the point $\mathbf{m}$ in the deformed configuration following an in-plane motion in the $(\mathbf{E}_x, \mathbf{E}_z)$ plane, i.e. $W_o = 0$ and $\Omega_x = \Omega_z = 0$, are expressed as:

$$\begin{aligned}\mathbf{m} \quad = \quad & \left(x + U_o + u + \left[(a + z + w)\sin\theta + v\cos\theta\right]\Omega_y\right)\mathbf{E}_x + \left(V_o\sin\theta + a + z + w - u\Omega_y\sin\theta\right)\mathbf{E}_R + \\ & \left(V_o\cos\theta + v - u\Omega_y\cos\theta\right)\mathbf{E}_\theta\end{aligned}$$

The coupling terms involving the tube axis rotation and the warping degree-of-freedom, i.e. $u\Omega_y$, are here neglected leading to:

$$\mathbf{m} = \left(x + U_o + (a + z)\,\Omega_y\sin\theta + u + \Omega_y h\right)\mathbf{E}_x + (V_o\sin\theta + a + z + w)\,\mathbf{E}_R + (V_o\cos\theta + v)\,\mathbf{E}_\theta$$

with $h = (w\mathbf{E}_R + v\mathbf{E}_\theta)\cdot\mathbf{E}_z = w\sin\theta + v\cos\theta$. The derivatives of the coordinates of the point $\mathbf{m}$ with respect to the variables x, θ and z are given by:

$$\begin{cases}\partial_x\mathbf{m} \quad = \quad \left(1 + \dfrac{\partial U_o}{\partial x} + \dfrac{\partial u}{\partial x} + (a + z)\dfrac{\partial\Omega_y}{\partial x}\sin\theta + \dfrac{\partial}{\partial x}\left(\Omega_y h\right)\right)\mathbf{E}_x + \left(\dfrac{\partial V_o}{\partial x}\sin\theta + \dfrac{\partial w}{\partial x}\right)\mathbf{E}_R + \left(\dfrac{\partial V_o}{\partial x}\cos\theta + \dfrac{\partial v}{\partial x}\right)\mathbf{E}_\theta \\ \partial_z\mathbf{m} \quad = \quad \left(\dfrac{\partial u}{\partial z} + \Omega_y\sin\theta + \Omega_y\dfrac{\partial h}{\partial z}\right)\mathbf{E}_x + \left(1 + \dfrac{\partial w}{\partial z}\right)\mathbf{E}_R + \dfrac{\partial v}{\partial z}\mathbf{E}_\theta \\ \partial_\theta\mathbf{m} \quad = \quad \left(\dfrac{\partial u}{\partial\theta} + (a + z)\,\Omega_y\cos\theta + \Omega_y\dfrac{\partial h}{\partial\theta}\right)\mathbf{E}_x + \left(\dfrac{\partial w}{\partial\theta} - v\right)\mathbf{E}_R + \left(\dfrac{\partial v}{\partial\theta} + a + z + w\right)\mathbf{E}_\theta\end{cases}$$

The metrics associated with this gradient are defined as:

$$g_{ij} \equiv \partial_i\mathbf{m}\cdot\partial_j\mathbf{m}$$

with $i = x, \theta, z$ and $j = x, \theta, z$. Then, neglecting both the second-order beam-type displacement terms and the second-order shell-type displacement terms leads to the following metrics expressions:

$$\begin{cases} g_{xx} = 1 + 2\left(\dfrac{\partial U_o}{\partial x} + \dfrac{\partial u}{\partial x} + (a+z)\dfrac{\partial \Omega_y}{\partial x}\sin\theta\right) + 2\left(\Omega_y + \dfrac{\partial V_o}{\partial x}\right)\dfrac{\partial h}{\partial x} + 2h\dfrac{\partial \Omega_y}{\partial x} \\ g_{\theta\theta} = (a+z)^2 + 2(a+z)\left(\dfrac{\partial v}{\partial \theta} + w\right) \\ g_{zz} = 1 + 2\dfrac{\partial w}{\partial z} \\ g_{x\theta} = \dfrac{\partial u}{\partial \theta} + (a+z)\left(\Omega_y + \dfrac{\partial V_o}{\partial x}\right)\cos\theta + \left(\Omega_y + \dfrac{\partial V_o}{\partial x}\right)\dfrac{\partial h}{\partial \theta} + (a+z)\dfrac{\partial v}{\partial x} \\ g_{xz} = \dfrac{\partial u}{\partial z} + \left(\Omega_y + \dfrac{\partial V_o}{\partial x}\right)\sin\theta + \left(\Omega_y + \dfrac{\partial V_o}{\partial x}\right)\dfrac{\partial h}{\partial z} + \dfrac{\partial w}{\partial x} \\ g_{z\theta} = \dfrac{\partial w}{\partial \theta} - v + (a+z)\dfrac{\partial v}{\partial z} \end{cases}$$

The strain tensor is directly obtained with the metrics using the relations:

$$\begin{cases} 2\,\varepsilon_{xx} = g_{xx} - 1 \\ 2\,\varepsilon_{\theta\theta} = \dfrac{1}{(a+z)^2} g_{\theta\theta} - 1 \\ 2\,\varepsilon_{zz} = g_{zz} - 1 \end{cases} \quad \text{and} \quad \begin{cases} 2\,\varepsilon_{x\theta} = \dfrac{1}{a+z} g_{x\theta} \\ 2\,\varepsilon_{xz} = g_{xz} \\ 2\,\varepsilon_{z\theta} = \dfrac{1}{a+z} g_{z\theta} \end{cases}$$

As a consequence, the strain-displacement relations are given by:

$$\begin{cases} \varepsilon_{xx} = \dfrac{\partial U_o}{\partial x} + (a+z)\sin\theta\dfrac{\partial \Omega_y}{\partial x} + \dfrac{\partial u}{\partial x} + \left(\Omega_y + \dfrac{\partial V_o}{\partial x}\right)\dfrac{\partial h}{\partial x} + h\dfrac{\partial \Omega_y}{\partial x} \\ \varepsilon_{\theta\theta} = \dfrac{1}{a+z}\left(\dfrac{\partial v}{\partial \theta} + w\right) \\ \varepsilon_{zz} = \dfrac{\partial w}{\partial z} \\ 2\,\varepsilon_{x\theta} = \left(\Omega_y + \dfrac{\partial V_o}{\partial x}\right)\cos\theta + \dfrac{1}{a+z}\dfrac{\partial u}{\partial \theta} + \dfrac{\partial v}{\partial x} + \dfrac{1}{a+z}\left(\Omega_y + \dfrac{\partial V_o}{\partial x}\right)\dfrac{\partial h}{\partial \theta} \\ 2\,\varepsilon_{xz} = \left(\Omega_y + \dfrac{\partial V_o}{\partial x}\right)\sin\theta + \dfrac{\partial u}{\partial z} + \dfrac{\partial w}{\partial x} + \left(\Omega_y + \dfrac{\partial V_o}{\partial x}\right)\dfrac{\partial h}{\partial z} \\ 2\,\varepsilon_{z\theta} = \dfrac{1}{a+z}\left(\dfrac{\partial w}{\partial \theta} - v\right) + \dfrac{\partial v}{\partial z} \end{cases} \tag{A.1}$$

Appendix B. Virtual power principle

The virtual power principle writes:

$$\mathcal{P}_a = \mathcal{P}_i + \mathcal{P}_e \quad \text{with} \quad \mathcal{P}_a = \int_\Omega \rho \frac{\partial^2 \mathbf{U}}{\partial t^2} \cdot \delta\,\mathbf{U}\,\mathrm{d}V \quad \text{and} \quad \mathcal{P}_i = -\int_\Omega \boldsymbol{\sigma} : \delta\,\boldsymbol{\varepsilon}\,\mathrm{d}V \tag{B.1}$$

with the elementary volume $\mathrm{d}V = a\,\mathrm{d}\theta\mathrm{d}z\mathrm{d}x$ and the elementary surface $\mathrm{d}S = a\,\mathrm{d}\theta\mathrm{d}z$.

Appendix B.1. Power of inertia

Based on the displacement field expressed in Eq. (16), the acceleration and virtual displacement vectors are given by:

$$\begin{cases} \dfrac{\partial^2 \mathbf{U}}{\partial t^2} &= \left(\dfrac{\partial^2 U_o}{\partial t^2} + \dfrac{\partial^2 u}{\partial t^2} + [(a+z)\sin\theta + h]\dfrac{\partial^2 \Omega_y}{\partial t^2} + 2\dfrac{\partial h}{\partial \mathrm{t}}\dfrac{\partial \Omega_y}{\partial \mathrm{t}} + \Omega_y \dfrac{\partial^2 h}{\partial t^2}\right)\mathbf{E}_x + \left(\dfrac{\partial^2 V_o}{\partial t^2}\sin\theta + \dfrac{\partial^2 w}{\partial t^2}\right)\mathbf{E}_R + \left(\dfrac{\partial^2 V_o}{\partial t^2}\cos\theta + \dfrac{\partial^2 v}{\partial t^2}\right) \\ \delta\mathbf{U} &= \left(\delta U_o + \delta u + [(a+z)\sin\theta + h]\,\delta\Omega_y + \Omega_y \delta h\right)\mathbf{E}_x + (\delta V_o \sin\theta + \delta w)\,\mathbf{E}_R + (\delta V_o \cos\theta + \delta v)\,\mathbf{E}_\theta \end{cases}$$

leading to the following scalar product:

$$\begin{aligned} \frac{\partial^2 \mathbf{U}}{\partial t^2}\cdot\delta\mathbf{U} &= \frac{\partial^2 U_o}{\partial t^2}\delta U_o + \frac{\partial^2 u}{\partial t^2}\delta u + [(a+z)\sin\theta + h]^2\frac{\partial^2 \Omega_y}{\partial t^2}\delta\Omega_y + \\ &\quad \frac{\partial^2 V_o}{\partial t^2}\delta V_o + \frac{\partial^2 V_o}{\partial t^2}\delta h + \frac{\partial^2 h}{\partial t^2}\delta V_o + \frac{\partial^2 v}{\partial t^2}\delta v + \frac{\partial^2 w}{\partial t^2}\delta w \end{aligned}$$

Using the Euler-Bernoulli condition (cf. Eq. (6)) and the relation $\delta h = \delta w \sin\theta + \delta v \cos\theta$ leads to the following expression:

$$\begin{aligned} \mathcal{P}_a &= \int_\Omega \rho \left[\frac{\partial^2 U_o}{\partial t^2}\delta U_o + \left(\frac{\partial^2 V_o}{\partial t^2} - [(a+z)\sin\theta + h]^2\frac{\partial^4 V_o}{\partial t^2 \partial x^2} + \frac{\partial^2 h}{\partial t^2}\right)\delta V_o + \right. \\ &\quad \left. \frac{\partial^2 u}{\partial t^2}\delta u + \left(\frac{\partial^2 v}{\partial t^2} + \frac{\partial^2 V_o}{\partial t^2}\cos\theta\right)\delta v + \left(\frac{\partial^2 w}{\partial t^2} + \frac{\partial^2 V_o}{\partial t^2}\sin\theta\right)\delta w\right] \mathrm{d}V \end{aligned}$$

Then, using the first-order decomposition of the shell-type displacements (cf. Eq. (8)) makes it possible to rewrite the power of inertia as:

$$\begin{aligned} \mathcal{P}_a &= \int_\Omega \rho \left[\frac{\partial^2 U_o}{\partial t^2}\delta U_o + \left(\frac{\partial^2 V_o}{\partial t^2} - [(a+z)\sin\theta + h]^2\frac{\partial^4 V_o}{\partial t^2 \partial x^2} + \frac{\partial^2 h}{\partial t^2}\right)\delta V_o + \right. \\ &\quad \left(\frac{\partial^2 u_o}{\partial t^2} - z\frac{\partial^2 u_1}{\partial t^2}\right)\delta u_o - z\left(\frac{\partial^2 u_o}{\partial t^2} - z\frac{\partial^2 u_1}{\partial t^2}\right)\delta u_1 + \\ &\quad \left(\frac{\partial^2 v_o}{\partial t^2} + z\frac{\partial^2 v_1}{\partial t^2} + \frac{\partial^2 V_o}{\partial t^2}\cos\theta\right)\delta v_o + z\left(\frac{\partial^2 v_o}{\partial t^2} + z\frac{\partial^2 v_1}{\partial t^2} + \frac{\partial^2 V_o}{\partial t^2}\cos\theta\right)\delta v_1 + \\ &\quad \left.\left(\frac{\partial^2 w_o}{\partial t^2} + \frac{\partial^2 V_o}{\partial t^2}\sin\theta\right)\delta w_o\right] \mathrm{d}V \end{aligned}$$

As $\int_{-e/2}^{e/2} z\,\mathrm{d}z = 0$, this relation can be simplified to:

$$\begin{aligned} \mathcal{P}_a &= \int_\Omega \rho \left[\frac{\partial^2 U_o}{\partial t^2}\delta U_o + \left(\frac{\partial^2 V_o}{\partial t^2} - [(a+z)\sin\theta + h]^2\frac{\partial^4 V_o}{\partial t^2 \partial x^2} + \frac{\partial^2 h_o}{\partial t^2}\right)\delta V_o + \right. \\ &\quad \frac{\partial^2 u_o}{\partial t^2}\delta u_o + z^2\frac{\partial^2 u_1}{\partial t^2}\delta u_1 + \left(\frac{\partial^2 v_o}{\partial t^2} + \frac{\partial^2 V_o}{\partial t^2}\cos\theta\right)\delta v_o + z^2\frac{\partial^2 v_1}{\partial t^2}\delta v_1 + \\ &\quad \left.\left(\frac{\partial^2 w_o}{\partial t^2} + \frac{\partial^2 V_o}{\partial t^2}\sin\theta\right)\delta w_o\right] \mathrm{d}V \end{aligned} \tag{B.2}$$

with $h_o = w_o \sin\theta + v_o \cos\theta$. Then, using the Love-Kirchhoff conditions (cf. Eq. (9)) leads to:

$$\begin{aligned} \mathcal{P}_a &= \int_\Omega \rho \left[\frac{\partial^2 U_o}{\partial t^2}\delta U_o + \left(\frac{\partial^2 V_o}{\partial t^2} - [(a+z)\sin\theta + h]^2\frac{\partial^4 V_o}{\partial t^2 \partial x^2} + \frac{\partial^2 h_o}{\partial t^2}\right)\delta V_o + \right. \\ &\quad \frac{\partial^2 u_o}{\partial t^2}\delta u_o + z^2\frac{\partial^3 w_o}{\partial t^2 \partial x}\frac{\partial \delta w_o}{\partial x} + \left(\frac{\partial^2 v_o}{\partial t^2} + \frac{\partial^2 V_o}{\partial t^2}\cos\theta\right)\delta v_o + \\ &\quad \left. + \frac{z^2}{a^2}\left(\frac{\partial^3 w_o}{\partial t^2 \partial\theta} - \frac{\partial^2 v_o}{\partial t^2}\right)\left(\frac{\partial \delta w_o}{\partial \theta} - \delta v_o\right) + \left(\frac{\partial^2 w_o}{\partial t^2} + \frac{\partial^2 V_o}{\partial t^2}\sin\theta\right)\delta w_o\right] \mathrm{d}V \end{aligned}$$

After integration by parts this rewrites as:

$$\begin{aligned}\mathcal{P}_a &= \int_\Omega \rho \left[\frac{\partial^2 U_o}{\partial t^2}\delta U_o + \left(\frac{\partial^2 V_o}{\partial t^2} - [(a+z)\sin\theta + h]^2 \frac{\partial^4 V_o}{\partial t^2 \partial x^2} + \frac{\partial^2 h_o}{\partial t^2} \right) \delta V_o + \right. \\ & \frac{\partial^2 u_o}{\partial t^2}\delta u_o + \left(\frac{\partial^2 v_o}{\partial t^2} + \frac{\partial^2 V_o}{\partial t^2}\cos\theta - \frac{z^2}{a^2}\left(\frac{\partial^3 w_o}{\partial t^2 \partial \theta} - \frac{\partial^2 v_o}{\partial t^2} \right) \right) \delta v_o + \\ & \left. \left(\frac{\partial^2 w_o}{\partial t^2} + \frac{\partial^2 V_o}{\partial t^2}\sin\theta - z^2 \frac{\partial^4 w_o}{\partial t^2 \partial x^2} - \frac{z^2}{a^2}\left(\frac{\partial^4 w_o}{\partial t^2 \partial \theta^2} - \frac{\partial^3 v_o}{\partial t^2 \partial \theta} \right) \right) \delta w_o \right] \mathrm{d}V\end{aligned}$$

The mid-surface displacement field are expressed as Fourier expansions (cf. Eq. (15)). In addition, note that the integral of the product of two Fourier expansions given by:

$$\begin{aligned}\alpha &= \alpha_o^c + \sum_{i=1}^{N_f} \left(\alpha_i^c \cos(i\theta) + \alpha_i^s \sin(i\theta) \right) \\ \beta &= \beta_o^c + \sum_{i=1}^{N_f} \left(\beta_i^c \cos(i\theta) + \beta_i^s \sin(i\theta) \right)\end{aligned}$$

is as follows:

$$\int_0^{2\pi} \alpha\beta \,\mathrm{d}\theta = 2\pi\alpha_o^c\beta_o^c + \pi \sum_{i=1}^{N_f} \left(\alpha_i^c\beta_i^c + \alpha_i^s\beta_i^s \right)$$

As a consequence, the power of inertia is expressed as:

$$\begin{aligned}\mathcal{P}_a &= \int \rho \left[2\pi ae \frac{\partial^2 U_o}{\partial t^2}\delta U_o + \left(2\pi ae \frac{\partial^2 V_o}{\partial t^2} - I_y \frac{\partial^4 V_o}{\partial t^2 \partial x^2} \right) \delta V_o + \right. \\ & \pi ae \sum_{i=2}^{N_f} \left(\frac{\partial^2 u_i^c}{\partial t^2}\delta u_i^c + \frac{\partial^2 u_i^s}{\partial t^2}\delta u_i^s \right) + \pi ae \left(1 + \frac{e^2}{12a^2} \right) \sum_{i=1}^{N_f} \frac{1}{i^2} \left(\frac{\partial^2 w_i^c}{\partial t^2}\delta w_i^c + \frac{\partial^2 w_i^s}{\partial t^2}\delta w_i^s \right) - \pi ae \frac{\partial^2 V_o}{\partial t^2}\delta w_1^s \\ & + \pi ae \frac{e^2}{12a^2} \left(\frac{\partial^2 w_1^c}{\partial t^2}\delta w_1^c + \frac{\partial^2 w_1^s}{\partial t^2}\delta w_1^s - \sum_{i=2}^{N_f} \left(\frac{\partial^2 w_i^c}{\partial t^2}\delta w_i^c + \frac{\partial^2 w_i^s}{\partial t^2}\delta w_i^s \right) \right) + \\ & 2\pi ae \frac{\partial^2 w_o^c}{\partial t^2}\delta w_o^c + \pi ae \sum_{i=1}^{N_f} \left(\frac{\partial^2 w_i^c}{\partial t^2}\delta w_i^c + \frac{\partial^2 w_i^s}{\partial t^2}\delta w_i^s \right) + \pi ae \frac{\partial^2 V_o}{\partial t^2}\delta w_1^s \\ & - 2\pi ae \frac{e^2}{12} \frac{\partial^4 w_o^c}{\partial t^2 \partial x^2}\delta w_o^c - \pi ae \frac{e^2}{12} \sum_{i=1}^{N_f} \left(\frac{\partial^4 w_i^c}{\partial t^2 \partial x^2}\delta w_i^c + \frac{\partial^4 w_i^s}{\partial t^2 \partial x^2}\delta w_i^s \right) + \pi ae \frac{e^2}{12a^2} \sum_{i=1}^{N_f} \left(i^2 \frac{\partial^2 w_i^c}{\partial t^2}\delta w_i^c + i^2 \frac{\partial^2 w_i^s}{\partial t^2}\delta w_i^s \right) \\ & \left. + \pi ae \frac{e^2}{12a^2} \left(\frac{\partial^2 w_1^c}{\partial t^2}\delta w_1^c + \frac{\partial^2 w_1^s}{\partial t^2}\delta w_1^s - \sum_{i=2}^{N_f} \left(\frac{\partial^2 w_i^c}{\partial t^2}\delta w_i^c + \frac{\partial^2 w_i^s}{\partial t^2}\delta w_i^s \right) \right) \right] \mathrm{d}x\end{aligned}$$

as $\int_0^{2\pi} h_o \,\mathrm{d}\theta = 0$ and with the area moment of inertia:

$$I_y = \int_S \left((a+z)\sin\theta + h \right)^2 \mathrm{d}S$$

which can be expressed as:

$$\begin{aligned}I_y &= \pi a^3 e \left(1 + 2\frac{w_o^c}{a} - \frac{3}{2}\frac{w_2^c}{a} + \left(\frac{3}{4}\frac{w_1^s}{a} \right)^2 + \left(\frac{w_o^c}{a} - \frac{3}{4}\frac{w_2^c}{a} \right)^2 + \right. \\ & \frac{1}{4} \sum_{i \geq 2} \left(\left(\frac{i+2}{i+1}\frac{w_{i+1}^s}{a} - \frac{i-2+2\delta_{i2}}{i-1}\frac{w_{i-1}^s}{a} \right)^2 + \left(\frac{i+2}{i+1}\frac{w_{i+1}^c}{a} - \frac{i-2+2\delta_{i2}}{i-1}\frac{w_{i-1}^c}{a} \right)^2 \right) \\ & \left. + \frac{e^2}{12a^2} \left(1 + 4\frac{w_1^c}{a} \right) \right)\end{aligned} \tag{B.3}$$

Note that the moment of inertia for a beam is given by:

$$I_y^b = \pi a^3 e \left(1 + \frac{e^2}{12a^2}\right) \tag{B.4}$$

After some algebraic manipulations, this can be rewritten under the following form:

$$\begin{aligned}
\mathcal{P}_a \;=\; & \int \rho \left[S \frac{\partial^2 U_o}{\partial t^2} \delta U_o + S \left(\frac{\partial^2 V_o}{\partial t^2} - \frac{I_y}{S} \frac{\partial^4 V_o}{\partial t^2 \partial x^2} \right) \delta V_o + \right. \\
& \pi a e \sum_{i=2}^{N_f} \left(\frac{\partial^2 u_i^c}{\partial t^2} \delta u_i^c + \frac{\partial^2 u_i^s}{\partial t^2} \delta u_i^s \right) + 2\pi a e \left(\frac{\partial^2 w_o^c}{\partial t^2} - \frac{e^2}{12} \frac{\partial^4 w_o^c}{\partial t^2 \partial x^2} \right) \delta w_o^c + \\
& 2\pi a e \left(1 + 2\frac{e^2}{12a^2}\right) \left(\frac{\partial^2 w_1^c}{\partial t^2} \delta w_1^c + \frac{\partial^2 w_1^s}{\partial t^2} \delta w_1^s \right) - \pi a \frac{e^3}{12} \left(\frac{\partial^4 w_1^c}{\partial t^2 \partial x^2} \delta w_1^c + \frac{\partial^4 w_1^s}{\partial t^2 \partial x^2} \delta w_1^s \right) \\
& + \pi a e \sum_{i=2}^{N_f} \frac{i^2+1}{i^2} \left(\frac{\partial^2 w_i^c}{\partial t^2} \delta w_i^c + \frac{\partial^2 w_i^s}{\partial t^2} \delta w_i^s \right) + \pi a \frac{e^3}{12a^2} \sum_{i=2}^{N_f} \frac{\left(i^2-1\right)^2}{i^2} \left(\frac{\partial^2 w_i^c}{\partial t^2} \delta w_i^c + \frac{\partial^2 w_i^s}{\partial t^2} \delta w_i^s \right) \\
& \left. - \pi a \frac{e^3}{12} \sum_{i=2}^{N_f} \left(\frac{\partial^4 w_i^c}{\partial t^2 \partial x^2} \delta w_i^c + \frac{\partial^4 w_i^s}{\partial t^2 \partial x^2} \delta w_i^s \right) \right] \mathrm{d}x
\end{aligned} \tag{B.5}$$

with $S = 2\pi a e$.

Appendix B.2. Power of internal forces

The power of internal forces is now expressed using the stress-strain relation. Following the decomposition $\boldsymbol{\varepsilon} = \boldsymbol{\varepsilon}^m + z\mathbf{k}$, the stress tensor can also be decomposed as:

$$\boldsymbol{\sigma} = \boldsymbol{\sigma}^m + z\boldsymbol{\sigma}^k \quad \text{with} \quad \boldsymbol{\sigma}^m = \frac{E}{1-\nu^2} \left((1-\nu)\, \boldsymbol{\varepsilon}^m + \nu\, \mathrm{trac}(\boldsymbol{\varepsilon}^m)\, \mathbf{I} \right) \quad \text{and} \quad \boldsymbol{\sigma}^k = \frac{E}{1-\nu^2} \left((1-\nu)\, \mathbf{k} + \nu\, \mathrm{trac}(\mathbf{k})\, \mathbf{I} \right)$$

The power of internal forces can thus be expressed as:

$$\mathcal{P}_i = -\int_\Omega \left(\boldsymbol{\sigma}^m : \delta\, \boldsymbol{\varepsilon}^m + z^2 \boldsymbol{\sigma}^k : \delta \mathbf{k} \right) \mathrm{d}V \tag{B.6}$$

as $\int_{-e/2}^{e/2} z\, \mathrm{d}z = 0$. Based on the strain-displacement relationship expressed in Eq. (11), we can write:

$$\begin{aligned}
\mathcal{P}_i \;=\; & -\int_\Omega \left[\sigma_{xx}^m \left(\frac{\partial \delta U_o}{\partial x} - a \sin\theta \frac{\partial^2 \delta V_o}{\partial x^2} + \frac{\partial \delta u_o}{\partial x} - \frac{\partial^2 \delta V_o}{\partial x^2} h_o - \frac{\partial^2 V_o}{\partial x^2} \left(\delta w_o \sin\theta + \delta v_o \cos\theta \right) \right) + \right. \\
& z^2 \sigma_{xx}^k \left(-\sin\theta \frac{\partial^2 \delta V_o}{\partial x^2} - \frac{\partial^2 \delta w_o}{\partial x^2} + \frac{\cos\theta}{a} \frac{\partial^2 \delta V_o}{\partial x^2} \left(\frac{\partial w_o}{\partial \theta} - v_o \right) + \frac{\cos\theta}{a} \frac{\partial^2 V_o}{\partial x^2} \left(\frac{\partial \delta w_o}{\partial \theta} - \delta v_o \right) \right) + \\
& \sigma_{\theta\theta}^m \frac{1}{a} \left(\frac{\partial \delta v_o}{\partial \theta} + \delta w_o \right) - \sigma_{\theta\theta}^k \frac{z^2}{a^2} \left(\frac{\partial^2 \delta w_o}{\partial \theta^2} + \delta w_o \right) + \\
& \left. \sigma_{x\theta}^m \left(\frac{1}{a} \frac{\partial \delta u_o}{\partial \theta} + \frac{\partial \delta v_o}{\partial x} \right) - \sigma_{x\theta}^k \frac{z^2}{a} \left(2 \frac{\partial^2 \delta w_o}{\partial x \partial \theta} + \frac{1}{a} \frac{\partial \delta u_o}{\partial \theta} - \frac{\partial \delta v_o}{\partial x} \right) \right] \mathrm{d}V
\end{aligned} \tag{B.7}$$

which can be rearranged as:

$$\begin{aligned}
\mathcal{P}_i \;=\; & -\int_\Omega \left[\sigma_{xx}^m \frac{\partial \delta U_o}{\partial x} - \sigma_{xx} \left((a+z)\sin\theta + h_o - \frac{z}{a} \cos\theta \left(\frac{\partial w_o}{\partial \theta} - v_o \right) \right) \frac{\partial^2 \delta V_o}{\partial x^2} + \right. \\
& \sigma_{xx}^m \frac{\partial \delta u_o}{\partial x} + \frac{1}{a} \left(\sigma_{x\theta}^m - \frac{z^2}{a} \sigma_{x\theta}^k \right) \frac{\partial \delta u_o}{\partial \theta} + \\
& \left(-\sigma_{xx}^m \frac{\partial^2 V_o}{\partial x^2} \sin\theta + \frac{1}{a} \left(\sigma_{\theta\theta}^m - \frac{z^2}{a} \sigma_{\theta\theta}^k \right) \right) \delta w_o + \frac{z^2}{a} \sigma_{xx}^k \frac{\partial^2 V_o}{\partial x^2} \cos\theta \frac{\partial \delta w_o}{\partial \theta} - \frac{z^2}{a^2} \sigma_{\theta\theta}^k \frac{\partial^2 \delta w_o}{\partial \theta^2} \\
& -2 \frac{z^2}{a} \sigma_{x\theta}^k \frac{\partial^2 \delta w_o}{\partial x \partial \theta} - z^2 \sigma_{xx}^k \frac{\partial^2 \delta w_o}{\partial x^2} \\
& \left. - \left(\sigma_{xx}^m + \frac{z^2}{a} \sigma_{xx}^k \right) \frac{\partial^2 V_o}{\partial x^2} \cos\theta \delta v_o + \left(\sigma_{x\theta}^m + \frac{z^2}{a} \sigma_{x\theta}^k \right) \frac{\partial \delta v_o}{\partial x} + \sigma_{\theta\theta}^m \frac{1}{a} \frac{\partial \delta v_o}{\partial \theta} \right] \mathrm{d}V
\end{aligned}$$

The mid-surface displacement virtual field is now expanded in Fourier series as in Eq. (15):

$$
\begin{aligned}
\mathcal{P}_i \;=\; & -\int_\Omega \Bigg[\sigma^m_{xx} \frac{\partial \delta U_o}{\partial x} - \sigma_{xx}\left((a+z)\sin\theta + h\right)\frac{\partial^2 \delta V_o}{\partial x^2} + \\
& \sigma^m_{xx} \sum_{i=2}^{N_f} \left(\frac{\partial \delta u^c_i}{\partial x}\cos(i\theta) + \frac{\partial \delta u^s_i}{\partial x}\sin(i\theta) \right) + \frac{1}{a}\left(\sigma^m_{x\theta} - \frac{z^2}{a}\sigma^k_{x\theta} \right) \sum_{i=2}^{N_f} i \left(-\delta u^c_i \sin(i\theta) + \delta u^s_i \cos(i\theta) \right) + \\
& \left(-\sigma^m_{xx}\frac{\partial^2 V_o}{\partial x^2}\sin\theta + \frac{1}{a}\left(\sigma^m_{\theta\theta} - \frac{z^2}{a}\sigma^k_{\theta\theta} \right) \right) \left(\delta w^c_o + \delta w^c_1 \cos\theta + \delta w^s_1 \sin\theta + \sum_{i=2}^{N_f} \left(\delta w^c_i \cos(i\theta) + \delta w^s_i \sin(i\theta) \right) \right) \\
& + \sigma^k_{xx}\frac{z^2}{a}\frac{\partial^2 V_o}{\partial x^2}\cos\theta \left(-\delta w^c_1 \sin\theta + \delta w^s_1 \cos\theta + \sum_{i=2}^{N_f} i \left(-\delta w^c_i \sin(i\theta) + \delta w^s_i \cos(i\theta) \right) \right) \\
& + \sigma^k_{\theta\theta}\frac{z^2}{a^2} \left(\delta w^c_1 \cos\theta + \delta w^s_1 \sin\theta + \sum_{i=2}^{N_f} i^2 \left(\delta w^c_i \cos(i\theta) + \delta w^s_i \sin(i\theta) \right) \right) \\
& - 2\frac{z^2}{a}\sigma^k_{x\theta} \left(-\frac{\partial \delta w^c_1}{\partial x}\sin\theta + \frac{\partial \delta w^s_1}{\partial x}\cos\theta + \sum_{i=2}^{N_f} i \left(-\frac{\partial \delta w^c_i}{\partial x}\sin(i\theta) + \frac{\partial \delta w^s_i}{\partial x}\cos(i\theta) \right) \right) \\
& - z^2 \sigma^k_{xx} \left(\frac{\partial^2 \delta w^c_o}{\partial x^2} + \frac{\partial^2 \delta w^c_1}{\partial x^2}\cos\theta + \frac{\partial^2 \delta w^s_1}{\partial x^2}\sin\theta + \sum_{i=2}^{N_f} \left(\frac{\partial^2 \delta w^c_i}{\partial x^2}\cos(i\theta) + \frac{\partial^2 \delta w^s_i}{\partial x^2}\sin(i\theta) \right) \right) \\
& - \left(\sigma^m_{xx} + \frac{z^2}{a}\sigma^k_{xx} \right) \frac{\partial^2 V_o}{\partial x^2}\cos\theta \left(-\delta w^s_1 \cos\theta + \delta w^c_1 \sin\theta + \sum_{i=2}^{N_f} \frac{1}{i} \left(\delta w^s_i \cos(i\theta) - \delta w^c_i \sin(i\theta) \right) \right) \\
& + \sigma^m_{\theta\theta}\frac{1}{a} \left(\delta w^c_1 \cos\theta + \delta w^s_1 \sin\theta - \sum_{i=2}^{N_f} \left(\delta w^s_i \sin(i\theta) + \delta w^c_i \cos(i\theta) \right) \right) \\
& + \left(\sigma^m_{x\theta} + \frac{z^2}{a}\sigma^k_{x\theta} \right) \left(-\frac{\partial \delta w^s_1}{\partial x}\cos\theta + \frac{\partial \delta w^c_1}{\partial x}\sin\theta + \sum_{i=2}^{N_f} \frac{1}{i} \left(\frac{\partial \delta w^s_i}{\partial x}\cos(i\theta) - \frac{\partial \delta w^c_i}{\partial x}\sin(i\theta) \right) \right) \Bigg] \, \mathrm{d}V
\end{aligned}
$$

Introducing the *generalized* forces and moments associated with the beam-type and shell-type motions, this can be rewritten as:

$$
\begin{aligned}
\mathcal{P}_i \;=\; & -\int_0^L \Bigg[N\frac{\partial \delta U_o}{\partial x} - M_y \frac{\partial^2 \delta V_o}{\partial x^2} + \sum_{i=2}^{N_f} \left((t_u)^c_i \, \delta u^c_i + (t_u)^s_i \, \delta u^s_i \right) + \sum_{i=2}^{N_f} \left((n_u)^c_i \frac{\partial \delta u^c_i}{\partial x} + (n_u)^s_i \frac{\partial \delta u^s_i}{\partial x} \right) + \\
& (t_w)^c_o \, \delta w^c_o - (m_w)^c_o \frac{\partial^2 \delta w^c_o}{\partial x^2} + \\
& (t_w)^c_1 \, \delta w^c_1 + (t_w)^s_1 \, \delta w^s_1 + (n_w)^c_1 \frac{\partial \delta w^c_1}{\partial x} + (n_w)^s_1 \frac{\partial \delta w^s_1}{\partial x} - (m_w)^c_1 \frac{\partial^2 \delta w^c_1}{\partial x^2} - (m_w)^s_1 \frac{\partial^2 \delta w^s_1}{\partial x^2} \\
& \sum_{i=2}^{N_f} \left((t_w)^c_i \, \delta w^c_i + (t_w)^s_i \, \delta w^s_i + (n_w)^c_i \frac{\partial \delta w^c_i}{\partial x} + (n_w)^s_i \frac{\partial \delta w^s_i}{\partial x} - (m_w)^c_i \frac{\partial^2 \delta w^c_i}{\partial x^2} - (m_w)^s_i \frac{\partial^2 \delta w^s_i}{\partial x^2} \right) \Bigg] \, \mathrm{d}x
\end{aligned}
\tag{B.8}
$$

with the following definition of the generalized forces and moments:

$$
\left\{
\begin{array}{lcl}
N & = & \displaystyle\int_S \sigma^m_{xx}\,\mathrm{d}S \\
M_y & = & \displaystyle\int_S \sigma_{xx}\left((a+z)\sin\theta + h\right)\,\mathrm{d}S \\
(t_u)^c_i & = & \displaystyle -i\int_S \frac{1}{a}\left(\sigma^m_{x\theta} - \frac{z^2}{a}\sigma^k_{x\theta}\right)\sin(i\theta)\,\mathrm{d}S \\
(t_u)^s_i & = & \displaystyle +i\int_S \frac{1}{a}\left(\sigma^m_{x\theta} - \frac{z^2}{a}\sigma^k_{x\theta}\right)\cos(i\theta)\,\mathrm{d}S \\
(n_u)^c_i & = & \displaystyle\int_S \sigma^m_{xx}\cos(i\theta)\,\mathrm{d}S \\
(n_u)^s_i & = & \displaystyle\int_S \sigma^m_{xx}\sin(i\theta)\,\mathrm{d}S \\
(t_w)^c_o & = & \displaystyle\int_S \left(-\sigma^m_{xx}\frac{\partial^2 V_o}{\partial x^2}\sin\theta + \frac{1}{a}\left(\sigma^m_{\theta\theta} - \frac{z^2}{a}\sigma^k_{\theta\theta}\right)\right)\,\mathrm{d}S \\
(m_w)^c_o & = & \displaystyle\int_S z^2\sigma^k_{xx}\,\mathrm{d}S \\
(t_w)^c_1 & = & \displaystyle\int_S 2\left(-\left(\sigma^m_{xx} + \frac{z^2}{a}\sigma^k_{xx}\right)\frac{\partial^2 V_o}{\partial x^2}\cos\theta\sin\theta + \frac{1}{a}\sigma^m_{\theta\theta}\cos\theta\right)\,\mathrm{d}S \\
(t_w)^s_1 & = & \displaystyle\int_S \left(\left(\sigma^m_{xx}\left(\cos^2\theta - \sin^2\theta\right) + 2\frac{z^2}{a}\sigma^k_{xx}\cos^2\theta\right)\frac{\partial^2 V_o}{\partial x^2} + 2\frac{1}{a}\sigma^m_{\theta\theta}\sin\theta\right)\,\mathrm{d}S \\
(n_w)^c_1 & = & \displaystyle +\int_S \left(\sigma^m_{x\theta} + 3\frac{z^2}{a}\sigma^k_{x\theta}\right)\sin\theta\,\mathrm{d}S \\
(n_w)^s_1 & = & \displaystyle -\int_S \left(\sigma^m_{x\theta} + 3\frac{z^2}{a}\sigma^k_{x\theta}\right)\cos\theta\,\mathrm{d}S \\
(m_w)^c_1 & = & \displaystyle\int_S z^2\sigma^k_{xx}\cos\theta\,\mathrm{d}S \\
(m_w)^s_1 & = & \displaystyle\int_S z^2\sigma^k_{xx}\sin\theta\,\mathrm{d}S \\
(t_w)^c_i & = & \displaystyle\int_S \left(+\frac{1}{i}\sigma^m_{xx}\frac{\partial^2 V_o}{\partial x^2}\left(\cos\theta\sin(i\theta) - i\sin\theta\cos(i\theta)\right) + \left(i^2-1\right)\frac{z^2}{a^2}\sigma^k_{\theta\theta}\cos(i\theta) - \frac{i^2-1}{i}\sigma^k_{xx}\frac{z^2}{a}\frac{\partial^2 V_o}{\partial x^2}\cos\theta\sin(i\theta)\right)\,\mathrm{d}S \\
(t_w)^s_i & = & \displaystyle\int_S \left(-\frac{1}{i}\sigma^m_{xx}\frac{\partial^2 V_o}{\partial x^2}\left(\cos\theta\cos(i\theta) + i\sin\theta\sin(i\theta)\right) + \left(i^2-1\right)\frac{z^2}{a^2}\sigma^k_{\theta\theta}\sin(i\theta) + \frac{i^2-1}{i}\sigma^k_{xx}\frac{z^2}{a}\frac{\partial^2 V_o}{\partial x^2}\cos\theta\cos(i\theta)\right)\,\mathrm{d}S \\
(n_w)^c_i & = & \displaystyle -\int_S \frac{1}{i}\left(\sigma^m_{x\theta} + \left(1-2i^2\right)\frac{z^2}{a}\sigma^k_{x\theta}\right)\sin(i\theta)\,\mathrm{d}S \\
(n_w)^s_i & = & \displaystyle +\int_S \frac{1}{i}\left(\sigma^m_{x\theta} + \left(1-2i^2\right)\frac{z^2}{a}\sigma^k_{x\theta}\right)\cos(i\theta)\,\mathrm{d}S \\
(m_w)^c_i & = & \displaystyle\int_S z^2\sigma^k_{xx}\cos(i\theta)\,\mathrm{d}S \\
(m_w)^s_i & = & \displaystyle\int_S z^2\sigma^k_{xx}\sin(i\theta)\,\mathrm{d}S
\end{array}
\right.
$$

for $i \geq 2$ with the following components of the stress-tensor:

$$\left\{\begin{array}{l}
\sigma^m_{xx} = \dfrac{E}{1-\nu^2}\left(\dfrac{\partial U_o}{\partial x} - a\sin\theta\dfrac{\partial^2 V_o}{\partial x^2} + \dfrac{\partial u_o}{\partial x} - \dfrac{\partial^2 V_o}{\partial x^2}\left(w_o\sin\theta + v_o\cos\theta\right) + \nu\dfrac{1}{a}\left(\dfrac{\partial v_o}{\partial\theta} + w_o\right)\right)\\
\sigma^m_{\theta\theta} = \dfrac{E}{1-\nu^2}\left(\dfrac{1}{a}\left(\dfrac{\partial v_o}{\partial\theta} + w_o\right) + \nu\left(\dfrac{\partial U_o}{\partial x} - a\sin\theta\dfrac{\partial^2 V_o}{\partial x^2} + \dfrac{\partial u_o}{\partial x} - \dfrac{\partial^2 V_o}{\partial x^2}\left(w_o\sin\theta + v_o\cos\theta\right)\right)\right)\\
\sigma^m_{x\theta} = \dfrac{E}{1+\nu}\dfrac{1}{2}\left(\dfrac{1}{a}\dfrac{\partial u_o}{\partial\theta} + \dfrac{\partial v_o}{\partial x}\right)\\
\sigma^k_{xx} = \dfrac{E}{1-\nu^2}\left(-\sin\theta\dfrac{\partial^2 V_o}{\partial x^2} - \dfrac{\partial^2 w_o}{\partial x^2} + \dfrac{\cos\theta}{a}\dfrac{\partial^2 V_o}{\partial x^2}\left(\dfrac{\partial w_o}{\partial\theta} - v_o\right) - \nu\dfrac{1}{a^2}\left(\dfrac{\partial^2 w_o}{\partial\theta^2} + w_o\right)\right)\\
\sigma^k_{\theta\theta} = \dfrac{E}{1-\nu^2}\left(-\dfrac{1}{a^2}\left(\dfrac{\partial^2 w_o}{\partial\theta^2} + w_o\right) + \nu\left(-\sin\theta\dfrac{\partial^2 V_o}{\partial x^2} - \dfrac{\partial^2 w_o}{\partial x^2} + \dfrac{\cos\theta}{a}\dfrac{\partial^2 V_o}{\partial x^2}\left(\dfrac{\partial w_o}{\partial\theta} - v_o\right)\right)\right)\\
\sigma^k_{x\theta} = -\dfrac{E}{1+\nu}\dfrac{1}{2a}\left(2\dfrac{\partial^2 w_o}{\partial x\partial\theta} + \dfrac{1}{a}\dfrac{\partial u_o}{\partial\theta} - \dfrac{\partial v_o}{\partial x}\right)
\end{array}\right.$$

N and M_y are the axial force and the in-plane bending moment, respectively, associated with the beam-type DOFs. $(t_u)_i^{c/s}$ and $(n_u)_i^{c/s}$ are the forces associated with the cross-section warping. $(t_w)_o^c$ and $(m_w)_o^c$ are associated to the radial expansion/contraction of the tube cross-section while $(t_w)_1^{c/s}$, $(n_w)_1^{c/s}$ and $(m_w)_1^{c/s}$ are linked to the vanishing rigid-body of the tube cross-section. Finally, $(t_w)_i^{c/s}$, $(n_w)_i^{c/s}$ and $(m_w)_i^{c/s}$ for $i \geq 2$ correspond to the forces associated to the tube cross-section distortion.

The axial force and the in-plane bending moment corresponding to the beam motion are expressed as:

$$\left\{\begin{array}{rcl}
N &=& +\dfrac{ES}{1-\nu^2}\left(\dfrac{\partial U_o}{\partial x} + \nu\dfrac{w_o^c}{a}\right)\\
M_y &=& -\dfrac{EI_y}{1-\nu^2}\dfrac{\partial^2 V_o}{\partial x^2}\\
&& +\dfrac{ES}{1-\nu^2}\dfrac{1}{2}\left(\displaystyle\sum_{i\geq 2}\dfrac{1}{2}\left(\dfrac{\partial u_i^c}{\partial x}\left(\dfrac{i+2}{i+1}w_{i+1}^s - \dfrac{i-2+2\delta_{i2}}{i-1}w_{i-1}^s\right) - \dfrac{\partial u_i^s}{\partial x}\left(\dfrac{i+2}{i+1}w_{i+1}^c - \dfrac{i-2+2\delta_{i2}}{i-1}w_{i-1}^c\right)\right)\right.\\
&& \left. -\dfrac{e^2}{12}\dfrac{\partial^2 w_1^s}{\partial x^2} + 2\nu w_1^s\right)
\end{array}\right. \tag{B.9}$$

It has to be noticed that N corresponds to the classical axial force of a beam with an additional term related to the cross-section expansion/contraction corresponding to the Poisson effect. M_y involve two type of terms: the first one is similar to the beam-type bending moment with the *modified* moment of inertia given in Eq. (B.3) whereas the second one are due to the non-linear coupling.

Then, the forces corresponding to the cross-section warping are expressed for $i \geq 2$ as:

$$\left\{\begin{array}{rcl}
(t_u)_i^c &=& +\dfrac{ES}{1+\nu}\dfrac{1}{4a}\left(i^2\left(1+\dfrac{e^2}{12a^2}\right)\dfrac{u_i^c}{a} + \left(1+\dfrac{e^2}{12a^2}\left(2i^2-1\right)\right)\dfrac{\partial w_i^c}{\partial x}\right)\\
(t_u)_i^s &=& +\dfrac{ES}{1+\nu}\dfrac{1}{4a}\left(i^2\left(1+\dfrac{e^2}{12a^2}\right)\dfrac{u_i^s}{a} + \left(1+\dfrac{e^2}{12a^2}\left(2i^2-1\right)\right)\dfrac{\partial w_i^s}{\partial x}\right)\\
(n_u)_i^c &=& +\dfrac{ES}{1-\nu^2}\dfrac{1}{2}\left(\dfrac{\partial u_i^c}{\partial x} + \dfrac{1}{2}\dfrac{\partial^2 V_o}{\partial x^2}\left(\dfrac{i-2+2\delta_{i2}}{i-1}w_{i-1}^s - \dfrac{i+2}{i+1}w_{i+1}^s\right)\right)\\
(n_u)_i^s &=& +\dfrac{ES}{1-\nu^2}\dfrac{1}{2}\left(\dfrac{\partial u_i^s}{\partial x} - \dfrac{1}{2}\dfrac{\partial^2 V_o}{\partial x^2}\left(\dfrac{i-2+2\delta_{i2}}{i-1}w_{i-1}^c - \dfrac{i+2}{i+1}w_{i+1}^c\right)\right)
\end{array}\right. \tag{B.10}$$

The moments and forces associated to the mode 0 in the Fourier expansion of the cross-section deformation are given by:

$$\left\{\begin{array}{lcl}(t_w)_o^c & = & +\dfrac{ES}{1-\nu^2}\left(\dfrac{1}{a}\left(\dfrac{w_o^c}{a}+\nu\dfrac{\partial U_o}{\partial x}\right)+\dfrac{1}{2}\left(a+\dfrac{1}{2}\left(2w_o^c-\dfrac{3}{2}w_2^c\right)\right)\left(\dfrac{\partial^2 V_o}{\partial x^2}\right)^2-\nu\dfrac{w_1^s}{a}\dfrac{\partial^2 V_o}{\partial x^2}+\dfrac{e^2}{12a^2}\left(\dfrac{w_o^c}{a^2}+\nu\left(\dfrac{\partial^2 w_o^c}{\partial x^2}-\dfrac{w_1^s}{a}\dfrac{\partial^2 V_o}{\partial x^2}\right)\right)\right)\\ (m_w)_o^c & = & -\dfrac{ES}{1-\nu^2}\dfrac{e^2}{12}\left(\dfrac{\partial^2 w_o^c}{\partial x^2}-\dfrac{\partial^2 V_o}{\partial x^2}\dfrac{w_1^s}{a}+\nu\dfrac{w_o^c}{a^2}\right)\end{array}\right. \tag{B.11}$$

In addition, the moments and forces associated to the mode 1 in the Fourier expansion of the cross-section deformation are given by:

$$\left\{\begin{array}{lcl}(t_w)_1^c & = & +\dfrac{ES}{1-\nu^2}\left(2\dfrac{w_1^c}{a^2}-\dfrac{1}{2}\dfrac{\partial^2 V_o}{\partial x^2}\left(\dfrac{\partial u_2^s}{\partial x}-\dfrac{e^2}{12a}\dfrac{\partial^2 w_2^s}{\partial x^2}\right)-\nu\dfrac{\partial^2 V_o}{\partial x^2}\dfrac{3}{4}\left(1+2\dfrac{e^2}{12a^2}\right)\dfrac{w_2^s}{a}\right.\\ & & \left.+\dfrac{1}{4}\left(\dfrac{\partial^2 V_o}{\partial x^2}\right)^2\left(2\left(1+\dfrac{e^2}{12a^2}\right)w_1^c-\dfrac{4}{3}\left(1-2\dfrac{e^2}{12a^2}\right)w_3^c\right)\right)\\ (t_w)_1^s & = & +\dfrac{ES}{1-\nu^2}\left(2\dfrac{w_1^s}{a^2}+\dfrac{1}{2}\dfrac{\partial^2 V_o}{\partial x^2}\left(\dfrac{\partial u_2^c}{\partial x}-\dfrac{e^2}{12a}\left(\dfrac{\partial^2 w_2^c}{\partial x^2}+2\dfrac{\partial^2 w_o^c}{\partial x^2}\right)\right)-\nu\dfrac{\partial^2 V_o}{\partial x^2}\left(1+\left(1+\dfrac{e^2}{12a^2}\right)\dfrac{w_o^c}{a}-\dfrac{3}{4}\left(1+2\dfrac{e^2}{12a^2}\right)\dfrac{w_2^c}{a}\right)\right.\\ & & \left.+\dfrac{1}{4}\left(\dfrac{\partial^2 V_o}{\partial x^2}\right)^2\left(2\left(1+\dfrac{e^2}{12a^2}\right)w_1^s-\dfrac{4}{3}\left(1-2\dfrac{e^2}{12a^2}\right)w_3^s\right)\right)\\ (n_w)_1^c & = & +\dfrac{ES}{1+\nu}\dfrac{1}{4}\left(1+9\dfrac{e^2}{12a^2}\right)\dfrac{\partial w_1^c}{\partial x}\\ (n_w)_1^s & = & +\dfrac{ES}{1+\nu}\dfrac{1}{4}\left(1+9\dfrac{e^2}{12a^2}\right)\dfrac{\partial w_1^s}{\partial x}\\ (m_w)_1^c & = & -\dfrac{ES}{1-\nu^2}\dfrac{e^2}{24}\left(\dfrac{\partial^2 w_1^c}{\partial x^2}+\dfrac{\partial^2 V_o}{\partial x^2}\dfrac{3w_2^s}{4a}\right)\\ (m_w)_1^s & = & -\dfrac{ES}{1-\nu^2}\dfrac{e^2}{24}\left(\dfrac{\partial^2 w_1^s}{\partial x^2}+\dfrac{\partial^2 V_o}{\partial x^2}\left(1+\dfrac{3w_2^c}{4a}\right)\right)\end{array}\right. \tag{B.12}$$

Finally, the moments and forces associated to the mode i (for $i \geq 2$) in the Fourier expansion of the cross-section deformation are expressed as:

$$
\left\{
\begin{aligned}
(t_w)_i^c &= \frac{ES}{1-\nu^2}\left(\frac{i^2-1}{2}\frac{e^2}{12a^2}\left(\left(i^2-1\right)\frac{w_i^c}{a^2}-\nu\frac{\partial^2 w_i^c}{\partial x^2}\right)-\frac{1}{4i}\frac{\partial^2 V_o}{\partial x^2}\left((i-1)\frac{\partial u_{i+1}^s}{\partial x}-(i+1)\frac{\partial u_{i-1}^s}{\partial x}+\left(i^2-1\right)\frac{e^2}{12a}\left(-\frac{\partial^2 w_{i+1}^s}{\partial x^2}-\frac{\partial^2 w_{i-1}^s}{\partial x^2}\right)\right)\right.\\
&\quad +\nu\frac{\partial^2 V_o}{\partial x^2}\left(\frac{i+1}{2i}\delta_{i2}\frac{w_{i-1}^s}{a}+\frac{i^2-1}{4}\frac{e^2}{12a^2}\left(\frac{i-2+2\delta_{i2}}{i-1}\frac{w_{i-1}^s}{a}-\frac{i+2}{i+1}\frac{w_{i+1}^s}{a}\right)\right)\\
&\quad +\frac{1}{8i}\left(\frac{\partial^2 V_o}{\partial x^2}\right)^2\left(-2(i+1)a\delta_{i2}-\frac{(i+1)(i-2-(1-\delta_{i2})(1-2\delta_{i3}))}{i-2}w_{i-2}^c+\frac{(i-1)^2+(i+1)^2}{i}w_i^c-\frac{(i-1)(i+3)}{i+2}w_{i+2}^c\right.\\
&\quad \left.\left.+\left(i^2-1\right)\frac{e^2}{12a^2}\left(2a\delta_{i2}+\frac{(i-2)^2-1+2\delta_{i3}}{i-2}(1-\delta_{i2})w_{i-2}^c+2\frac{i^2-1}{i}w_i^c+\frac{(i+2)^2-1}{i+2}w_{i+2}^c\right)\right)\right)\\
(t_w)_i^s &= \frac{ES}{1-\nu^2}\left(\frac{i^2-1}{2}\frac{e^2}{12a^2}\left(\left(i^2-1\right)\frac{w_i^s}{a^2}-\nu\frac{\partial^2 w_i^s}{\partial x^2}\right)+\frac{1}{4i}\frac{\partial^2 V_o}{\partial x^2}\left((i-1)\frac{\partial u_{i+1}^c}{\partial x}-(i+1)\frac{\partial u_{i-1}^c}{\partial x}+\left(i^2-1\right)\frac{e^2}{12a}\left(-\frac{\partial^2 w_{i+1}^c}{\partial x^2}-\frac{\partial^2 w_{i-1}^c}{\partial x^2}\right)\right)\right.\\
&\quad -\nu\frac{\partial^2 V_o}{\partial x^2}\left(\frac{i+1}{2i}\delta_{i2}\frac{w_{i-1}^c}{a}+\frac{i^2-1}{4}\frac{e^2}{12a^2}\left(\frac{i-2+2\delta_{i2}}{i-1}\frac{w_{i-1}^c}{a}-\frac{i+2}{i+1}\frac{w_{i+1}^c}{a}\right)\right)\\
&\quad +\frac{1}{8i}\left(\frac{\partial^2 V_o}{\partial x^2}\right)^2\left(-\frac{(i+1)(i-3+2\delta_{i3})}{i-2}(1-\delta_{i2})w_{i-2}^s+\frac{(i-1)^2+(i+1)^2}{i}w_i^s-\frac{(i-1)(i+3)}{i+2}w_{i+2}^s\right.\\
&\quad \left.\left.+\left(i^2-1\right)\frac{e^2}{12a^2}\left(\frac{(i-2)^2-1+2\delta_{i3}}{i-2}(1-\delta_{i2})w_{i-2}^s+2\frac{i^2-1}{i}w_i^s+\frac{(i+2)^2-1}{i+2}w_{i+2}^s\right)\right)\right)\\
(n_w)_i^c &= +\frac{ES}{1+\nu}\frac{1}{4}\left(\left(1+\left(2i^2-1\right)\frac{e^2}{12a^2}\right)\frac{u_i^c}{a}+\frac{1}{i^2}\left(1+\left(2i^2-1\right)^2\frac{e^2}{12a^2}\right)\frac{\partial w_i^c}{\partial x}\right)\\
(n_w)_i^s &= +\frac{ES}{1+\nu}\frac{1}{4}\left(\left(1+\left(2i^2-1\right)\frac{e^2}{12a^2}\right)\frac{u_i^s}{a}+\frac{1}{i^2}\left(1+\left(2i^2-1\right)^2\frac{e^2}{12a^2}\right)\frac{\partial w_i^s}{\partial x}\right)\\
(m_w)_i^c &= -\frac{ES}{1-\nu^2}\frac{e^2}{24}\left(\frac{\partial^2 w_i^c}{\partial x^2}-\frac{1}{2}\frac{\partial^2 V_o}{\partial x^2}\left(\frac{(i+1)^2-1}{i+1}\frac{w_{i+1}^s}{a}+\frac{(i-1)^2-1+2\delta_{i2}}{i-1}\frac{w_{i-1}^s}{a}\right)-\nu\left(i^2-1\right)\frac{w_i^c}{a^2}\right)\\
(m_w)_i^s &= -\frac{ES}{1-\nu^2}\frac{e^2}{24}\left(\frac{\partial^2 w_i^s}{\partial x^2}+\frac{1}{2}\frac{\partial^2 V_o}{\partial x^2}\left(\frac{(i+1)^2-1}{i+1}\frac{w_{i+1}^c}{a}+\frac{(i-1)^2-1+2\delta_{i2}}{i-1}\frac{w_{i-1}^c}{a}\right)-\nu\left(i^2-1\right)\frac{w_i^s}{a^2}\right)
\end{aligned}
\right.
\tag{B.13}
$$

Terms in magenta in the previous equations are due to the non-linear coupling between the axis rotation and the cross-section deformation. First, it has to be noticed that without this coupling, the forces corresponding to mode i depends only on DOFs of mode i. In contrary, terms with $\partial^2_{x^2}V_o$ involves DOFs of mode $i-1$, i and $i+1$ whereas terms with $\left(\partial^2_{x^2}V_o\right)^2$ involves DOFs of mode $i-2$, i and $i+2$. Finally, the cross-section warping and the cross-section ovalization are connected through the forces $(t_u)_i^{c/s}$, $(n_u)_i^{c/s}$, $(t_w)_i^{c/s}$ and $(n_w)_i^{c/s}$. Terms in blue in the previous equations involved the ratio $e^2/12a^2$ which can be neglected in the case of very thin-walled tubes.

Appendix B.3. Tube equations of motion

Finally, the equations of motion of the tube are:

$$
\left\{\begin{array}{llllll}
\rho S\dfrac{\partial^2 U_o}{\partial t^2} & & & -\dfrac{\partial N}{\partial x} & & = 0 \\
\rho S\left(\dfrac{\partial^2 V_o}{\partial t^2}-\dfrac{I_y}{S}\dfrac{\partial^4 V_o}{\partial t^2\partial x^2}\right) & & -\dfrac{\partial^2 M_y}{\partial x^2} & & & = 0 \\
\rho S\left(\dfrac{\partial^2 w_o^c}{\partial t^2}-\dfrac{e^2}{12}\dfrac{\partial^4 w_o^c}{\partial t^2\partial x^2}\right) & & -\dfrac{\partial^2 (m_w)_o^c}{\partial x^2} & & +(t_w)_o^c & = 0 \\
\rho S\left(\left(1+2\dfrac{e^2}{12a^2}\right)\dfrac{\partial^2 w_1^c}{\partial t^2}-\dfrac{1}{2}\dfrac{e^2}{12}\dfrac{\partial^4 w_1^c}{\partial t^2\partial x^2}\right) & & -\dfrac{\partial^2 (m_w)_1^c}{\partial x^2} & -\dfrac{\partial (n_w)_1^c}{\partial x} & +(t_w)_1^c & = 0 \\
\rho S\left(\left(1+2\dfrac{e^2}{12a^2}\right)\dfrac{\partial^2 w_1^s}{\partial t^2}-\dfrac{1}{2}\dfrac{e^2}{12}\dfrac{\partial^4 w_1^s}{\partial t^2\partial x^2}\right) & & -\dfrac{\partial^2 (m_w)_1^s}{\partial x^2} & -\dfrac{\partial (n_w)_1^s}{\partial x} & +(t_w)_1^s & = 0 \\
\rho S\dfrac{1}{2}\left(\left(\dfrac{i^2+1}{i^2}+\dfrac{\left(i^2-1\right)^2}{i^2}\dfrac{e^2}{12a^2}\right)\dfrac{\partial^2 w_i^c}{\partial t^2}-\dfrac{e^2}{12}\dfrac{\partial^4 w_i^c}{\partial t^2\partial x^2}\right) & & -\dfrac{\partial^2 (m_w)_i^c}{\partial x^2} & -\dfrac{\partial (n_w)_i^c}{\partial x} & +(t_w)_i^c & = 0 \\
\rho S\dfrac{1}{2}\left(\left(\dfrac{i^2+1}{i^2}+\dfrac{\left(i^2-1\right)^2}{i^2}\dfrac{e^2}{12a^2}\right)\dfrac{\partial^2 w_i^s}{\partial t^2}-\dfrac{e^2}{12}\dfrac{\partial^4 w_i^s}{\partial t^2\partial x^2}\right) & & -\dfrac{\partial^2 (m_w)_i^s}{\partial x^2} & -\dfrac{\partial (n_w)_i^s}{\partial x} & +(t_w)_i^s & = 0 \\
\rho S\dfrac{1}{2}\dfrac{\partial^2 u_i^c}{\partial t^2} & & & -\dfrac{\partial (n_u)_i^c}{\partial x} & +(t_u)_i^c & = 0 \\
\rho S\dfrac{1}{2}\dfrac{\partial^2 u_i^s}{\partial t^2} & & & -\dfrac{\partial (n_u)_i^s}{\partial x} & +(t_u)_i^s & = 0
\end{array}\right. \tag{B.14}
$$

For the specific case where only mode 0 is considered in the Fourier expansion, the equations of motion write:

$$
\left\{\begin{array}{llll}
\rho S\dfrac{\partial^2 U_o}{\partial t^2} & & -\dfrac{\partial N}{\partial x} & = 0 \\
\rho S\left(\dfrac{\partial^2 V_o}{\partial t^2}-\dfrac{I_y}{S}\dfrac{\partial^4 V_o}{\partial t^2\partial x^2}\right) & -\dfrac{\partial^2 M_y}{\partial x^2} & & = 0 \\
\rho S\left(\dfrac{\partial^2 w_o^c}{\partial t^2}-\dfrac{e^2}{12}\dfrac{\partial^4 w_o^c}{\partial t^2\partial x^2}\right) & -\dfrac{\partial^2 (m_w)_o^c}{\partial x^2} & +(t_w)_o^c & = 0
\end{array}\right. \tag{B.15}
$$

with the generalized forces:

$$
\left\{\begin{array}{lll}
N & = & +\dfrac{ES}{1-\nu^2}\left(\dfrac{\partial U_o}{\partial x}+\nu\dfrac{w_o^c}{a}\right) \\
M_y & = & -\dfrac{EI_y}{1-\nu^2}\dfrac{\partial^2 V_o}{\partial x^2} \\
(t_w)_o^c & = & +\dfrac{ES}{1-\nu^2}\left(\dfrac{1}{a}\left(\dfrac{w_o^c}{a}+\nu\dfrac{\partial U_o}{\partial x}\right)+\dfrac{1}{2}\left(a+w_o^c\right)\left(\dfrac{\partial^2 V_o}{\partial x^2}\right)^2+\dfrac{e^2}{12a^2}\left(\dfrac{w_o^c}{a^2}+\nu\dfrac{\partial^2 w_o^c}{\partial x^2}\right)\right) \\
(m_w)_o^c & = & -\dfrac{ES}{1-\nu^2}\dfrac{e^2}{12}\left(\dfrac{\partial^2 w_o^c}{\partial x^2}+\nu\dfrac{w_o^c}{a^2}\right)
\end{array}\right.
$$

with the moment of inertia given by:

$$
I_y = \pi a^3 e\left(1+2\frac{w_o^c}{a}+\left(\frac{w_o^c}{a}\right)^2+\frac{e^2}{12a^2}\right)
$$

When neglecting the terms associated with the non-linear coupling and the terms in $e^2/12a^2$ due to the thin-walled assumption, this leads to:

$$\left\{\begin{array}{lcl} N & = & +\dfrac{ES}{1-\nu^2}\left(\dfrac{\partial U_o}{\partial x}+\nu\dfrac{w_o^c}{a}\right) \\ M_y & = & -\dfrac{EI_y}{1-\nu^2}\dfrac{\partial^2 V_o}{\partial x^2} \\ (t_w)_o^c & = & +\dfrac{ES}{1-\nu^2}\dfrac{1}{a}\left(\dfrac{w_o^c}{a}+\nu\dfrac{\partial U_o}{\partial x}\right) \\ (m_w)_o^c & = & -\dfrac{ES}{1-\nu^2}\dfrac{e^2}{12}\dfrac{\partial^2 w_o^c}{\partial x^2} \end{array}\right. \quad \text{with} \quad I_y=\pi a^3 e = I_y^b \tag{B.16}$$

For the specific case where only mode 2 is considered in the Fourier expansion, the equations of motion write:

$$\left\{\begin{array}{llll} \rho S\dfrac{\partial^2 U_o}{\partial t^2} & & -\dfrac{\partial N}{\partial x} & = 0 \\ \rho S\left(\dfrac{\partial^2 V_o}{\partial t^2}-\dfrac{I_y}{S}\dfrac{\partial^4 V_o}{\partial t^2\partial x^2}\right) & -\dfrac{\partial^2 M_y}{\partial x^2} & & = 0 \\ \rho S\dfrac{1}{2}\left(\left(\dfrac{5}{4}+\dfrac{9}{4}\dfrac{e^2}{12a^2}\right)\dfrac{\partial^2 w_2^c}{\partial t^2}-\dfrac{e^2}{12}\dfrac{\partial^4 w_2^c}{\partial t^2\partial x^2}\right) & -\dfrac{\partial^2 (m_w)_2^c}{\partial x^2} & -\dfrac{\partial (n_w)_2^c}{\partial x}+(t_w)_2^c & = 0 \end{array}\right. \tag{B.17}$$

with the following generalized forces:

$$\left\{\begin{array}{lcl} N & = & +\dfrac{ES}{1-\nu^2}\dfrac{\partial U_o}{\partial x} \\ M_y & = & -\dfrac{EI_y}{1-\nu^2}\dfrac{\partial^2 V_o}{\partial x^2} \\ (t_w)_2^c & = & \dfrac{ES}{1-\nu^2}\left(\dfrac{3}{2}\dfrac{e^2}{12a^2}\left(3\dfrac{w_2^c}{a^2}-\nu\dfrac{\partial^2 w_2^c}{\partial x^2}\right)+\dfrac{1}{16}\left(\dfrac{\partial^2 V_o}{\partial x^2}\right)^2\left(-6a+5w_2^c+3\dfrac{e^2}{12a}\left(2+3\dfrac{w_2^c}{a}\right)\right)\right) \\ (n_w)_2^c & = & +\dfrac{ES}{1+\nu}\dfrac{1}{16}\left(1+49\dfrac{e^2}{12a^2}\right)\dfrac{\partial w_2^c}{\partial x} \\ (m_w)_2^c & = & -\dfrac{ES}{1-\nu^2}\dfrac{e^2}{24}\left(\dfrac{\partial^2 w_2^c}{\partial x^2}-3\nu\dfrac{w_2^c}{a^2}\right) \end{array}\right.$$

with the moment of inertia given by:

$$I_y=\pi a^3 e\left(1-\frac{3}{2}\frac{w_2^c}{a}+\frac{5}{8}\left(\frac{w_2^c}{a}\right)^2+\frac{e^2}{12a^2}\right)$$

Assuming that $\partial^2_{x^2} w_2^c = 0$ and neglecting the terms in $e^2/12a^2$ in $(n_w)_2^c$, $(m_w)_2^c$, in the coupling term in $(t_w)_2^c$ and in I_y leads to:

$$\left\{\begin{array}{lcl} N & = & +\dfrac{ES}{1-\nu^2}\dfrac{\partial U_o}{\partial x} \\ M_y & = & -\dfrac{EI_y}{1-\nu^2}\dfrac{\partial^2 V_o}{\partial x^2} \\ (t_w)_2^c & = & \dfrac{ES}{1-\nu^2}\left(\dfrac{9}{2}\dfrac{e^2}{12a^2}\dfrac{w_2^c}{a^2}+\dfrac{1}{16}\left(\dfrac{\partial^2 V_o}{\partial x^2}\right)^2\left(-6a+5w_2^c\right)\right) \\ (n_w)_2^c & = & \dfrac{ES}{1+\nu}\dfrac{1}{16}\dfrac{\partial w_2^c}{\partial x} \\ (m_w)_2^c & = & 0 \end{array}\right. \tag{B.18}$$

with $I_y=\pi a^3 e\left(1-\dfrac{3}{2}\dfrac{w_2^c}{a}+\dfrac{5}{8}\left(\dfrac{w_2^c}{a}\right)^2\right)$.

Appendix B.4. Cylindrical shell equations of motion

It has also to be noticed that the present tube kinematics incorporates the circular cylindrical shell kinematics. Considering the shell terms in Eqs. (B.2) and (B.7) leads to the two following relationships:

$$\mathcal{P}_a = \int_\Omega \rho \left[\frac{\partial^2 u_o}{\partial t^2}\delta u_o + z^2 \frac{\partial^2 u_1}{\partial t^2}\delta u_1 + \frac{\partial^2 v_o}{\partial t^2}\delta v_o + z^2 \frac{\partial^2 v_1}{\partial t^2}\delta v_1 + \frac{\partial^2 w_o}{\partial t^2}\delta w_o \right] \mathrm{d}V$$

and

$$\begin{aligned}\mathcal{P}_i = -\int_\Omega \Bigg[& \sigma^m_{xx}\frac{\partial \delta u_o}{\partial x} + \sigma^m_{x\theta}\frac{1}{a}\frac{\partial \delta u_o}{\partial \theta} - z^2\sigma^k_{xx}\frac{\partial \delta u_1}{\partial x} - \sigma^k_{x\theta}\frac{z^2}{a}\frac{\partial \delta u_1}{\partial \theta} + \sigma^m_{x\theta}\frac{\partial \delta v_o}{\partial x} + \left(\sigma^m_{\theta\theta} - \sigma^k_{\theta\theta}\frac{z^2}{a}\right)\frac{1}{a}\frac{\partial \delta v_o}{\partial \theta} \\ & + \sigma^k_{x\theta} z^2 \frac{\partial \delta v_1}{\partial x} + + \sigma^k_{\theta\theta}\frac{z^2}{a}\frac{\partial \delta v_1}{\partial \theta} + \left(\sigma^m_{\theta\theta} - \sigma^k_{\theta\theta}\frac{z^2}{a}\right)\frac{1}{a}\delta w_o \Bigg] \mathrm{d}V\end{aligned}$$

As a consequence, the corresponding equations of motion write:

$$\left\{ \begin{array}{lcl} \rho a e \dfrac{\partial^2 u_o}{\partial t^2} & = & a\dfrac{\partial N_x}{\partial x} + \dfrac{\partial Q_{x\theta}}{\partial \theta} \\ \rho a e \dfrac{e^2}{12}\dfrac{\partial^2 u_1}{\partial t^2} & = & -a\dfrac{\partial M_x}{\partial x} - \dfrac{\partial N_{x\theta}}{\partial \theta} \\ \rho a e \dfrac{\partial^2 v_o}{\partial t^2} & = & a\dfrac{\partial Q_{x\theta}}{\partial x} + \dfrac{\partial Q_\theta}{\partial \theta} \\ \rho a e \dfrac{e^2}{12}\dfrac{\partial^2 v_1}{\partial t^2} & = & a\dfrac{\partial N_{x\theta}}{\partial x} + \dfrac{\partial N_\theta}{\partial \theta} \\ \rho a e \dfrac{\partial^2 w_o}{\partial t^2} & = & -Q_\theta \end{array} \right. \quad \text{with} \quad \left\{ \begin{array}{lcl} N_x & = & \displaystyle\int \sigma^m_{xx}\,\mathrm{d}z \\ Q_{x\theta} & = & \displaystyle\int \sigma^m_{x\theta}\,\mathrm{d}z \\ M_x & = & \displaystyle\int \sigma^k_{xx} z^2\,\mathrm{d}z \\ N_{x\theta} & = & \displaystyle\int \sigma^k_{x\theta} z^2\,\mathrm{d}z \\ Q_\theta & = & \displaystyle\int \left(\sigma^m_{\theta\theta} - \sigma^k_{\theta\theta}\frac{z^2}{a}\right)\mathrm{d}z \\ N_\theta & = & \displaystyle\int \sigma^k_{\theta\theta} z^2\,\mathrm{d}z \end{array} \right. \tag{B.19}$$

where the variables Q, N and M correspond to the transverse shearing force, in-plane force and moments, respectively. These equations are in agreement with those expressed in [47, 48] for circular cylindrical shells when considering integration over the elementary volume $a\ \mathrm{d}\theta\mathrm{d}z\mathrm{d}x$ instead of $(a+z)\ \mathrm{d}\theta\mathrm{d}z\mathrm{d}x$.

Appendix C. Size and sparseness of the stiffness matrices

Using the same notations that the ones used in Sec. 3, the (symmetric) stiffness matrix of the tube element can be written as:

$$\mathbf{K}_e = \begin{pmatrix} \mathbf{K}_e^{11} & \mathbf{K}_e^{12} \\ \mathbf{K}_e^{21} & \mathbf{K}_e^{22} \end{pmatrix} \quad \text{with} \quad \mathbf{K}_e^{ij} = \int_0^{\ell_e} \left(\mathbf{B}_e^i\right)^T \mathbf{D}\ \mathbf{B}_e^j \mathrm{d}x \tag{C.1}$$

with $\mathbf{D}$ the (symmetric) constitutive matrix. With the expressions of the generalized forces and moments expressed in Eqs. (B.9), (B.10), (B.11), (B.12) and (B.13), we can conclude that the non-zero components of the matrix $\mathbf{K}_e^{ij}$ are:

$$\mathbf{K}_e^{ij} = \begin{pmatrix} \mathbf{K}_{ij}^{b} & \mathbf{K}_{ij}^{b,s_o} & \mathbf{K}_{ij}^{b,s_1} & \mathbf{K}_{ij}^{b,s_2} & \mathbf{K}_{ij}^{b,s_3} & \mathbf{K}_{ij}^{b,s_4} & \mathbf{K}_{ij}^{b,s_5} & \mathbf{K}_{ij}^{b,s_6} \\ \mathbf{K}_{ij}^{s_o,b} & \mathbf{K}_{ij}^{s_o} & \mathbf{K}_{ij}^{s_o,s_1} & \mathbf{K}_{ij}^{s_o,s_2} & \mathbf{0} & \mathbf{0} & \mathbf{0} & \mathbf{0} \\ \mathbf{K}_{ij}^{s_1,b} & \mathbf{K}_{ij}^{s_1,s_o} & \mathbf{K}_{ij}^{s_1} & \mathbf{K}_{ij}^{s_1,s_2} & \mathbf{K}_{ij}^{s_1,s_3} & \mathbf{0} & \mathbf{0} & \mathbf{0} \\ \mathbf{K}_{ij}^{s_2,b} & \mathbf{K}_{ij}^{s_2,s_o} & \mathbf{K}_{ij}^{s_2,s_1} & \mathbf{K}_{ij}^{s_2} & \mathbf{K}_{ij}^{s_2,s_3} & \mathbf{K}_{ij}^{s_2,s_4} & \mathbf{0} & \mathbf{0} \\ \mathbf{K}_{ij}^{s_3,b} & \mathbf{0} & \mathbf{K}_{ij}^{s_3,s_1} & \mathbf{K}_{ij}^{s_3,s_2} & \mathbf{K}_{ij}^{s_3} & \mathbf{K}_{ij}^{s_3,s_4} & \mathbf{K}_{ij}^{s_3,s_5} & \mathbf{0} \\ \mathbf{K}_{ij}^{s_4,b} & \mathbf{0} & \mathbf{0} & \mathbf{K}_{ij}^{s_4,s_2} & \mathbf{K}_{ij}^{s_4,s_3} & \mathbf{K}_{ij}^{s_4} & \mathbf{K}_{ij}^{s_4,s_5} & \mathbf{K}_{ij}^{s_4,s_6} \\ \mathbf{K}_{ij}^{s_5,b} & \mathbf{0} & \mathbf{0} & \mathbf{0} & \mathbf{K}_{ij}^{s_5,s_3} & \mathbf{K}_{ij}^{s_5,s_4} & \mathbf{K}_{ij}^{s_5} & \mathbf{K}_{ij}^{s_5,s_6} \\ \mathbf{K}_{ij}^{s_6,b} & \mathbf{0} & \mathbf{0} & \mathbf{0} & \mathbf{0} & \mathbf{K}_{ij}^{s_6,s_4} & \mathbf{K}_{ij}^{s_6,s_5} & \mathbf{K}_{ij}^{s_6} \end{pmatrix}$$

where the matrix $\mathbf{K}_e^{ij}$ has a symmetric/anti-symmetric form with for $k \geq 2$:

$$\mathbf{K}_{ij}^{b} = \begin{pmatrix} \times & 0 & 0 \\ 0 & \times & \times \\ 0 & \times & \times \end{pmatrix}, \quad \mathbf{K}_{ij}^{b,s_o} = \begin{pmatrix} \times & \times \\ \times & \times \\ \times & \times \end{pmatrix}, \quad \mathbf{K}_{ij}^{b,s_1} = \begin{pmatrix} 0 & 0 & 0 & 0 \\ \times & \times & \times & \times \\ \times & \times & \times & \times \end{pmatrix}, \quad \mathbf{K}_{ij}^{b,s_k} = \begin{pmatrix} 0 & 0 & 0 & 0 & 0 & 0 \\ \times & \times & \times & \times & \times & \times \\ \times & \times & \times & \times & \times & \times \end{pmatrix},$$

$$\mathbf{K}_{ij}^{s_o} = \begin{pmatrix} \times & \times \\ \times & \times \end{pmatrix}, \quad \mathbf{K}_{ij}^{s_o,s_1} = \begin{pmatrix} 0 & 0 & \times & \times \\ 0 & 0 & \times & \times \end{pmatrix}, \quad \mathbf{K}_{ij}^{s_o,s_2} = \begin{pmatrix} 0 & \times & \times & 0 & 0 & 0 \\ 0 & \times & \times & 0 & 0 & 0 \end{pmatrix},$$

$$\mathbf{K}_{ij}^{s_1} = \begin{pmatrix} \times & \times & 0 & 0 \\ \times & \times & 0 & 0 \\ 0 & 0 & \times & \times \\ 0 & 0 & \times & \times \end{pmatrix}, \quad \mathbf{K}_{ij}^{s_1,s_2} = \begin{pmatrix} 0 & 0 & 0 & \times & \times & \times \\ 0 & 0 & 0 & \times & \times & \times \\ \times & \times & \times & 0 & 0 & 0 \\ \times & \times & \times & 0 & 0 & 0 \end{pmatrix}, \quad \mathbf{K}_{ij}^{s_1,s_3} = \begin{pmatrix} 0 & \times & \times & 0 & 0 & 0 \\ 0 & \times & \times & 0 & 0 & 0 \\ 0 & 0 & 0 & 0 & \times & \times \\ 0 & 0 & 0 & 0 & \times & \times \end{pmatrix},$$

and for $k \geq 2$

$$\mathbf{K}_{ij}^{s_k} = \begin{pmatrix} \times & \times & \times & 0 & 0 & 0 \\ \times & \times & \times & 0 & 0 & 0 \\ \times & \times & \times & 0 & 0 & 0 \\ 0 & 0 & 0 & \times & \times & \times \\ 0 & 0 & 0 & \times & \times & \times \\ 0 & 0 & 0 & \times & \times & \times \end{pmatrix}, \quad \mathbf{K}_{ij}^{s_k,s_{k+1}} = \begin{pmatrix} 0 & 0 & 0 & 0 & \times & \times \\ 0 & 0 & 0 & \times & \times & \times \\ 0 & 0 & 0 & \times & \times & \times \\ 0 & \times & \times & 0 & 0 & 0 \\ \times & \times & \times & 0 & 0 & 0 \\ \times & \times & \times & 0 & 0 & 0 \end{pmatrix}, \quad \mathbf{K}_{ij}^{s_k,s_{k+2}} = \begin{pmatrix} 0 & 0 & 0 & 0 & 0 & 0 \\ 0 & \times & \times & 0 & 0 & 0 \\ 0 & \times & \times & 0 & 0 & 0 \\ 0 & 0 & 0 & 0 & 0 & 0 \\ 0 & 0 & 0 & 0 & \times & \times \\ 0 & 0 & 0 & 0 & \times & \times \end{pmatrix},$$

where the non-zero components due to the non-linear coupling are colored in magenta and where the superscript b and s_k correspond to the beam and the shell DOFs associated with the Fourier mode k, respectively. As a consequence, the number of the non-zero components of the stiffness matrix of the tube element is 1948 for the non-linear formulation and 476 for the linear formulation. In comparison, the stiffness of a rectangular plate with 4 nodes and 6 DOFs per node can be written as:

$$\mathbf{k}_e^s = \begin{pmatrix} \mathbf{k}_e^{ij} \end{pmatrix} \quad \text{where} \quad \mathbf{k}_e^{ij} = \begin{pmatrix} \mathbf{k}_{ij}^{tr} & \mathbf{0} \\ \mathbf{0} & \mathbf{k}_{ij}^{rot} \end{pmatrix} \quad \text{for } 1 \leq i, j \leq 4$$

where the superscript tr and rot correspond to the translational and rotational DOFs, respectively, with:

$$\mathbf{k}_{ij}^{tr} = \begin{pmatrix} \times & \times & 0 \\ \times & \times & 0 \\ 0 & 0 & 0 \end{pmatrix} \quad \text{and} \quad \mathbf{k}_{ij}^{rot} = \begin{pmatrix} \times & \times & \times \\ \times & \times & \times \\ \times & \times & \times \end{pmatrix}$$

As a consequence, the number of the non-zero components of the shell stiffness matrix is 208.